Exploring Potential: ALPS II's TES Detection System for Direct Dark Matter Searches

Dissertation

zur Erlangung des Doktorgrades

an der Fakultät für Mathematik, Informatik und Naturwissenschaften

Fachbereich Physik

der Universität Hamburg

vorgelegt von

Christina Schwemmbauer

Hamburg

2025

Eidesstattliche Versicherung:
Hiermit versichere ich an Eides statt, die vorliegende Dissertationsschrift selbst verfasst und keine anderen als die angegebenen Hilfsmittel und Quellen benutzt zu haben. Sofern im Zuge der Erstellung der vorliegenden Dissertationsschrift generative Künstliche Intelligenz (gKI) basierte elektronische Hilfsmittel verwendet wurden, versichere ich, dass meine eigene Leistung im Vordergrund stand und dass eine vollständige Dokumentation aller verwendeten Hilfsmittel gemäß der Guten wissenschaftlichen Praxis vorliegt. Ich trage die Verantwortung für eventuell durch die gKI generierte fehlerhafte oder verzerrte Inhalte, fehlerhafte Referenzen, Verstöße gegen das Datenschutz- und Urheberrecht oder Plagiate.

Affidavit:
I hereby declare and affirm that this doctoral dissertation is my own work and that I have not used any aids and sources other than those indicated. If electronic resources based on generative artificial intelligence (gAI) were used in the course of writing this dissertation, I confirm that my own work was the main and value-adding contribution and that complete documentation of all resources used is available in accordance with good scientific practice. I am responsible for any erroneous or distorted content, incorrect references, violations of data protection and copyright law or plagiarism that may have been generated by the gAI.

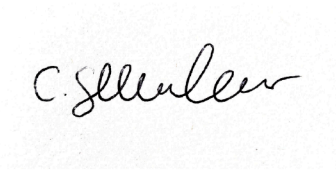

Hamburg, den 31.07.2025 Christina Schwemmbauer

Gutachter der Dissertation:	Prof. Dr. Erika Garutti Dr. Axel Lindner
Zusammensetzung der Prüfungskommission:	Prof. Dr. Erika Garutti Dr. Axel Lindner Dr. Andreas Ringwald Prof. Dr. Oliver Gerberding Prof. Dr. Daniela Pfannkuche
Vorsitzender der Prüfungskommission:	Prof. Dr. Daniela Pfannkuche
Datum der Disputation:	29.09.2025
Vorsitzender des Fach-Promotionsausschusses Physik:	Prof. Dr. Wolfgang J. Parak
Leiter des Fachbereichs Physik:	Prof. Dr. Markus Drescher
Dekan der Fakultät MIN:	Prof. Dr.-Ing. Norbert Ritter

Abstract

This thesis both proposes and experimentally explores the opportunity to operate Transition Edge Sensors (TES) as detectors for Dark Matter (DM)-scattering by simultaneously employing them as target and sensor. By exploiting their microcalorimetric capabilities and sensitivity to low energy depositions, competitive limits can be set on low mass DM interactions based on electron scattering. Further limits on absorption and DM-nucleon scattering can be determined as well.

With a sensitive area of 25 µm × 25 µm, 20 nm thickness, and a mass of just 0.2 ng, the TES sensors are not comparable to large scale experiments searching for ∼GeV-scale Weakly Interacting Massive Particles (WIMPs). However, the sensors' sensitivity to energy depositions as low as ∼ 0.3 eV enables sensitivity to much lower sub-MeV DM masses. TES are operated on the transition curve between the normal and superconducting state, where the sensor is sensitive to the smallest energy depositions, yielding detectable pulses. Based on the detector's sensitivity, especially to single near-infrared photons, it should also be sensitive to sub-MeV to high MeV DM particles scattering in its electron or nucleon systems. By exploiting the similarity of these processes and using the ALPS II experiment's TES detection system, dedicated DM searches were performed with two distinct TES detection modules.

In dedicated experimental setups, the well-known ALPS II-optimized analysis scheme was employed to determine ideal detector configurations for DM searches in need of a sufficiently large energy bandwidth. In a next step, the detector's energy response was investigated by analyzing the pulse shapes of photons from different lasers with photon energies from 0.76 eV to 1.41 eV. During these tests, a linear proportionality between the pulse's integral with the energy was found, while at the same time, the rise and decay time of the pulses stayed predominantly constant over these energies. This performance along with subsequent simulations of signal pulses over a larger energy range can be used for a dedicated event selection to isolate photon-like pulses from the various backgrounds present in the system. Therefore, these background sources, including fast (baseline) noise spikes, are mitigated by dedicated analysis and straightforward cutting schemes.

Dedicated DM search measurements are performed using two different detector modules. The measurement and analysis pipeline was optimized for module TES D. A second module TES F with a setup adjusted for DM search measurements is presented in a preliminary analysis, as well. DM search measurements of 489 h and 400 h have been performed, respectively. By applying dedicated event selections to each, limits on different DM parameter spaces have been set for both, considering expected DM interaction rates in

the explored DM mass range. The resulting limits are compared to results originating from similar experimental efforts, especially one employing Superconducting Nanowire Single Photon Detectors (SNSPDs) as both target and sensor, as well. The TES modules are able to surpass limits set by the first generation of these SNSPDs for lower masses in the light mediator limit. However, limits set by a dedicated optimized second generation SNSPD experiment exceed both. Nevertheless, this enhancement from a first to a second upgraded generation already exemplifies the strength of such an approach, as similar improvements can be explored for TES detectors as well. Therefore, projections for possible future detection scenarios are explored, presenting the strength of possible second generation TES detection systems. Hence, it was shown for the first time, that TES detectors can be used as a simultaneous sensor and target in direct DM experiments with a plethora of possibilities for further upgrades and optimization.

Zusammenfassung

In dieser Arbeit wird die Möglichkeit untersucht, Übergangskantensensoren (TES) als Detektoren zur Messung der Streuung von Dunkler Materie (DM) einzusetzen. Dazu werden die Detektoren gleichzeitig als Target und Sensor verwendet. Durch die Nutzung ihrer mikrokalorimetrischen Fähigkeiten und ihrer Empfindlichkeit gegenüber niedrigen Energiedepositionen können konkurrenzfähige Grenzen für Wechselwirkungen von DM mit niedriger Masse auf der Grundlage von Streuung an Elektronen festgelegt werden. Weitere Grenzen für die Absorption und die Streuung von DM an Nukleonen können ebenfalls bestimmt werden.

Mit einer sensitiven Fläche von $25\,\mu m \times 25\,\mu m$, einer Dicke von 20 nm und einer Masse von nur 0.2 ng sind die TES-Sensoren nicht mit groß angelegten Experimenten zur Suche nach schwach wechselwirkenden massiven Teilchen (WIMPs) auf der ∼GeV-Skala vergleichbar. Ihre niedrige Energieschwelle von bis zu $\sim 0.3\,eV$ ermöglicht jedoch eine Empfindlichkeit für viel niedrigere DM-Massen im Sub-MeV Bereich. TES werden an der Übergangskurve zwischen dem normalen und dem supraleitenden Zustand betrieben, wo der Sensor empfindlich auf kleinste Energiedepositionen reagiert und detektierbare Impulse erzeugt. Aufgrund der Empfindlichkeit des Detektors, insbesondere gegenüber einzelnen Photonen im nahen Infrarotbereich, sollte er auch empfindlich gegenüber DM-Teilchen im Sub-MeV bis hohen MeV-Bereich sein, die mit seinen Elektronen- oder Nukleonsystemen streuen. Unter Ausnutzung der Ähnlichkeit dieser Prozesse und unter Verwendung des TES-Detektionssystems des ALPS II Experiments wurden spezielle DM-Suchen mit zwei unterschiedlichen TES-Detektionsmodulen durchgeführt.

In speziellen Versuchsaufbauten wurde das bekannte, für ALPS II optimierte Analyseschema verwendet, um ideale Detektorkonfigurationen für die Suche nach Dunkler Materie zu ermitteln, für die eine ausreichend große energetische Bandbreite erforderlich ist. In einem nächsten Schritt wurde die Energieantwort des Detektors untersucht, indem die Signalformen von Photonen aus verschiedenen Lasern mit Energien von 0.76 eV to 1.41 eV analysiert wurden. Bei diesen Tests wurde eine lineare Proportionalität zwischen dem Pulsintegral und der Energie festgestellt, während gleichzeitig die Anstiegs- und Abklingzeit der Signale über diese Energien hinweg überwiegend konstant blieb. Dieses Verhalten kann zusammen mit nachfolgenden Simulationen von Signalpulsen über einen größeren Energiebereich für eine spezielle Asuwahl an Energien verwendet werden, um photonähnliche Signale von den verschiedenen im System vorhandenen Untergründen zu isolieren. Daher werden diese Untergrundquellen, einschließlich schneller Ausschlägen im elektronischen Rauschen, durch spezielle Analysen und simple Schnittschemata reduziert.
Spezielle Dunkle Materie Suchmessungen werden mit zwei verschiedenen Detektormodulen durchgeführt. Die Mess- und Analysepipeline wurde für das Modul TES D optimiert. Ein zweites Modul, TES F, dessen Aufbau für Messungen zur Suche nach Dunkler Materie angepasst wurde, wird ebenfalls in einer vorläufigen Analyse vorgestellt. Es wurden Messungen zur Suche nach Dunkler Materie von 489 h bzw. 400 h durchgeführt. Durch die Anwendung spezieller Signalselektionen auf jedes Modul wurden für beide Module Limits für verschiedene DM-Parameterräume bestimmt, wobei die erwarteten DM-Wechselwirkungsraten im untersuchten DM-Massenbereich berücksichtigt wurden. Die resultierenden Limits werden mit Ergebnissen aus ähnlichen experimentellen Arbeiten verglichen, insbesondere mit denen, bei denen ebenfalls supraleitende Nanodraht-Einzelphotonen-Detektoren (SNSPDs) sowohl als Target als auch als Sensor verwendet wurden. Die TES-Module sind in der Lage, die von der ersten Generation dieser SNSPDs festgelegten Limits für niedrigere Massen im Limit leichter Mediatorteilchen zu überschreiten. Die von einem speziellen, optimierten SNSPD-Experiment der zweiten Generation festgelegten Limits übertreffen jedoch beide. Dennoch verdeutlicht diese Verbesserung von der ersten zur zweiten Generation bereits die Stärke eines solchen Ansatzes, da ähnliche Verbesserungen auch für TES-Detektoren erwartet werden können. Daher werden Prognosen für mögliche zukünftige Detektionsszenarien untersucht, um die Stärke möglicher TES-Detektionssysteme der zweiten Generation aufzuzeigen. Damit wurde erstmals gezeigt, dass TES Sensoren in direkten DM-Experimenten mit einer Vielzahl von Möglichkeiten gleichzeitig als Sensor und Target verwendet werden können.

Contents

1 Introduction

> *The probability of success is difficult to estimate; but if we never search, the chance of success is zero"*
>
> — **G. Cocconi & P. Morrison**

It is part of the inherent nature and history of the physical sciences, that the stories of many new discoveries begin when something is missing. One of the earliest examples is the discovery of a planet. When calculations of Uranus' orbit based on Newtonian forces did not match telescope observations, two mathematicians, Urbain Le Verrier and John Couch Adams were able to correctly predict the exact position of a missing gravitational mass, independently from each other, leading to the discovery of Neptune in 1846 [1]. In 1859, it was again calculations based on Newton's laws that showed a mismatch between the calculated and observed orbit of Mercury. Le Verrier again hypothesized unknown gravitational bodies as the source of the orbit's deviations, to be exact: a planet Vulcan. Decades later it was calculations by Einstein dispelling the claims of a necessary planet, and instead explaining the perihelion motion of Mercury via his new theory of general relativity [2]. Similar stories are found throughout history and science, playing major roles e.g. also in the discovery of the neutron. While these examples have led to major discoveries, today's largest and longest standing missing mass problem remains unsolved.

The missing mass in spiral galaxies, first observed by Vera Rubin in 1970 [3], posing a mismatch between observed and expected rotational velocities, gave rise to a widely accepted theory of a missing gravitational source in our galaxy called Dark Matter (DM). This term was first introduced for the missing mass when aiming to explain the dynamics of the Coma Cluster with the Virial theorem by Fritz Zwicky in 1933 [4]. After decades of dedicated experiments and numerous new theories, the nature of DM remains elusive, even though many more hints such as the Bullet Cluster [5] and gravitational lensing effects [6] have been discovered.

However, these combined efforts have not only fostered advancements in technology, but have also been able to rule-out certain models and configurations. Hence, the next years could be crucial in determining what kind of story the search for DM represents. Every new experimental and theoretical effort therefore helps to narrow down the remaining possibilities or to uncover new exploring potential.

This thesis explores the potential of using superconducting Transition Edge Sensor (TES) detectors for direct particle DM searches, mainly via scattering. By performing dedicated background measurements with the TES detection system designed for the Any Light Particle Search II (ALPS II) experiment, the viability of this technology to function as both target and sensor in DM scattering experiments is explored. Subsequently, this thesis is structured as follows:

- The remainder of this chapter shortly introduces existing particle DM models and dedicated search efforts (many of which already include TES technology), including the ALPS II experiment, whose TES system is employed for this study. The viability of superconductors for dedicated DM searches and specifically TES is discussed, before the working principle and theory of TES is introduced, as well as their readout and amplification via Superconducting Quantum Interference Device (SQUID) chips. Last but not least, the calculation of DM-electron scattering rates in a TES is considered.
- Chapter 2 describes the general experimental setup including the cryogenic cooling, the used TES detection modules as well as the readout electronics. Afterwards, the different experimental setups used within this thesis are described.
- Chapter 3 regards the optimization and calibration of the used detection modules. After describing the general signal shape and fitting scheme used for TES signals, the optimization for DM searches and energy calibration is discussed. Finally, possible backgrounds present in the setup are considered, including the results of dedicated noise simulations.
- Chapter 4 discusses the first dedicated DM-electron scattering searches performed with a TES detection system, including subsequent analysis. Furthermore, the sensitivity of the detectors to DM signals is evaluated and exclusion limits for the mass-dependent DM-electron scattering cross-section are derived and discussed.
- Chapter 5 then adds to the previous chapter by considering two additional DM search channels accessible with TES detectors, namely dark photon DM absorption and DM-nucleon scattering. Constraints on the respective parameter spaces, compared with relevant limits, are determined and discussed.
- Chapter 6 concludes and summarizes the findings and introduces an outlook on possible future enhancements of the investigated setup and beyond.

1.1 Particle Dark Matter and Searches

There is a plethora of particle DM models ranging from wave-like DM with masses as low as 10^{-21} eV to a heavy Weakly Interacting Massive Particle (WIMP) with masses up to

∼TeV and even non-particle DM-candidates such as primordial black holes. Even though many different experiments have explored these different models, no verifiable detection of a new DM particle has been achieved so far. A summary of many of the most prominent models, as well as current efforts towards their detection can be found in Ref. [7, 8]. This section shortly describes the DM models and searches that have been the focus of most experimental efforts in recent decades, as well as emerging new ideas that are gaining more traction due to the ongoing lack of discovery.

Two of the currently most favored models for particle DM include one ultra-light candidate, the axion, and another very heavy candidate, the WIMP. The axion, was originally proposed by Wilczek and Weinberg [9, 10] to solve the strong CP-problem. The particle arises from the spontaneous breaking of the Peccei-Quinn symmetry, first introduced by Peccei and Quinn [11]. Consequently, the axion represents a ready solution possibly able to solve at least two problems at once. Measurement schemes to detect an axion are often based on the axion coupling to two Standard Model (SM) photons, which is exploited via axion-photon conversion in a background magnetic field. Three different schemes are mainly employed: The haloscope detecting axions from the DM halo in our galaxy (e.g. MADMAX [12], ADMX [13]), the helioscope detecting axions produced in the Sun (e.g. CAST [14], BABYIAXO [15]) and the Light-Shining-through-Wall (LSW) approach for producing axions in the lab. The ALPS II experiment employs the latter scheme, which is shortly discussed in Sec. 1.3.1. More details are found in Ref. [16], and especially in the context of ALPS II searches in Ref. [17, 18].

In recent decades, ever grander experiments excluded ever larger portions of the DM-nucleon scattering parameter space in search of a WIMP signal. Even though many of the dedicated WIMP experiments vary in size, scale, materials and methods, most of them aim to detect the new particles via an elastic scattering approach. A DM halo is expected to be present in our galaxy, which would enable terrestrial detection of DM particles traveling through the earth. In theory, massive ∼GeV scale WIMPs could be detected by measuring the recoil energy of an elastic scattering event with such a particle with the *target* nuclei. Subsequent signals, depending on the specific target and experiments, are then detected and read out by a separate *sensor*. A majority of these consists either of large scale ton per year searches with a Time Projection Chamber (TPC) filled with cryogenically cooled liquid noble gases as targets or solid-state targets such as semiconductors. For the TPCs, the sensing is usually done via Photo-Multiplier Tubes (PMT). Examples of these experiments include the XENONnT experiment [19], the PandaX experiment [20] and the LZ experiment [21]. On the other hand, many experiments employ a semiconductor as target, which is coupled to a separate sensor, such as a TES[1]. A recent landscape of WIMP searches and their already excluded parameter space is shown in Fig. 1.1.

[1]More details including examples for semiconductor-based WIMP searches are given in Sec. 1.2

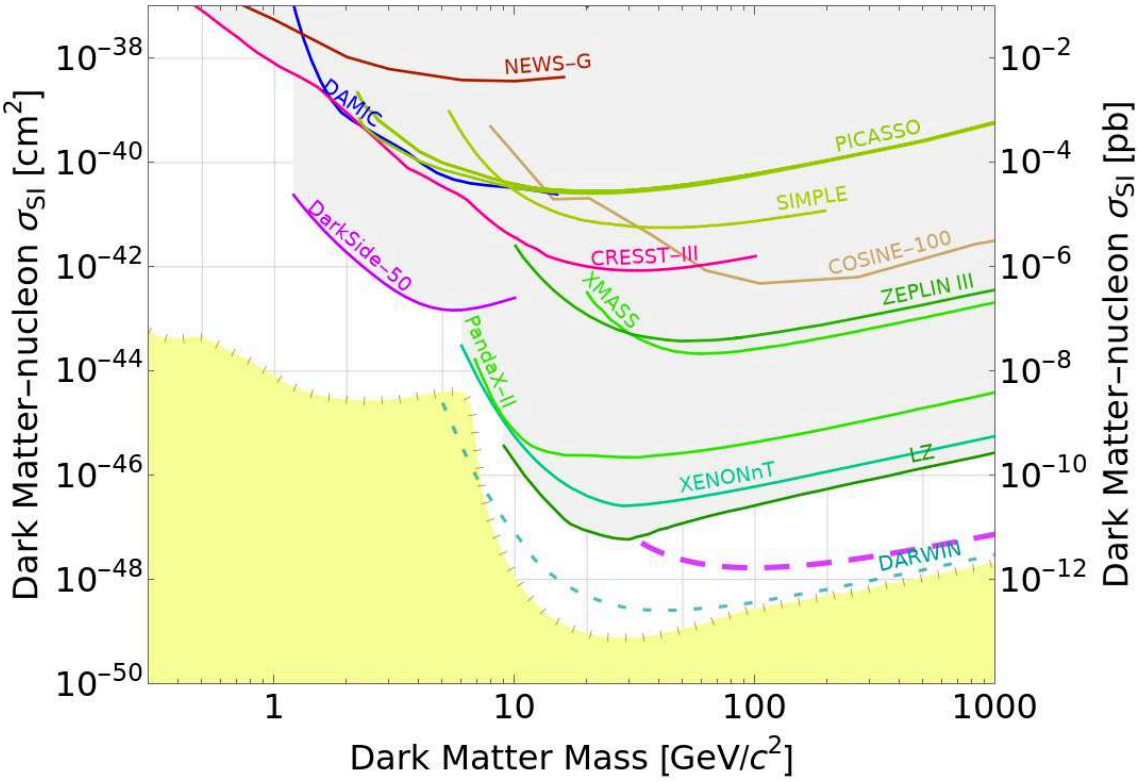

Fig. 1.1.: Parameter space of spin-independent DM-nucleon cross sections σ_{SI} as a function of DM mass on the GeV-scale. All nuclear recoil limits are scaled to a local dark matter density of $0.3\,\mathrm{GeV/c^2}$. The solid lines and gray-shaded areas indicate exclusion limits based on direct detection, while the dashed lines represent sensitivity projections for future experimental upgrades. The yellow shaded area shows the expected neutrino background [22], in this case shown for a Xenon target. The plot reflects the status of the data as of April 7, 2023 and relies on data based on Ref. [20, 21, 23–37]. Figure created with [38].

This parameter space refers to the spin-independent DM-nucleon cross sections σ_{SI} on the y-axis and the corresponding DM mass in the ∼GeV mass range on the x-axis. The solid lines and gray-shaded areas show the exclusion limits set by dedicated nucleon-scattering experiments on this parameter space. Therefore, no consistent hint for DM particles in this mass range has been found with the listed experiments. The yellow shaded region represents the neutrino background that will dominate the interactions measured with these experiments, once future optimizations increase their sensitivity in this parameter space to cross into this space. Originally titled, neutrino floor, it has recently been referred to as neutrino fog more often, as a result of the dedicated work towards mitigating the influence of solar neutrino background at lower scattering cross-sections [39]. The goal is to investigate unexplored parameter space, i.e. investigating lower cross-sections or different mass ranges. In order to gain sensitivity for lower cross-sections, larger target volumes are needed. Hence, the active target mass of some nucleon-scattering experiments is already reaching an order of tons. These experiments are expected to reach and be limited by

the neutrino fog in the coming years. In order to investigate lower mass ranges in this plot, the experiment needs to be sensitive to energy depositions from DM particles of a certain mass. Below GeV-masses, this proves increasingly complicated with DM scattering off of heavy nuclei. For lower DM masses, the reduced recoil energies are increasingly complicated to measure (see Sec. 1.2). When evaluating the entirety of this parameter space and considering that no conclusive signals have been found, it could hint towards DM particles being found somewhere else.

When looking for DM candidates lighter than WIMPs, but still accessible by scattering experiments, recent years have brought forth many new theories, which can be categorized as *light dark matter* residing in a hidden sector, ranging from keV to GeV masses, usually characterized by weak couplings to the SM. Some of these theories include WIMPless [40], asymmetric [41], secluded WIMP[42] or thermal relic DM [43]. Focus is therefore slowly shifting to sub-GeV and even sub-MeV DM masses, for which new detection methods are needed. Some of these methods include scattering off lighter nuclei instead of heavy ones, as planned for the DELight experiment employing a superfluid helium target [44], while others focus around an entirely different target category: Instead of nuclei, DM scattering off of electrons could be measured as well [45], which could be facilitated by using superconductors as targets, instead. In this work, the focus lies mainly on probing TES viability in this mass region, not on a specific DM model.

1.2 Superconductors as Dark Matter Detectors

Superconducting detectors, TES in particular, have been a key sensing technology in the search for DM for over a decade. Oftentimes used for dedicated WIMP experiments, these detectors are usually employed as sensors attached to a larger target mass. The following section focuses on the use of superconductors as targets in DM searches, instead, where they facilitate access to DM-electron scattering.

To explore sub-GeV DM mass parameter space through electron scattering experiments, suitable DM models and experimental setups need to be considered. Details on possible DM models and constraints are discussed thoroughly in Ref. [46]. For the case, where DM resides in a hidden sector, it would have to interact with the SM via a mediator ϕ with couplings to both the DM particles and the electromagnetic charge. These mediators can either be massive or light mediators, when comparing the mediator mass m_ϕ to the energy deposited in a detector E_D by a scattering event. In the following, 2-to-2 elastic scattering via such a mediator is assumed, where applicable, for both the light and heavy mediator case.

In simple terms, a relation can be used to gauge the transferred energies in scattering events, no matter if the scattering process is based on electrons or nuclei. This rule of thumb is

also discussed in Ref. [47]. For this, the non-relativistic case is considered, where the DM halo model is assumed. DM particles residing in this halo will therefore move through the earth and hit a target with a velocity of $\sim 10^{-3}c$. Thereby, for this non-relativistic case, the maximum amount of energy deposited in an elastic-scattering event $E_{D_{\max}}$ is always the entire kinetic energy of the incoming particle, in this case, a DM particle. With the DM mass m_{DM} and velocity v_{DM}, this yields

$$E_{D_{\max}} = E_{\mathrm{kin}}^{\mathrm{tot}} \sim m_{\mathrm{DM}} v_{\mathrm{DM}}^2 \sim 10^{-6} m_{\mathrm{DM}} \tag{1.1}$$

in natural units. Hence, from the mass of the incoming DM particle, the maximum deposited energy can be derived. This relation is visualized in Fig. 1.2.

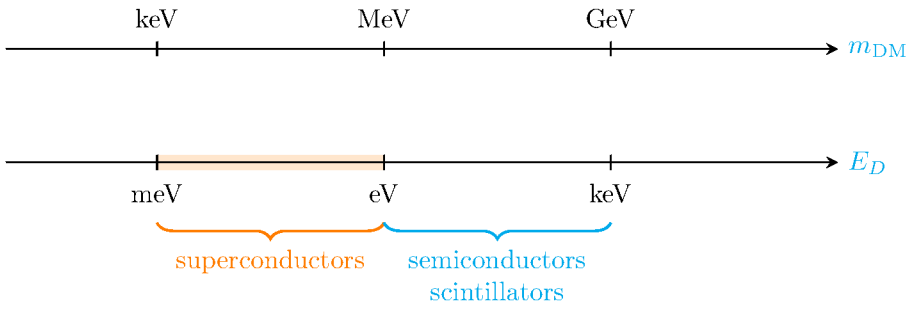

Fig. 1.2.: Visualization of the relation between the deposited energy in an elastic scattering event and the DM mass (rule-of-thumb). Examples for different detection channels in the sub-GeV mass region are given.

When aiming to explore sub-GeV parameter space, there are multiple options. In the ∼MeV to ∼GeV mass scale, semiconductors and scintillators are possible detection channels. For example, the band gap of many semiconductors including Silicon (Si) and Germanium is on the order of eV. Semiconductors are therefore sensitive to scattering events including sub-GeV DM searches, such as light WIMP searches. In such experiments, TES are often used as the sensor attached to, or deposited on a semiconducting bulk target mass. The target volume is usually orders of magnitude larger than the TES detectors. An example for such a setup is the SuperCDMS experiment employing TES detectors in this manner [48]. Its aim is to look for DM scattering signals with the semiconducting target, which would result in secondary phonons and ionization, where a thermally-coupled TES chip is used to measure the depositions' thermal energy. Experiments based on scintillating targets, such as the CRESST experiment, function in a similar manner, where the TES is used to measure both scintillation light and energy in the phonon system [49]. By comparing the population of both signals in the TES detector, different scattering particle sources can be identified. These are just two examples, but TES are already widely used in further types of direct DM experiments such as EDELWEISS [50], COSINUS [51], and TESSERACT [52]. However, these experiments always include TES chips for sensing, which are coupled to separate active targets. When aiming to explore sub-MeV mass regions, targets such as semiconductors,

lose sensitivity to energy depositions below the eV-scale. This scale fits to the scale of binding energies of Cooper pairs (∼meV), which are the dominant state of electrons in superconductors below their critical temperature T_C. If a DM particle with sub-MeV mass scatters with an electron in a superconductor in its superconducting equilibrium state, quasi-particle and phonon excitations follow, whose energy can be measured before the superconductor relaxes back to its equilibrium state. The same process applies for the detection of photons as well, which many superconducting detectors are primarily used for. Therefore, within its linear region the detection process is independent of the nature of the particle and the measured signal depends on the deposited energy only. While the operation of superconducting detectors for light DM searches is a fairly new concept [53], the Superconducting Nanowire Single Photon Detector (SNSPD) is a prime example for this method. SNSPDs are single photon detectors originally developed for quantum information science [54]. A superconducting material is etched in a meandering pattern onto a substrate, where single stripes of the pattern on the nanometer-scale represent the nanowires. The SNSPD is cooled below its critical temperature and stays in an equilibrium position by applying the proper bias current. Depending on its properties, the SNSPD has a threshold energy above which it is sensitive, for the infrared case on the order of eV. When a single photon or DM particle impacts the nanowire, it is absorbed, Cooper pairs break and a hotspot forms due to the heating of the surrounding material. This hotspot then grows across the sensor and suppresses the superconductivity, which results in a changing resistance, which can be readout as a voltage signal after some amplification. SNSPDs however function mostly as counting devices so far and therefore no information about the energy of the initial deposit is conserved, except for the fact, that it surpasses the device's energy threshold.

In a first generation experiment, SNSPDs have been used to explore and set limits on the DM-electron scattering parameter space, by using them as target and sensor simultaneously [47, 55]. If the same amount of energy is deposited, the particle's properties are irrelevant and scattering of a DM particle with the SNSPDs electron system will result in signal just as for a photon interaction. Compared with kilogram or even ton-scale targets used for DM-nucleon scattering experiments, the mass-scale of detection setups with a superconducting target is orders of magnitude smaller (so far), due to increased noise levels at larger areas. The properties of the first generation SNSPD device are listed in Tab. 1.1. This simple

mass	**duration**	**material**	**threshold energy**	**active volume**
4.3 ng	180 h	WSi	0.73 eV	$7\,\mathrm{nm} \times (400\,\mu\mathrm{m})^2$

Tab. 1.1.: Properties of the first generation SNSPD experiment employed for DM-electron scattering searches in Ref. [55].

first generation experiment, without optimization and with an exposure of about a week,

was already able to set new constraints in the DM-electron scattering parameter space (more details in Sec. 4.4). This exemplifies, that even with comparatively small exposure, superconductors are able to set competitive limits on the DM-electron scattering parameter space. This is possible, since no signal was measured in the above-mentioned device. Therefore, constraints are simply based on the fact, that no signal was recorded within the measurement time. Considering this and the options to improve sensitivity in scattering experiments described in Sec. 1.1, the sensitivity to lower DM masses can be influenced mainly by lowering the energy threshold of the device[2]. Since this can increase the amount of background and dark counts[3], whose origin is non-trivial, an energy-resolving device would enable dedicated background investigation and mitigation. Therefore, employing energy-resolving detectors instead, is a natural next step and is imperative to actual DM detection opposed to experiments setting limits on the parameter space only. With an energy-resolving experiment, the resulting energy spectrum can also be compared to the expected signal rate based on DM interactions. Therefore, employing superconducting detectors for competitive DM searches and detection needs the following:

- good energy resolution ($\sim$100 eV below 1 eV)
- low dark count rate
- low energy threshold ($<$1 eV)
- long exposure ($>$ days)

Therefore, as originally proposed for superconducting detectors, the same approach used for SNSPDs could be tested using existing TES infrastructure, as well. The TES detection system of the ALPS II experiment already provides such an infrastructure. It includes the detection modules housing two TES chips, optimized for 1064 nm each, including readout via SQUID chips. Many of these needed properties already match the ones determined at 1064 nm (1.165 eV) in the effort of optimizing the TES system for single-photon detection in the ALPS II experiment, such as low dark counts. However, these properties will need to be investigated at a broader energy range, as well. The exact status of ALPS II's TES system will be further discussed in Sec. 1.3.1.

Considering these points, ALPS II's TES detection system can be used to perform a proof-of-principle DM search, to verify the suitability of TES detectors for such endeavors and aim to explore the DM-electron scattering parameter space. For this purpose, both the ALPS II experiment, its TES detection system and the most important points regarding the working principle of TES sensors must be considered, before understanding how to determine the DM interaction rate with a TES.

[2]This was successfully performed with a second generation SNSPD device, see Ref. [56], covered in Sec. 4.4.
[3]Dark counts are detection events measured even when the detector is not directly exposed to any light or particle sources.

1.3 Transition Edge Sensors

Before discussing TES as DM detectors, the ALPS II experiment and the corresponding performance aspects of its TES system are considered. Subsequently, the most important points regarding the physics of TES in general will be discussed, mainly following the description in Ref. [57]. The goal is to understand the working principle of TES and the expected signal shapes of small energy depositions in the material, e.g. from a single photon. Based on this, an expression used to fit such signals analytically is derived following [57, 58].

1.3.1 TES in the ALPS II Experiment

The TES system used in this thesis is based on the research and development of a TES detection system for the ALPS II experiment. Since much of the work towards enhancing and understanding this setup has already been done in the context of optimizations for measurements with ALPS II, the base principles and aim of the experiment will only be discussed shortly, as well as a short discussion of the current status of TES detection system. Detailed explanations of the ALPS II experimental setup are found in Ref. [59–63] and on the TES system for ALPS II in Ref. [17, 18, 58, 64–69]. More details on the TES detectors, cryogenic cooling and Data Acquisition (DAQ) setup are discussed in Ch. 2.

The ALPS II experiment (see Ref. [59]) is a LSW experiment aiming to produce and detect axions and Axion Like Particle (ALP)[4]. The $L \approx 250\,\mathrm{m}$ long experiment, was assembled in the HERA[5] accelerator tunnel at DESY in Hamburg, Germany[6]. The experiment not only reuses the HERA infrastructure, but is also built out of 24 straightened superconducting dipole magnets [59]. In a simplified picture[7], 12 of these $B = 5.3\,\mathrm{T}$ magnets are each placed on one side of a light-tight wall. The setup, shown in Fig. 1.3, also includes a high-power laser system on the left side of the wall, that shines a 1064 nm infrared laser into an optical cavity placed inside the left magnet string. The laser light's power is increases manifold inside the optical cavity, called production cavity, such that, assuming an axion-photon coupling $g_{a\gamma\gamma}$, single photons will couple to virtual photons provided by the magnetic field to turn into an ALP. Due to the light-tight wall, photons are not able to reach the second magnet string, including second optical cavity. ALPs converted from photons however, due to their very weak interaction with normal matter, can cross this barrier and enter the second magnetic field and cavity on the right-hand side of the wall. Within this cavity, the ALPs undergo the time-reversed process with a probability enhanced by the cavity as well and decay into two photons, of which one is the virtual photon of the magnetic field again.

[4] Axion-like particles resembling axions in many aspects, but not able to solve the strong CP problem.
[5] Hadron-Elektron-Ring-Anlage, former circular particle accelerator with a circumference of ∼6 km.
[6] Using the HERA infrastructure in a similar context was first proposed in Ref. [70].
[7] The complexity of the optical setup exceeds this description and is described in detail eg. in Ref. [62].

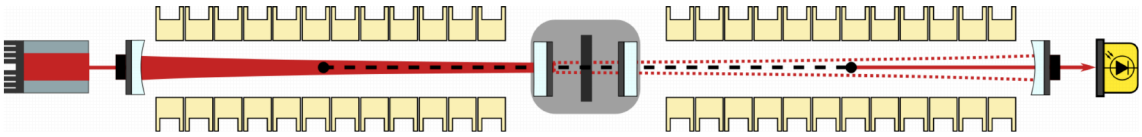

Fig. 1.3.: ALPS II experimental setup. A high power infrared laser shines light into an optical cavity (production cavity) placed inside a long magnetic field. The laser power is built up inside the cavity and, in combination with the magnetic field strength, able to produce ALPs with a certain probability. A light-tight wall in the center of the drawing hinders photons to cross the barrier, which is transparent to ALPs. ALPs traveling through the barrier enter the regeneration cavity, where they decay back into a photon with a certain probability, as well. Consequently, these photons can be detected.

The second optical cavity is therefore called regeneration cavity. Measuring this photon behind the light tight wall, could prove the existence of a possible DM candidate.

The probability for the combined processes (production and regeneration) to happen consecutively, scales with the axion-photon coupling, the magnetic field strength B and the length of the magnetic fields L:

$$P_{\gamma \to a \to \gamma} \propto g_{a\gamma\gamma}^4 B^4 L^4 \tag{1.2}$$

For $g_{a\gamma\gamma} = 2 \times 10^{-11}\,\mathrm{GeV}^{-1}$ and with the optical cavities and specialized laser systems of the ALPS II setup, this probability warrants two expected reconverted photons per day. The challenge is to measure such a low flux of reconverted photons precisely and reliably. Since the first science run of ALPS II in 2023 employing only the regeneration cavity for now (this changes the $g_{a\gamma\gamma}$ the setup is sensitive to), the experiment has been successfully using a so-called heterodyne sensing scheme [71] to detect photons in the regeneration cavity. This method is based on finding a beat-note in two mixed frequencies originating from a local oscillator laser in the regeneration cavity and the signal frequency of a reconverted photon. Therefore, the method relies on the wave-like characteristics of a photon. In the experiment's proposed original approach, a TES was supposed to exploit the particle nature of a reconverted photon by measuring the number of single-photons from the regeneration cavity.

Currently, the ALPS II experiment is aiming for a full science run, including the production cavity, where the reliable heterodyne sensing scheme will be employed again. Research optimizing and enhancing both methods has been ongoing and TES detection for ALPS II remains a viable option complementing the heterodyne detection scheme. Especially in the case of a discovery or measurement of unexpected phenomena, the TES system could pose an alternative to dispel or prove possible hypotheses.

Within the efforts to optimize the TES detection systems, following favorable and often cutting-edge properties have been shown:

- intrinsic (non-fiber coupled) background of $6.9 \cdot 10^{-6}$ cps [67]

- >90 % system detection efficiency [65]
- energy resolution of $\sim 5\,\%$ [65]
- stable operation $> 20\,\mathrm{d}$

These numbers refer to measurements optimized for laser wavelengths of 1064 nm i.e. to a photon energy of 1.165 eV. While the intrinsic background without fiber connection to the ALPS II experiment already meets the sensitivity goal of $< 7.7 \cdot 10^{-6}\,\mathrm{cps}$ background rate (0.5 photons per day) [17], the extrinsic background arising in fiber-coupled setups[8] due to in-coupling black-body radiation from the outside, still needs to be reduced further to meet ALPS II requirements. However, the system is on a good way and exploring many different options of reducing its extrinsic background further, such as a cryogenic low-pass filter, fiber curling and optimized analysis methods [72]. Therefore, the TES system is expected to match these requirements within the next years.

Especially, the reported low rate of dark counts show promise for employing TES in Dark Matter (DM) searches. To understand how this system could be used in direct DM searches, the general working principle of TES needs to be considered in the following.

1.3.2 TES Working Principle

TES are based on the principles of superconductivity. When a metal is cooled to cryogenic temperatures its electrical resistance decreases. Certain materials, such as Tungsten (W), exhibit superconducting features below its critical temperature T_C, where the temperature dependent resistance $R(T)$ drops to zero. For the W-TES films used in this thesis, the critical temperature is about 140 mK. However, between the superconducting state and the normal conducting resistance R_N, a steep transition curve exists, as the phase change between the two states is not instantaneous. When a superconductor is retained on this transition edge, e.g. by applying a suitable bias current I, it gets very sensitive to the smallest changes in temperature ΔT, resulting in a comparatively large increase in resistance ΔR. TES are superconducting thin films, generally operated on the transition edge between the two phases. The bias point is called the working point and is visualized on the superconducting transition curve in Fig. 1.4. Therefore, TES are widely used as superconducting micro calorimeters of thermal capacitance C, where the change in temperature is proportional to the energy ΔE deposited in the sensor:

$$\Delta T = \Delta E / C. \tag{1.3}$$

[8] Fiber-coupled setup refers to measurements, where photons are coupled into a fiber and routed into the cryostat housing the TES detector. There, the fiber would be directly coupled with the TES as well.

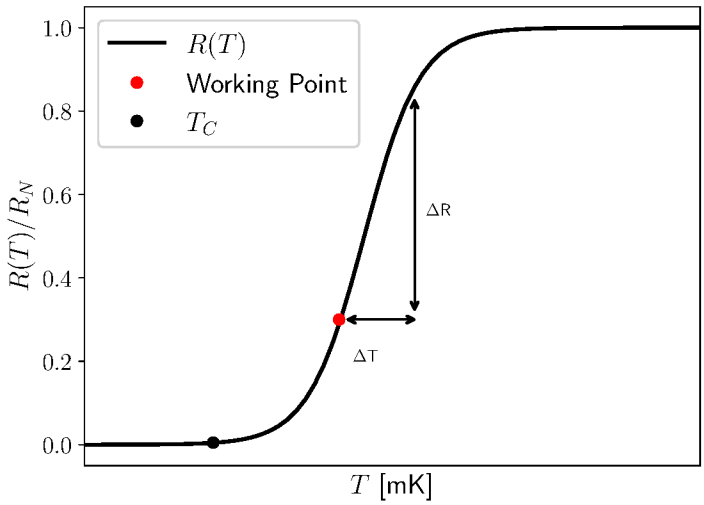

Fig. 1.4.: Representation of a transition region between the superconducting state (below $\sim T_C$), where the $R(T_C) = 0$, and the normal-conducting state, where $R(T)$ is equal to the normal-state resistance (R_N). The TES operates in this region, and a working point (red) can be selected on the steep slope between the two conductive states. A small temperature change, ΔT, on the order of millikelvin, results in a relatively large change in resistance, ΔR, on the order of Ohms. This configuration exhibits a strong sensitivity to small temperature changes, making it ideal for temperature-sensing applications.

Depending on the critical temperature, the change in temperature can therefore already be induced e.g. by single photons or other particles with energies below $\sim 1\,\text{eV}$. Therefore, TES technology is widely used as one of the most sensitive photon-number resolving detectors.

Exploiting this superconducting transition edge for detection methods was first demonstrated by measuring infrared signals in 1942 by Ref. [73], already. Especially within the last decades, they have been established as detector solutions across many different fields from large-scale applications in astrophysics such as earth-based Cosmic Microwave Background (CMB) observations at the Atacama Cosmology Telescope [74], to small-scale applications in biophysics such as cell imaging [75].

1.3.3 Small Signal Theory

To understand the detectors response not only to photons, but also other possible energy depositions, such as recoil energy from DM scattering, a description for the current response of a TES circuit to a small energy deposition will be derived. This description closely follows the Small Signal Theory (SST) description of Ref. [57].

The TES is usually cooled below its critical temperature by a weak coupling to a thermal bath with conductance G. By applying a bias current, the TES temperature increases

and settles around the respective working point. When energy is deposited and the TES temperature increases, the bath cools the TES down to the working point again. This cooling happens based on the thermal time constant τ defined as:

$$\tau = \frac{C}{G}, \tag{1.4}$$

with an exponential decrease of the temperature with time t depending on this time constant

$$T(t) \propto \exp\left(\frac{-t}{\tau}\right). \tag{1.5}$$

The circuit diagram of a TES, in simple terms, is represented by the temperature and current dependent TES resistance R_{TES}, an applied bias voltage V_{bias}, a coil with inductance L (used for SQUID readout) and a load resistance R_L representing the combined shunt and parasitic resistances $R_L = R_{\mathrm{SH}} + R_{\mathrm{PAR}}$, see Fig. 1.5. When omitting additional noise

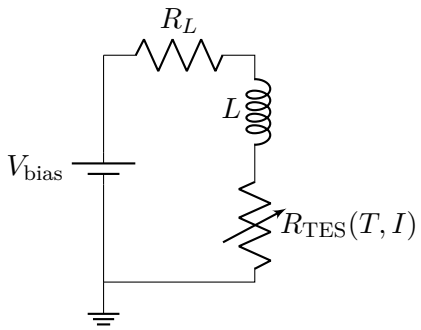

Fig. 1.5.: Simplified TES circuit representation showing a bias voltage V_{bias} applied to a series including a coil with inductance L, a load resistor R_L and the TES with resistance R_{TES}. Diagram adapted from Ref. [57].

terms, the TES response can be described by a thermal, as well as an electrical differential equation, describing the thermal and electrical response of a TES, respectively:

$$C\frac{\mathrm{d}T}{\mathrm{d}t} = -P_{\mathrm{bath}} + P_J + P \tag{1.6}$$

$$L\frac{\mathrm{d}I}{\mathrm{d}t} = V - IR_L - IR_{\mathrm{TES}}(T, I). \tag{1.7}$$

with the signal power P, Joule power dissipation P_J in the TES film and the power flow to the thermal bath P_{bath}. Due to Joule heating and subsequent power dissipation as well as the weak link to the thermal bath, the TES temperature is always above T_{bath} when biased. When assuming a small signal, it can be represented by an incident delta-function,

inducing a small temperature change δT compared to the steady state. An approximation of the power flow to the thermal bath for small signals is given by

$$P_{\text{bath}} \approx P_{J_0} + P_0 + G\delta T \tag{1.8}$$

with the Joule power $P_{J_0} = I_0^2 R_0$ and signal power P_0 of the steady state. Due to the small temperature change, the TES resistance can be expanded to

$$R_{\text{TES}}(T, I) \approx R_0 + \left.\frac{\partial R}{\partial T}\right|_{I_0} \delta T + \left.\frac{\partial R}{\partial I}\right|_{T_0} \delta I, \tag{1.9}$$

with $\delta I = I - I_0$. The steady state parameters I_0, T_0 and R_0 represent the values when a TES is biased at its working point (see Fig. 1.4). Next, the temperature sensitivity α_I and current sensitivity β_I of a TES dependent on the steady state parameters can be defined as

$$\alpha_I = \frac{T_0}{R_0} \left.\frac{\partial R}{\partial T}\right|_{I_0} \tag{1.10}$$

$$\beta_I = \frac{I_0}{R_0} \left.\frac{\partial R}{\partial I}\right|_{T_0}. \tag{1.11}$$

When plugging the sensitivities introduced in Eq. 1.10 and 1.11 into Eq. 1.9, the resistance takes the following form

$$R_{\text{TES}}(T, I) \approx R_0 + \alpha_I \frac{R_0}{T_0} \delta T + \beta_I \frac{R_0}{I_0} \delta I, \tag{1.12}$$

which can also be used to expand the Joule power:

$$P_J = I^2 R \approx P_{J_0} + 2J_0 R_0 \delta I + \alpha_I \frac{P_{J_0}}{T_0} \delta T + \beta_I \frac{P_{J_0}}{I_0} \delta I. \tag{1.13}$$

By introducing the electrical time constant of the bias circuit

$$\tau_{\text{el}} = \frac{L}{R_L + R_0(1 + \beta_I)}, \tag{1.14}$$

the low-frequency loop gain $\mathcal{L}_I = \frac{P_{J_0} \alpha_I}{G T_0}$ for a constant current and the current biased thermal time constant

$$\tau_I = \frac{\tau}{1 - \mathcal{L}_I}, \tag{1.15}$$

a set of linearized differential equations can be derived from Eq. 1.6 and 1.7, by combining them with Eq. 1.8, 1.12 and 1.13. These coupled equations describe the TES response based on its electrical and thermal circuit including small variations δV and δP

$$\frac{\mathrm{d}}{\mathrm{d}t}\delta I = -\frac{1}{\tau_{\mathrm{el}}}\delta I - \frac{\mathcal{L}_I G}{I_0 L}\delta T + \frac{1}{L}\delta V \tag{1.16}$$

$$\frac{\mathrm{d}}{\mathrm{d}t}\delta T = \frac{I_0 R_0(2+\beta_I)}{C}\delta I - \frac{1}{\tau_I}\delta T + \frac{1}{C}\delta P. \tag{1.17}$$

It is important to note, that a TES circuit can be biased in two ways, either via keeping a constant voltage (voltage-biased) or by keeping a constant current (current-biased). When keeping the TES circuit at a constant voltage an effect called negative Electro-Thermal Feedback (ETF) can be exploited. When the temperature increases due to an energy deposition, the resistance increases as well. For voltage-biased circuits ($R_L \ll R_0$) this leads to a reduction in Joule power dissipation, which renders it stable against thermal runaway. On the other hand, current-biased circuits, where $R_L \gg R_0$, result in an increase in P_J, called positive ETF. Since the negative ETF supports the relaxation to the steady state, it is the favorable mode for TES circuit biasing and ensures stable measurements as well as fast signals. This holds especially true for the strong negative ETF, where $\mathcal{L}_I \gg 1, \beta_I$. For this case, the ETF energy can be described by the TES bias voltage V_{TES} and the small variation in the current:

$$E_{\mathrm{ETF}} = -\int_0^\infty V_{\mathrm{TES}}\delta I(t)\,\mathrm{d}t \approx -V_{\mathrm{TES}}\int_0^\infty \delta I(t)\,\mathrm{d}t\,, \tag{1.18}$$

Therefore, E_{ETF} is only dependent on the changes over time of δI induced by the initial energy deposition.

To properly describe δI and therefore the signal shape, a solution to Eq. 1.16 and 1.17 needs to be approximated. A homogeneous solution to the differential equations is presented in Ref. [76] by applying a change of variables approach and taking $\delta V = \delta P = 0$. The eigenvalues of the homogeneous solution of Eq. 1.16 and 1.17 are

$$\frac{1}{\tau_\pm} = \frac{1}{2\tau_{\mathrm{el}}} + \frac{1}{2\tau_I} \pm \frac{1}{2}\sqrt{\left(\frac{1}{\tau_{\mathrm{el}}} - \frac{1}{\tau_I}\right)^2 - 4\frac{R_0\mathcal{L}_I(2+\beta_I)}{L\tau}}, \tag{1.19}$$

which are the inverse of the rise and decay time constants of the signal pulse, where the decay time represents the return time to the steady state. For a small energy deposit, instant thermalization is assumed leading to the following initial conditions:

$$\delta T(0) = \Delta T = \frac{\Delta E}{C},\ \delta I(0) = 0. \tag{1.20}$$

Therefore, the current and thermal response to a deposited energy of temperature ΔT for $t \geq 0$ are the solutions of the differential equations in Eq. 1.17 and 1.16:

$$\delta I(t) = \left(\frac{\tau_I}{\tau_+} - 1\right)\left(\frac{\tau_I}{\tau_-} - 1\right)\frac{1}{2+\beta_I}\frac{C\Delta T}{I_0 R_0 \tau_I^2}\frac{\exp\left\{\frac{-t}{\tau_+}\right\} - \exp\left\{\frac{-t}{\tau_-}\right\}}{1/\tau_+ - 1/\tau_-} \tag{1.21}$$

$$\delta T(t) = \left(\left(\frac{1}{\tau_I} - \frac{1}{\tau_+}\right)\exp\left\{\frac{-t}{\tau_-}\right\} + \left(\frac{1}{\tau_I} - \frac{1}{\tau_-}\right)\exp\left\{\frac{-t}{\tau_+}\right\}\right)\frac{\Delta T}{1/\tau_+ - 1/\tau_-}. \tag{1.22}$$

Based on the current response, the amplitude of the pulse can then be written as

$$A = \left(\frac{\tau_I}{\tau_+} - 1\right)\left(\frac{\tau_I}{\tau_-} - 1\right)\frac{1}{2+\beta_I}\frac{C\Delta T}{I_0 R_0 \tau_I^2}\frac{1}{1/\tau_+ - 1/\tau_-} \tag{1.23}$$

leading to the simplified form:

$$\delta I(t) = \begin{cases} A\left[\exp\left\{\frac{-t}{\tau_+}\right\} - \exp\left\{\frac{-t}{\tau_-}\right\}\right], & \text{if } t \geq 0 \\ 0, & \text{else.} \end{cases} \tag{1.24}$$

This equation represents the current response of a TES in the small signal limit and can be used to derive the signal shape of an amplified TES signal in the next section. Considering Eq. 1.19, when the inductance of the coil L is small, $\tau_+ \ll \tau_-$ holds and it follows for the time constants:

$$\tau_+ \to \tau_{\text{el}} \tag{1.25}$$

$$\tau_- \to \tau\frac{1 + \beta_I + \frac{R_L}{R_0}}{1 + \beta_I + R_L/R_0 + (1 - R_L/R_0)\mathcal{L}_I}. \tag{1.26}$$

At last, the TES signal shape is also influenced by internal noise sources, which consequently influence and limit the fundamental energy resolution of the TES. In short, the resolution-limiting noise consists mainly of phonon noise (or Thermal Fluctuation Noise (TFN)) and Johnson-Nyquist noise, based on the random propagation of phonons and thermal motion of electrons influencing the resistance, respectively. Following Ref. [77], the fundamental limit of the energy resolution given by the full width at half maximum is

$$\Delta E_{\text{FWHM}} \approx 2.36\sqrt{4k_B T_0^2 C\frac{1}{\alpha_I}\sqrt{\frac{n}{2}}} \tag{1.27}$$

with the Boltzmann constant k_B and n depending on the thermal impedance between the heat bath and the TES. Therefore, the energy resolution improves for lower thermal capacitance and higher temperature sensitivity, but worsens for higher working points, equaling a higher steady state temperature T_0.

1.3.4 SQUID Readout and Signal Shape

For readout and amplification, most TES applications rely on SQUID technology, or in more detail DC-SQUIDs [78]. SQUID theory and working principles especially for the setup used in this thesis, have already been discussed extensively in Ref. [17, 18]. SQUIDs are ultra-sensitive magnetometers, functioning as current amplifiers, operated at cryogenic temperatures similar to the TES. Some of their favored properties include low power dissipation and low noise characteristics. They represent a prime choice for the readout of many low frequency applications such as gravitational wave searches [79] and even magnetic resonance imaging [80].

While TES films usually need temperatures closer to absolute zero, SQUID chips can already be operated at around 4 K and retain their properties down to lower temperatures, as well. By connecting the SQUID via wires routed through the cold, they can be biased from room-temperature with a bias current I_{bias} used to monitor the voltage output and supply a feedback flux. Details on the DAQ setup used for this purpose within this work are discussed in Sec. 2.3. The coil in the TES circuit shown in Fig. 1.5 is used for the amplification and readout. The case of a voltage-biased TES in strong negative ETF is considered. For realizations of this circuit, a shunt resistor is usually located on the TES

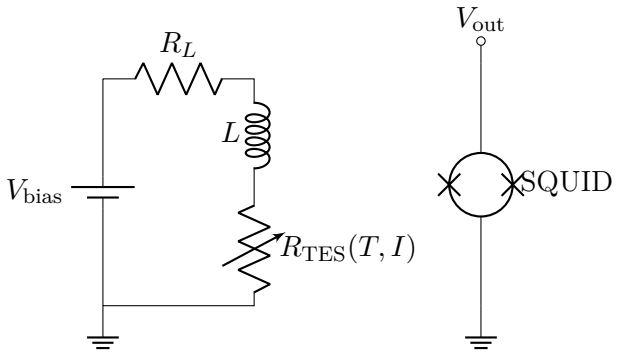

Fig. 1.6.: Simplified TES circuit representation with SQUID readout. The TES is biased via a voltage source V_{bias} and represented as a variable resistance depending on temperature T and current I flowing through the device. Magnetic flux changes due to changing current flowing through the coil with inductance L is sensed by the SQUID acting as a sensitive magnetometer.

chip, while the input coil is part of the SQUID chip. The two chips are usually wire-bonded to each other.

A bias current I_{bias} leads to variations in the magnetic flux of the superconducting loop. A DC-SQUID contains two weak links, which are part of the superconducting loop e.g. as insulators, forming Josephson-Junctions, which enable tunneling above the critical current of the junctions [81]. The magnetic flux variations then lead to a voltage swing across these junctions, defined by the magnetic flux quantum $\phi_0 = \frac{h}{2e} \approx 2.07 \cdot 10^{-15}\,\text{Wb}$, representing

the period of the voltage swing. The magnetic flux variations and their correlation to the voltage swing across the junctions is depicted in Fig. 1.7. A working point for the SQUID

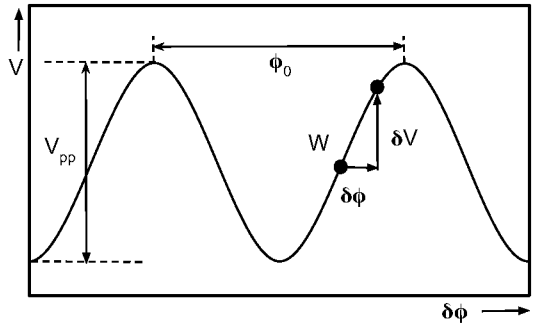

Fig. 1.7.: V-ϕ characteristic of a SQUID amplifier. W is the working point, V_{pp} is the peak-to-peak voltage and ϕ_0 the period. Linearity around the working point is only given for small values of $\delta\phi$. Adapted from Ref. [78].

is chosen in the linear regime of the $V-\phi$-characteristic, equaling a maximized $\left|\frac{\delta V}{\delta \phi}\right|$.

For readout, the SQUID is inductively coupled to the TES via its input coil. The SQUID then enables the conversion of an input TES signal δI_{TES} into an output SQUID voltage given by:

$$\delta I_{\mathrm{TES}} = \delta V_{\mathrm{out}} \frac{M_{\mathrm{in}}^{-1}}{R_f M_f^{-1}}, \tag{1.28}$$

where M_{in}^{-1} is the inverse mutual inductance between the TES coil and the SQUID and a feedback circuit within the SQUID gives the feedback resistance R_f and inverse feedback coil mutual inductance M_f^{-1}. This negative feedback loop, called Flux-Locked Loop (FLL), enables a linearized response and improves the SQUID's dynamic range [82]. The bandwidth of the SQUID readout is given by the Gain Bandwidth Product (GBWP), which can be adjusted and is usually on the order of GHz.

A DC-SQUID chip usually consists of an array of SQUIDs to boost the output voltage swing [83], enabling the coupling to a room-temperature DAQ system. The SQUID array then effectively acts like one SQUID with a higher output signal.

Amplified TES Signal

Based on the current-amplification through a SQUID-chip coupled to a TES and the current response derived in Eq. 1.24, a (photon) signal measured at the readout, takes a distinct shape at the output mainly defined by an amplitude parameter and the rise and decay time

parameters τ_+ and τ_-. At the voltage output of a dedicated DAQ system, discussed in Sec. 2.3, this would result in:

$$\delta U_{\mathrm{SST}}(t) = \begin{cases} A_{\mathrm{SST}} \left[\exp\left\{ \left(\frac{-(t-t_0)}{\tau_+} \right) \right\} - \exp\left\{ \left(\frac{-(t-t_0)}{\tau_-} \right) \right\} \right], & \text{if } t \geq t_0 \\ 0, & \text{else} \end{cases} \tag{1.29}$$

with the amplitude in the case of the small signal limit A_{SST}, as well as t_0 defining the start time of the pulse. This signal shape is shown in Fig. 1.8 (for a negative voltage output).

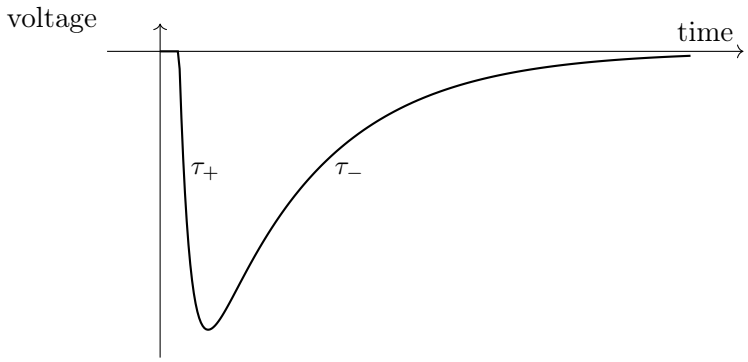

Fig. 1.8.: Schematic of a TES signal pulse at the SQUID current amplifier output. The rising edge of the pulse is governed by τ_+, while the decaying edge of the pulse is governed by τ_- and represents the relaxation back to the steady state.

In [66] it was shown that the alternative approach to the SST-form is a continuous fitting function describing the pulse phenomenologically, see Eq. 1.30, which showed a good fit to the TES signal shape.

$$U_{\mathrm{ph}}(t) = V_0 - \frac{2A_{\mathrm{ph}}}{\exp\left[-\frac{(t-t_0)}{\tau_{\mathrm{rise}}}\right] + \exp\left[\frac{(t-t_0)}{\tau_{\mathrm{decay}}}\right]} \tag{1.30}$$

Here τ_{rise} and τ_{decay} correspond to the rise and decay times of the signal pulse, are however not equivalent to the SST parameters τ_+ and τ_-. A_{ph} is the phenomenological pulse amplitude and V_0 represents a voltage offset in the measured timeline. Sec. 3.1 will introduce a stable fit function based on Eq. 1.29, by performing a Fast Fourier Transformation (FFT). For selected analyses, the phenomenological approach in Eq. 1.30 will be used complementary as well.

1.3.5 TES for Dark Matter Searches

The goal of this thesis is to perform dedicated measurements with ALPS II's TES detection system to explore the TES potential of directly detecting DM. Considering the requirements to use superconductors for competitive DM searches introduced in Sec. 1.2, ALPS II's TES system already meets most of them as shown in Sec. 1.3.1. Additionally, a lower

energy threshold $< 1\,\mathrm{eV}$[9] is viable as well, since this is determined by the system's trigger level, which could be lowered to access energy depositions of lower energies[10], and noise. Therefore, it is important to understand how the interaction rate of DM with the TES sensor is calculated, this rate will be used to determine the sensitivity of dedicated TES DM searches to mass-dependent DM-electron scattering cross-sections in Sec. 4.

To calculate the DM interaction rate with a TES, the loss function formalism is used. This section follows the formalism's introduction for superconducting detectors such as SNSPDs and TES in Ref. [84] and [85], and follows the calculation of the interaction rate regarding SNSPDs [55].

When scattering with electrons is considered, they cannot simply be assumed to be free particles in the respective material. Possible screening effects need to be taken into account, which can complicate underlying calculations. To simplify this, the scattering of DM particles in a material, is determined by the dielectric loss function

$$\mathcal{W}(\mathbf{q},\omega) = \mathrm{Im}\left(\frac{-1}{\epsilon_L(\mathbf{q},\omega)}\right), \tag{1.31}$$

which depends on the material's longitudinal dielectric permittivity $\epsilon_L(\mathbf{q},\omega)$, the momentum transfer $\mathbf{q}$ and deposited energy ω.

In the case of DM particles scattering with electrons, the Lindhard model [86] is used to determine the material's dielectric permittivity. The model is used to determine effects arising from the screening of electric fields in solid materials and can be calculated based on the plasma frequency

$$\omega_p = \sqrt{\frac{4\pi\alpha n_e}{m_e}}, \tag{1.32}$$

with the electron number density n_e, fine structure constant α and electron mass m_e. In the limit of low temperatures it can be calculated as

$$\epsilon_L(\mathbf{q},\omega) = 1 + \frac{3\omega_p^2}{\mathbf{q}^2 v_F^2}\left[\frac{1}{2} + \frac{k_F}{4\mathbf{q}}\left(1-Q_-^2\right)\log\left(\frac{Q_-+1}{Q_--1}\right) + \frac{k_F}{4\mathbf{q}}\left(1-Q_+^2\right)\log\left(\frac{Q_++1}{Q_+-1}\right)\right]. \tag{1.33}$$

Further parameters needed for the calculation are the momentum k_F and velocity $v_F = \frac{k_F}{m_e}$, by which $Q_\pm$ are defined:

$$Q_\pm = \frac{\mathbf{q}}{2k_F} \pm \frac{\omega}{\mathbf{q}v_F}. \tag{1.34}$$

[9] Compared to ALPS II searches focusing on one wavelength (1064 nm[1.165 eV]) only.
[10] The limiting factor is the TES current noise at the voltage output.

The used Fermi energy for these calculations for W is $E_F = 7\,\mathrm{eV}$. The Lindhard function is resonant at the plasma frequency ω_p, which is infinitely sharp in the above form. Therefore, $\omega \to \omega + \frac{i}{\tau}$ is used instead, with τ as the excitation lifetime. This guarantees results arising from the loss function even for energy depositions far from the resonance peak. Here, $\tau^{-1} = 0.1\omega_p$ is used as the typical width for metals. The determined dielectric loss function is then used to calculate the target's response in an elastic scattering event. This is defined by the dynamic structure factor for spin-independent electron-scattering with the electron charge e, which depends on the loss function introduced in Eq. 1.31:

$$S(\mathbf{q},\omega) = \frac{2\mathbf{q}^2}{e^2}\,\mathrm{Im}\left(\frac{-1}{\epsilon_L(\mathbf{q},\omega)}\right) \tag{1.35}$$

Since it depends on the material-dependent loss function, the structure factor is material-dependent as well[11]. To determine the scattering rate, one needs to integrate over the dynamic structure factor from Eq. 1.35, as well as the DM-electron interaction potential $V(\mathbf{q})$:

$$\Gamma = \int \frac{\mathrm{d}^3}{(2\pi)^3}|V(\mathbf{q})|^2 S(\mathbf{q},\omega). \tag{1.36}$$

The energy deposited in the detector in such an interaction is

$$\omega_{\mathbf{q}} = \mathbf{q}\cdot\mathbf{v}_{\mathrm{DM}} - \mathbf{q}^2/2m_{\mathrm{DM}}, \tag{1.37}$$

given by the DM velocity $\mathbf{v}_{\mathrm{DM}}$ and mass m_{DM}. Using the reduced mass between the electron and the DM particle $\mu_{e,\mathrm{DM}}$ and the coupling constants of the mediator to the electron g_e and the DM g_{DM}, the reference cross-section for spin-independent DM-electron scattering via a mediator ϕ is given by

$$\bar{\sigma}_e \equiv \frac{1}{\pi}\mu_{e,\mathrm{DM}}^2 g_e^2 g_{\mathrm{DM}}^2/(m_\phi^2 + q_{0,e}^2)^2, \tag{1.38}$$

where $q_{0,e} \equiv \alpha\, m_e$ is the reference momentum for electrons. Finally, by combining Eq.1.36-1.38, this can be used to determine the expected event rate in the target material given by:

$$\mathcal{R} = \frac{\pi n_{\mathrm{DM}}\bar{\sigma}_e}{\mu_{e,\mathrm{DM}}^2}\int \frac{\mathrm{d}^3\mathbf{v}_{\mathrm{DM}}\mathrm{d}^3\mathbf{q}\mathrm{d}\omega}{(2\pi)^3}\, f_{\mathrm{DM}}(\mathbf{v}_{\mathrm{DM}}) \times \mathcal{F}(q)^2\, S(\mathbf{q},\omega)\delta(\omega - \omega_{\mathbf{q}}) \tag{1.39}$$

using the form factor for spin-independent scattering

$$\mathcal{F}(q) = (m_\phi^2 + q_{0,e}^2)/(m_\phi^2 + q^2), \tag{1.40}$$

the DM number density n_{DM} and the velocity distribution of DM $f_{\mathrm{DM}}(\mathbf{v}_{\mathrm{DM}})$.

[11] More details on the dynamic structure factor are found in Ref. [87]

This expected event rate for a DM-electron scattering experiment with a TES can be used to search for and constrain interactions with DM particles. Based on this, the feasibility of TES for DM searches will be tested in this work, specifically in Ch. 4 and 5.

2 General Experimental Setup

The following chapter describes the general experimental setup used to perform the TES measurements in this thesis. In order to perform these measurements, the TES detectors need to be cooled down to 25 mK, using a dilution refrigerator. The details on the cryogenic cooling of detectors (also called modules) are discussed in Sec. 2.1. The TES detector modules consist of TES chips wire-bonded to SQUIDs, enabling biasing and readout. This thesis focuses on the results acquired by measurements using two different modules, which are in general and in detail described in Sec. 2.2. Next, Sec. 2.3 discusses the used electronics and readout, before Sec. 2.4 finally describes the experimental setups used for the different measurement types.

2.1 Cryogenic Cooling

The critical temperature of the W TES chips used in this thesis, below which they exhibit superconducting properties, lies roughly around $\sim 140\,\mathrm{mK}$[1]. To operate the TES chips within their superconducting transition region, they require stable cryogenic cooling. For the TES chips to reach these temperatures, the cryogenic cooling needs to be cold enough for the unbiased TES to reach the superconducting state. Subsequent application of the TES bias current then enables the stable operation at a certain point within the superconducting transition region e.g. at $30\,\%\ R_N$. Considering the additional heat load of the sensor modules, SQUIDs and electronic equipment attached to the cold finger, temperatures of $\sim 30\,\mathrm{mK}$ are needed to reach the critical temperature within the TES circuit. In this setup, these extremely low temperatures are provided by a Bluefors SD dilution refrigerator[2]. These cryostats contain a mixture of ^{3}He and ^{4}He, providing the necessary cooling power for temperatures below 1 K. The system includes custom software with automatic cool-down and subsequent warm-up scripts and enables monitoring of temperatures (at the different stages) and pressures. Its vacuum can's general setup is shown in Fig. 2.1 and an in-depth system description has already been given in Ref. [17]. Cooling down from room temperature to base temperature ($< 30\,\mathrm{mK}$) usually takes a maximum of 24 h, the same goes for the warm-up process. A cool-down remains very stable concerning temperatures and pressures for at least 20 days, after which instabilities can be introduced by saturation of the active charcoal trap used to filter impurities from the circulating mixture.

[1] As claimed by NIST and confirmed through measurements.
[2] Situated in HERA hall West approximately two floors underground.

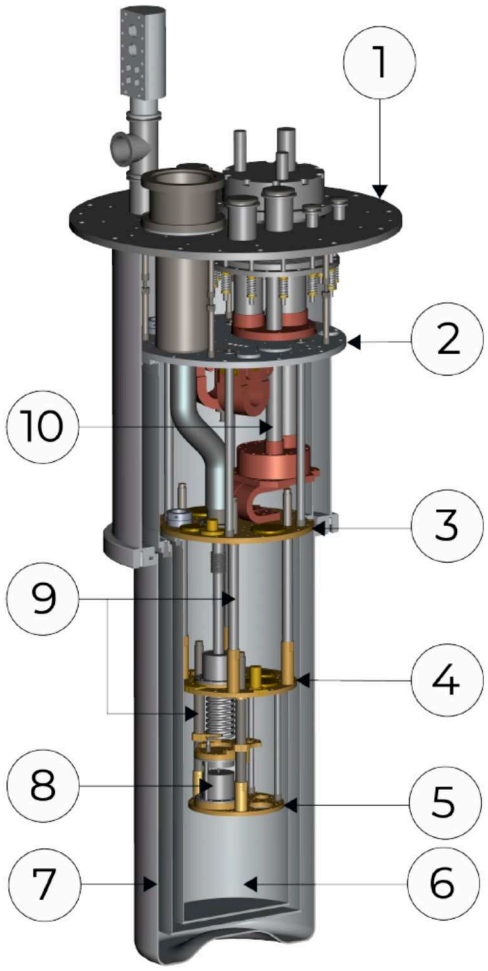

Fig. 2.1.: Schematic of the used Bluefors SD system dilution refrigerator. (1) Room temperature top flange (outside) (2) 50 K flange (3) 4 K flange (4) still flange (1 K stage) (5) MXC flange (25 mK) (6) coldest stage, where an additional coldfinger was installed (7) shielding layers (8) dilution unit (9) heat switches (10) pulse tube. Figure from Bluefors.

The oxygen-free copper cold finger where the TES modules are installed, described in detail in Section 2.2, is attached to the bottom of the Mixing Chamber (MXC) flange. A small amount of vacuum grease is applied between the cold finger mount and the MXC flange for maximized thermal connection between the cold parts. In turn, the TES module is tightly screwed to the cold finger using a small amount of vacuum grease for enhanced thermalization, as well. For additional shielding, a fitted aluminum can is attached to the bottom of the MXC flange, which completely encases the cold finger, TES module, and corresponding cabling and optical fibers.

2.2 TES Modules

The TES modules used in this thesis all share the same general layout, described in this section, followed by a detailed description of the differences between the TES modules used for DM searches in this thesis. One will be referred to as **TES D**, which is also used for ALPS II studies and the other is **TES F**, a module with an adjusted setup for DM searches, which will be considered in a preliminary study, as well. A summary of all modules used during the work for this thesis and their respective differences can be found in App. A.

2.2.1 TES and SQUID chips

The TES chips used in this thesis, provided by National Institute of Standards and Technology (NIST) (Boulder, CO, USA), are comprised of a racket-shaped Si-substrate chip, which houses the active W sensor in the center of the round disk and includes bonding pads for wire bonds on the handle, as seen in Figure 2.2a. The chip and active sensor shape

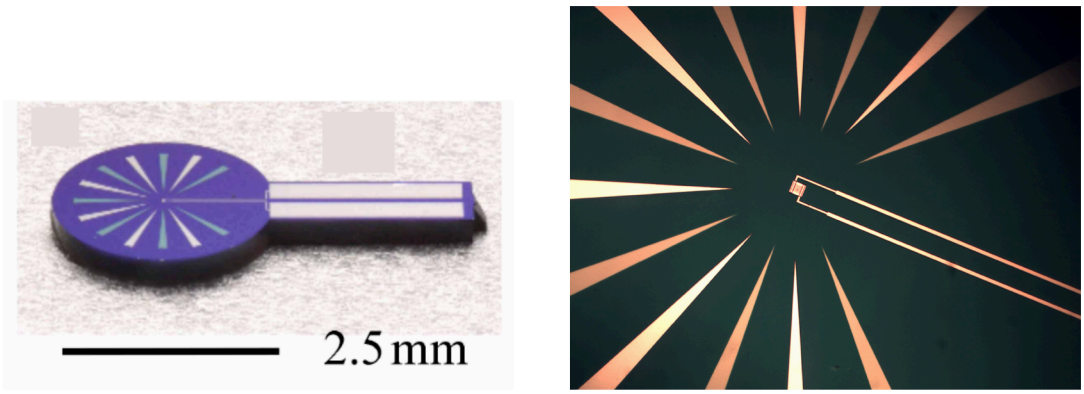

(a) (b)

Fig. 2.2.: (a) Side view of a NIST TES chip. The round part of the racket-shaped chip has a diameter of 2.5 mm with bonding pads for wire bonding on the long handle part below. The bright guiding stripes are pointing toward the active W sensor in the middle of the circular part. Image adapted from [88]. (b) Close-up view of the active TES sensor in the chip's center. The active sensor part has an area of $25{\cdot}25\,\mu m^2$.

is determined by the diameter of single-mode fiber ferrules and the size and position of their fiber core to enhance efficiency in fiber-coupled experiments [88]. The active sensor in the center of the disk has a tiny area of only $25 \times 25\,\mu m^2$ and a mass of 0.2 ng. Within this small-scale sensor, the active W film is embedded in an optical stack of dielectric materials. The exact deposit thickness of different layers, shown in Fig. 2.3, is optimized to enhance the absorption of 1064 nm photons and simultaneously reflect the majority of photons from other wavelengths.

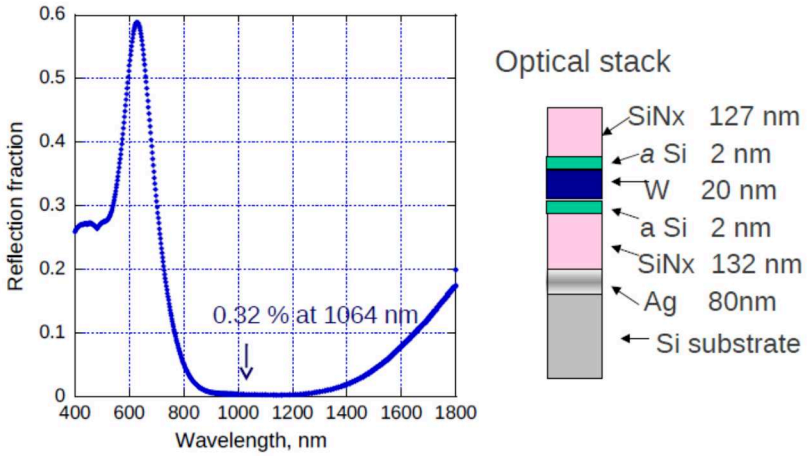

Fig. 2.3.: Left: Diagram showing the reflection fraction of the TES sensor, with an optical stack optimized for 1064 nm, for different wavelengths, showing a minimal reflection fraction around 1064 nm. Right: Assembly of the corresponding optical stack showing the different layers around the active W film, inlcuding amorphous Si (aSi) and Si nitride (SiNx). Image from A. Lita.

The layers of the optical stack include anti-reflective and non-absorbing SiNx layers, while the 20 nm thick W film is directly embedded in non-absorbing dielectric layers of amorphous Si. These layers are placed on a reflective Ag mirror and a Si substrate. This optimization leads to a quantum efficiency of $> 99\,\%$ for single 1064 nm photons. In addition, the composition of the multi-layer structure of the optical stack can be tuned in a way to optimize the detection efficiency for different wavelengths as well [89].

W is used as the active superconducting layer, due to the adjustability of its superconducting transition temperature, by optimizing the amount of α- and β-W phases. The superconducting transition temperature is defined by the combination of α- and β-W phases with a ratio of about $90\,\%$ α-W and $10\,\%$ β-W for the sensors used in this thesis. This leads to a critical temperature of ~ 140 mK. Further details of the device fabrication are discussed in [90]. To facilitate readout, wire-bonds connect the TES chips with SQUIDs. These are either single- or two-stage SQUID chips (depending on the module in question) with two channels each. The chips, provided and tested by Physikalisch-Technische Bundesanstalt (PTB) Berlin, have a size of ~ 3.5 mm $\times$ 3.5 mm and house both the input coil and shunt resistor of the TES circuit. While previous setups, and the majority of modules listed in App. A.2, used two-stage SQUIDs, the modules used for this thesis have been equipped with single-stage SQUIDs. Details are found in App. A.1.

2.2.2 Module Packaging

The detector modules used in this thesis are made of copper and gold-plated copper, housing both TES and SQUID chips. The TES chips provided by NIST come in a package, where

they are mounted on a sapphire rod using thermal grease and held in place by a zirconia fiber sleeve as shown in Fig. 2.4a. This method is originally used to enhance the coupling between the fiber core and TES chip for maximized system detection efficiency [88]. When the modules are fully assembled by PTB, the chip package in Fig. 2.4a is connected to the detector module using copper clamps (see Fig. 2.4b). In this configuration, the optical fiber tips can be carefully removed from the fiber sleeve (and therefore the entire module) again, which can simplify the installation into a cryostat. The SQUID chips are glued

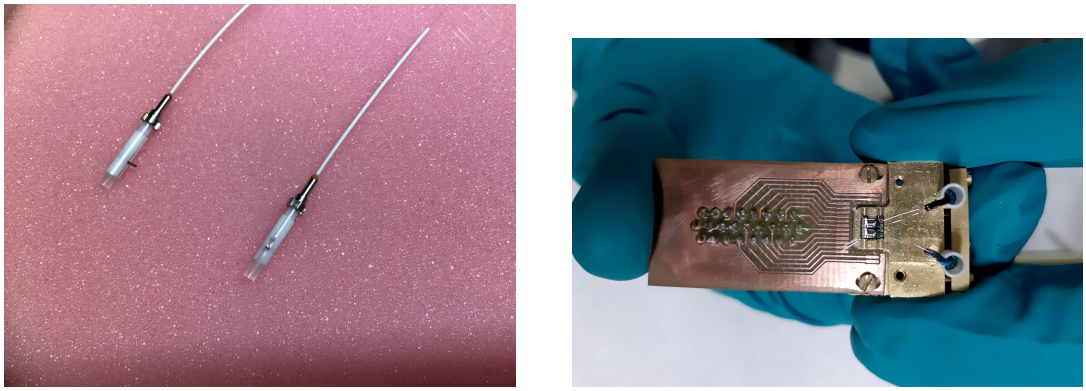

(a) (b)

Fig. 2.4.: (a) TES chips as packaged by NIST: The TES chip is placed on a (transparent) sapphire rod using thermal grease and kept in place by a (white) fiber sleeve, including an inserted fiber tip with a fiber during shipping. (b) Handheld view of the TES A module without fibers. Two racket-shaped TES chips are installed on the right side of the module, surrounded by zirconia fiber sleeves, wire-bonded directly to a two-stage SQUID chip. The SQUID chip is again wire-bonded to the module's readout electronics.

on the module[3] and the different bonding pads (for details, see Fig. A.2 in App. A.1), referring to specific circuit elements, are wire bonded to the module using aluminum wire bonds, enabling the contact to the readout described in Sec. 2.3. Additional wire bonds are bump-bonded to the TES chips, two for each chip, enabling the TES biasing and readout.

In the past, it proved to be problematic to find proper TES working points close to the superconducting state, since SQUID heating influenced the bath temperature and thus the TES chip's conductivity state. Therefore, a copper intermediate bonding pad was glued in between the SQUID chip and TES chips for one of the modules, which helps isolate the temperature-sensitive TES chips from excess power dissipated by the SQUID chip due to biasing. Both used TES modules are very similar, as they are equipped with the same type of TES and SQUID chips. The differentiating features, which are discussed in the following, are mainly related to the module architecture. A table including more details, also on other modules which have been used previously, is found in Tab. A.1 in the appendix.

[3] using GE 7031 varnish

2.2.3 TES Module D

The first module, which was used for this thesis, is TES module D. This module combines two features that differentiate it from previously used sensors in Ref. [17, 18, 58]. One is the above-mentioned intermediate copper bonding pad, which was added to reduce the additional heat load from the SQUID chip on the TES chips. The other differentiating feature is the use of a `C638_I15_X16FL` single-stage SQUID chip as opposed to using double-staged SQUIDs[4]. Fig. 2.5 shows a close-up of the module's top part including both TES chips and the SQUID chip. Before installing the SQUID chip on the module it was

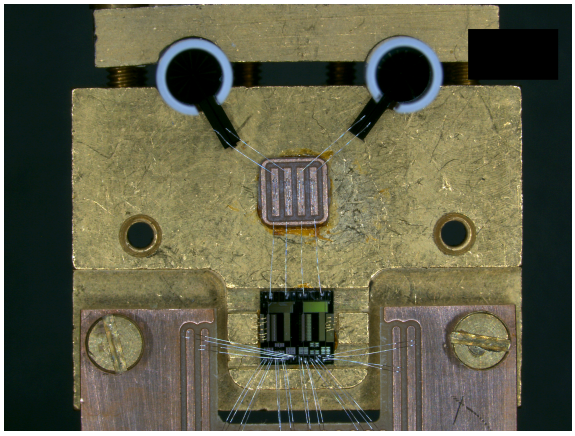

Fig. 2.5.: Closeup of TES module D recorded with a microscope. The racket-shaped TES chips placed within the Zirconia fiber sleeves are first wire-bonded to an interim copper bonding pad functioning as a heat-sink between the former and the SQUID chip.

tested at PTB at both 4.2 K and 0.3 K and the bias resistors were checked electrically. The two TES chips (`H7` & `H8`) from the same `TES101810` wafer, optimized for a wavelength of 1064 nm, were fabricated and provided by NIST. Furthermore, the readout is enabled by a MWDM-25 socket on the back of the module.

2.2.4 TES Module F

TES module F (see Fig. 2.6a) is a module with some unique characteristics specifically designed for the application in direct DM searches. According to simulations of the intrinsic background of other TES modules performed in [58], the zirconia fiber sleeves have been proposed as a main source of background. This background could be mitigated by either replacing the fiber sleeves with a radio-pure material or by removing them altogether, the latter presenting viable solution for DM searches, since fiber-coupling is no necessity. Module F is further equipped with a single-stage `C646 I14_A_B C6X216FB` SQUID chip

[4] Double-stage SQUIDs employ an additional SQUID for pre-amplification coupled to the front-end DC-SQUID. This additional stage leads to a more complicated setup when searching for SQUID working points. [78]

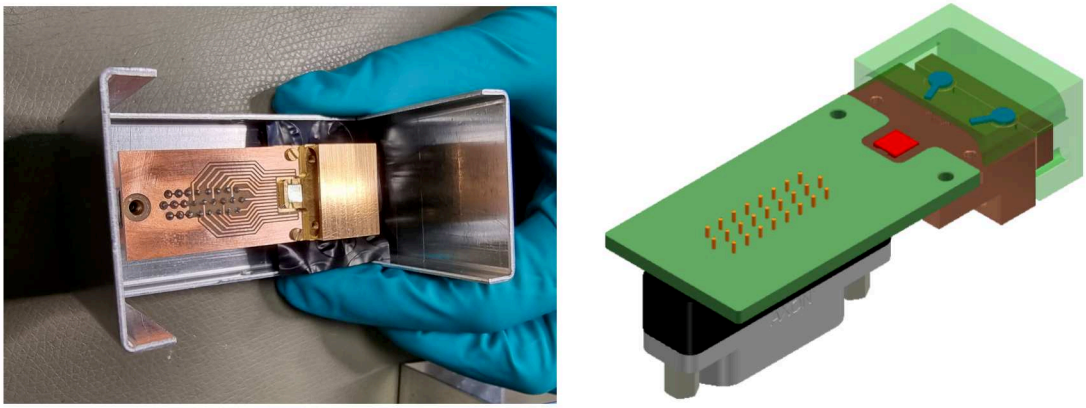

(a) (b)

Fig. 2.6.: (a) TES Module F as shown in its shipping package. From left to right the Printed Circuit Board (PCB) with the (shiny) SQUID chip is visible, followed by a protective copper cap covering both wire bonds and the TES chips, which are glued without fiber sleeves for this module. (b) Technical drawing of TES F showing the protective cap with the TES chips underneath.

and 1064 nm optimized TES chips (`A6` & `B9`) from the same wafer as TES D. Additionally, the readout is also enabled by a MWDM-25 socket on the module's back. However, TES F is not equipped with an intermediate bonding pad. The main difference to previously used modules is the placement of the TES chips on copper cylinders instead of sapphire ones due to the absence of zirconia fiber and alignment sleeves. Therefore, the copper cylinder is inserted into the module and the TES chip is glued[5] onto the cylinder, with the circular part aligning with the cylinder's top. Otherwise, the TES chips are placed in the same position as on previous modules. Due to the absence of the fiber sleeves, there is additional space to install a protective cap covering both the TES chips and the long wire bonds, connecting the TES chips with the SQUIDs. This is visualized in Fig. 2.6b. The protective cap does not only protect the device, especially during the process of installing it on the cold finger of the dilution refrigerator[6], but also acts as an additional shield from outside radiation e.g. from radioactive decays originating from non-pure materials within the setup. A summary of the differentiating features between the two modules is listed in Tab. 2.1.

	fiber sleeves	**TES chip placed on**	**chip fixated by**	**protective cap**
TES D	Zirconium	Sapphire	fiber sleeve/thermal grease	None
TES F	None	Copper	stycast glue	Copper

Tab. 2.1.: Comparison of modules TES D and F. Listed are the main features regarding the module architecture differentiating the two modules.

[5] using Stycast 1266 glue

[6] During the delicate process of uninstalling and installing new TES modules on the cold finger, wire bonds can accidentally be touched, broken or removed from the module.

2.3 Electronics and Readout

As mentioned above, the TES modules connected to the bottom of the cold finger include a Micro-D 25-pin connector (MWDM-25) with cryogenic and vacuum compatibility on their backside. A flat cable with a female Micro-D connector on each end connects the module to a custom Micro-D to Lemo 9 adapter attached to the bottom of the MXC flange. A feedthrough connects two CC-1 cryo-cables with Lemo connectors to the adapter, which are connected to one of the feedthroughs on top of the cryostat, after subsequent thermalization in different stages of the cryostat using e.g. copper clamps as thermal anchors. The lowest part of this setup is shown in Fig. 2.7. This cabling is used for powering and readout

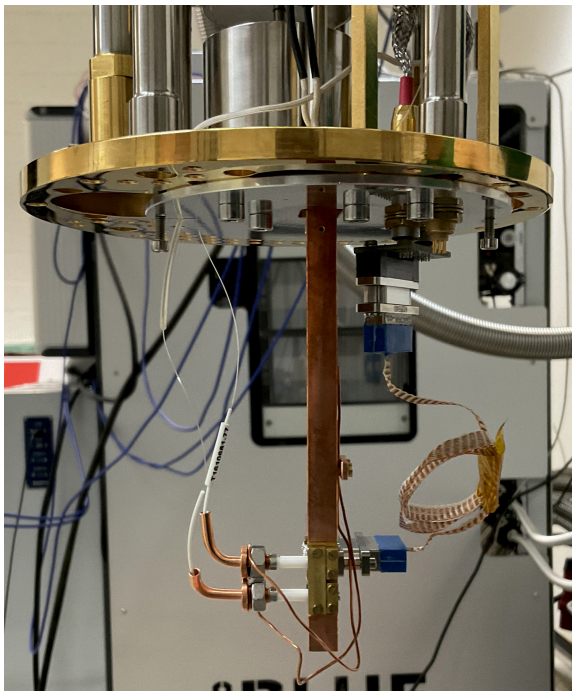

Fig. 2.7.: Side view of the cold finger with the installed TES D module. The adapters and cabling are visible on the right side of the cold finger, while the left side shows two optical fibers plugged into the TES module. The fibers are outfitted with copper heat sinks, connecting the fiber tips to the cold finger via copper wires to enhance their thermalization.

of both the TES and SQUID electronics using Magnicon's XXF-1 high-performance dc SQUID electronics system. A FLL electronics box is connected to the input connector in one of the cryostat's top flanges with another Lemo plug. On the other end of the FLL box another Lemo cable is connected to a connector box with outputs for connections with a PC (for SQUID and TES setup using the SQUIDViewer software) and multiple BNC signal output cables. Further integrated into the system is a CSE-1 (Current Source Extension) extension board, which is used for TES readout and bias. To set up a TES measurement, an I-V curve needs to be taken first, for which the SQUID electronics are bypassed using an IBox connected between the cryostat's top flange and FLL box. The details of SQUID

setup and locking, taking I-V curves, and biasing the TES have already been described in detail in Ref. [17] and [18]. The BNC signal output cables for channels one and two of the TES module can be connected via a BNC/Lemo adapter to an ATS9626 Alazar waveform digitizer, integrated into the DAQ computer, as the main component of the data acquisition system. The system has two input channels with a sampling frequency of up to 250 MHz per channel, 16-bit resolution, and both continuous timeline and triggered measurements can be operated using the custom AlazarGUI. Therefore, it is possible to set the desired trigger threshold, number of used processors for each measurement, duration of the measurement, etc. within the AlazarGUI.

Continuous Measurements: As the name suggests, these measurements record continuous timelines without any involved triggers. Therefore, the entire timeline and all noise and baseline fluctuations are recorded for the duration of the measurement. For very short measurement times, this already leads to large amounts of data. Therefore, this type of measurement is most suitable for short test measurements of up to a couple of minutes at most. For example: A 10 s background measurement at a sampling rate of 50 MHz already leads to a file size of 800 MB. However, it can be a suitable measurement mode e.g. for gauging the behavior of baseline noise.

Triggered Measurements: Triggered Alazar measurements involve the setting of a custom (negative) trigger level in mV and measurement duration. In this mode, only those timelines are recorded after which a trace of the signal crosses the trigger threshold. Each of these timelines is saved a certain time before and after the trigger crossing e.g. 30 µs before and 170 µs after the trigger. A new timeline is recorded and saved for each crossing of the trigger for the preset measurement duration. This is the preferred setting, especially for performing prolonged background and calibration measurements, where only those timelines with a sufficiently large background pulse are of interest.

2.4 Experimental Setups

For the different measurements performed within this thesis, different experimental setups are needed. The following section describes the differences and similarities between the setups. Both the setups for calibration measurements (Sec. 2.4.2) and the setups for direct DM measurements (Sec. 2.4.3) are variations of the standard setup (Sec. 2.4.1).

2.4.1 Standard (Fiber-Coupled) Setups

The standard experimental setup, shown in Fig. 2.8, represents the original setup intended for ALPS II research and measurements. In this standard configuration, two HI1060 optical

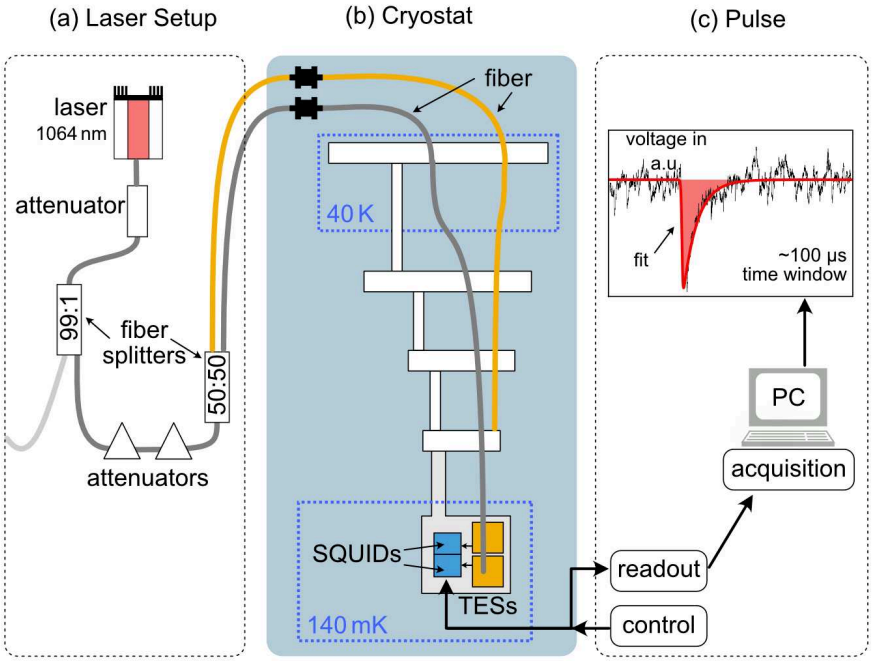

Fig. 2.8.: Standard experimental setup. The optical bench laser setup (a) consists of a 1064 nm laser with multiple attenuation stages. A 99:1 fiber splitter is used to attenuate the signal, where only the 1 % line is routed to the cryostat (b). Another 50:50 beam splitter can optionally be used when employing two fibers at the same time, or for further attenuation. After the second splitter, the gray fiber represents the *fiber-coupled* option, where the fiber is directly connected to one of the TES chips. The orange fiber represents the *non fiber-coupled* option, where the fiber is e.g. placed on the MXC-stage above instead. Subsequently, the SQUID output is readout by the DAQ system (c), where recorded single-pulses or timelines can be displayed in Volts. The temperatures in the setup drawings are based on measurements. Drawing adapted from Gulden Othman.

fibers with FC/APC connectors enter the cryostat from the top via vacuum feedthroughs. Within the cryostat's 40 K stage, the fibers are spliced to vacuum-compatible Corning HI1060 fiber ends without cladding. These unclad fibers are routed through the remainder of different cryostat stages until reaching below the MXC stage (for setup reference see Fig. 2.1). On each subsequent stage, the fibers are thermalized by attaching them to the heat switches and flanges using aluminum tape, to avoid heat transfer from outside of the cryostat to the sensitive detection system below the MXC plate. The pigtail fiber tips are anti-reflection coated and plugged into the fiber sleeves on the detector as described in Sec. 2.2.2. Since significant heat load from the plugged-in optical fibers was still observed in this configuration in the past, copper heat sinks, visible in Fig. 2.7, were installed before the fiber tip, which enable thermal contact between the fiber tips and cold finger using copper wires. For the final setup, any holes connecting the space within the aluminum can (see Sec. 2.1) to the stages above, are covered with aluminum tape for two reasons: Firstly, to avoid convective heat transfer between the cryostat stages and secondly, as a radiation barrier. The FC/APC fiber ends on the outside of the cryostat are connected to a mating sleeve, connecting the detector to an optical setup. The standard optical setup

involves a Schäfter + Kirchhoff 58 FCM 1064 nm fiber-coupled laser diode as a photon source, which is attenuated by multiple attenuation stages from $\sim 10^{-3}$ W to $\sim 10^{-16}$ W using a combination of e.g. Thorlabs TN1064R1A1A 99/1 beam splitters, a fiber-coupled Schäfter + Kirchhoff 48AT-0 screw attenuator, or additional barrel attenuators from 5 dB to 25 dB. The proper amount of attenuation can be gauged by observing the TES detector output on an oscilloscope while steadily decreasing the attenuation e.g. from a fully closed screw attenuation block, until triggered single pulses are visible on the oscilloscope screen without pile-up. A variation of the standard setup is the **non fiber-coupled** standard setup, where the pigtails are not plugged into the fiber sleeves. For calibration purposes they are not removed completely from the setup. Instead, they are

- either placed on the top of the MXC flange, while peeling back the aluminum tape to allow light from the fiber end to scatter into the aluminum can.
- or the fiber is hanging into the aluminum can from the bottom of the MXC plate.

The non fiber-coupled setups are similar to intrinsic measurement setups described before [17, 18, 58, 66, 68, 91], however, some laser light is generally necessary for calibrating the TES response within the same cool down cycle. Therefore, it is unavoidable to include the option to scatter light into the detection space using the optical fiber.

2.4.2 Calibration Setups

Calibration setups are used for calibration campaigns, either separate from a DM measurement for detector characterization or for pre-measurement pulse shape calibration. Generally, calibration setups can be **fiber-coupled** or **non fiber-coupled**, similar to the standard setup. Figure 2.9 shows the calibration setup in the fiber-coupled configuration. While the setup within the cryostat stays the same, the calibration is performed with different laser systems in the optical setup, using laser diodes of different wavelengths: These

wavelength [nm]	energy [eV]
880	1.409
1064*	1.165*
1310	0.93
1640	0.75

Tab. 2.2.: Energies and wavelengths of different lasers used in the calibration setup. The (*) refers to the previously mentioned 1064 nm laser not operated with the same laser driver.

butterfly diodes (except for the 1064 nm laser) can be used with the same Thorlabs CLD1015 fiber coupled-laser diode driver, where each wavelength uses different wavelength-specific attenuation equipment, such as variable optical attenuators. A list of equipment used for

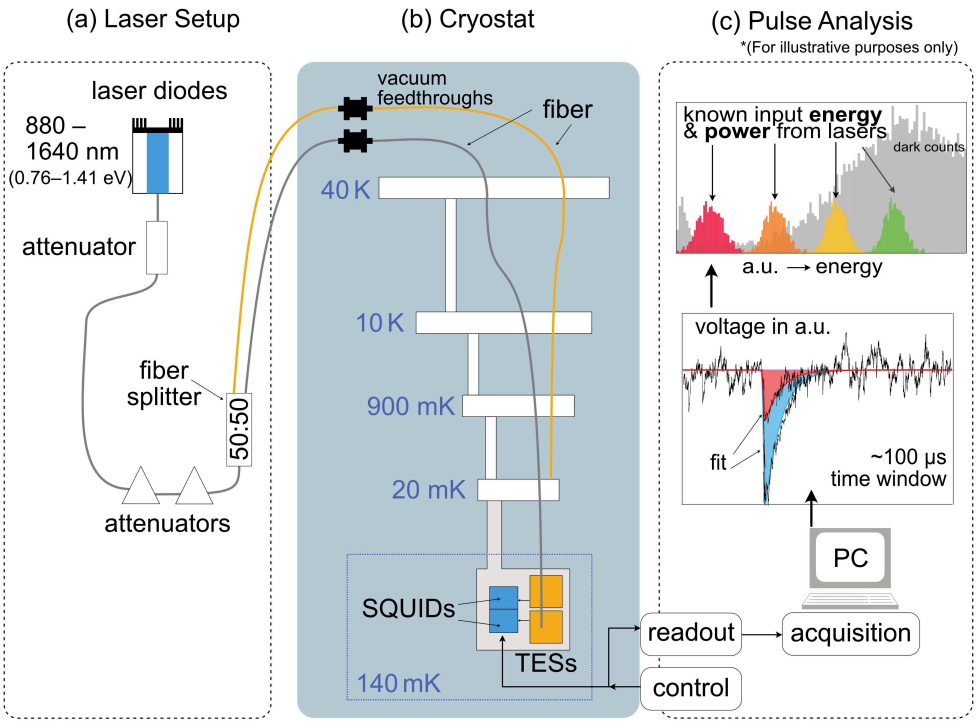

Fig. 2.9.: Calibration setup using laser diodes. The optical bench laser setup (a) consists of a laser driver that can be equipped with laser diodes of different wavelengths. Subsequently, multiple attenuation stages adapted to each wavelength attenuate the signals. Inside the croytsat (b) the gray fiber represents the *fiber-coupled* option, where the fiber is directly connected to one of the TES chips. The orange fiber represents the *non fiber-coupled* option, where the fiber is e.g. placed on the MXC-stage above instead. Either of these options can be used for a DM measurement. Subsequently, the SQUID output is readout by the DAQ system (c), where recorded single-pulses or timelines can be displayed in Volts. After subsequent fitting, pulse shape parameters can be used for energy calibration. Drawing adapted from Gulden Othman.

specific wavelengths within the calibration setups can be found in App. B. Apart from the optical setup outside of the cryostat, the HI1060 fibers[7] within are not substituted for these measurements, due to technical obstacles. However, since the efficiency of the transmission of single photons from the laser, through the fiber, to the detector is not of interest for DM measurements, the fiber losses can be ignored. As such, the losses in the fiber don't influence the pulse shape, but only the amount of pulses reaching the TES. Lastly, it is important to note that an increased laser power is needed in all non fiber-coupled setups, to account for the increased distance between the fiber tip and detector, and scattering losses.

[7]Single-mode fiber optimized for a wavelength of ∼1060 nm and with reduced transmission for other wavelengths.

2.4.3 Dark Matter Setups

For DM setups, shown in Fig. 2.10, nothing changes within the cryostat in comparison to the calibration setup, however, it is always non fiber-coupled. Therefore, the fiber is either

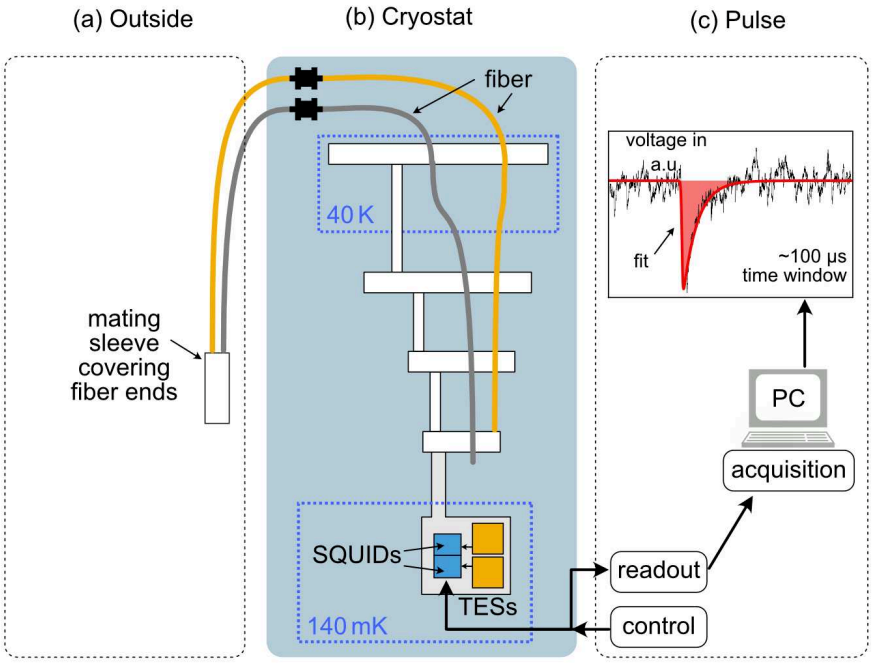

Fig. 2.10.: Setup used for DM search measurements. Outside of the cryostat (a) the fibers are plugged into a mating sleeve with covered fiber ends. Additionally, a black cloth is put on top of the optical bench to avoid stray light coupling into the fiber. Inside the croytsat (b) the gray fiber represents case where the fiber end is hanging above the TES in the same space. The orange fiber represents the option, where the fiber is placed on the MXC-stage above instead. Subsequently, the SQUID output is readout by the DAQ system (c), where recorded single-pulses or timelines can be displayed in Volts. Drawing adapted from Gulden Othman.

placed on top of the MXC stage or directly below. Outside of the cryostat, the optical fiber is not connected to a light source but is plugged into a mating sleeve, which is covered by a dark cap. To further avoid stray light coupling into the fiber, the optical table is covered by a black cloth as well.

3 Detector Optimization and Calibration

To investigate the detectors' sensitivities to different DM masses, the goal is to determine an energy spectrum of possible DM signals from a long measurement ($> 100\,\mathrm{h}$). Therefore, it is important to choose advantageous measurement configurations for a large dynamic range and good energy resolution. Furthermore, the understanding of the detector's response to depositions of different energies and of possible backgrounds present in recorded data is crucial. Combined, this information will enable a cut-based event selection used on pulse shape parameters derived from a fitting analysis. Before starting direct DM search measurements the TES and SQUID working point configurations of each detection module are optimized accordingly and calibration measurements, using lasers of different wavelengths and therefore energies, are performed.

The used experimental setups follow the description from Section 2.4. The following chapter outlines the general optimization and calibration of the used detection module for DM measurements. Since this procedure relies on the analysis and comparison of various parameters derived from the pulse shape of single-photon samples, first, the general signal shape and the fitting procedure are demonstrated in Section 3.1. Next, the preparatory procedures performed for each detection module are discussed. First in Section 3.2 for the detector optimization, using TES F as an example, and secondly in Section 3.3 for the calibration procedure, using TES D. Lastly, possible backgrounds contributing to these measurements, also influencing the Signal-to-Noise Ratio (SNR), are considered in Section 3.4. This includes the discussion of consecutive simulations of the baseline electronic noise background.

3.1 TES Signals and Fitting

The fit function and parameters described in the following, outline the general fitting analysis used for the majority of this thesis. If not stated otherwise, results derived from fit parameters refer to the fitting in frequency domain using the FFT fit approach of the ROOT-based *TESPASS* framework introduced in Ref. [58].
As described in Sec. 1.3, the SST can be used to describe the shape of single-photon pulses

in the TES sensors. As outlined in detail in Ref. [58], Eq. 1.29 can be converted to the frequency domain, which renders a fitting of the otherwise unstable SST function possible:

$$\mathscr{F}\left[U_{\mathrm{SST}}(t)\right](f) = -A_{\mathrm{SST}}(\tau_- - \tau_+)\frac{(1-(2\pi f)^2\tau_+\tau_-) - i2\pi f(\tau_+ + \tau_-)}{(1+\tau_+^2(2\pi f)^2)(1+\tau_-^2(2\pi f)^2)}e^{-i2\pi f t_0} \tag{3.1}$$

The pulse, converted to the frequency domain, is fitted there, using the above function, as shown in Fig. 3.1(a) and (b). The resulting fit parameters A_{SST}, τ_-, τ_+ and t_0 can be plugged into Eq. 1.29 to display the fitting function in the time domain, shown in Fig. 3.1(c). Figure 3.1(d) also shows the Power Spectral Density (PSD)'s square root determined from the noise of the underlying dataset. Other parameters of interest, which can be derived

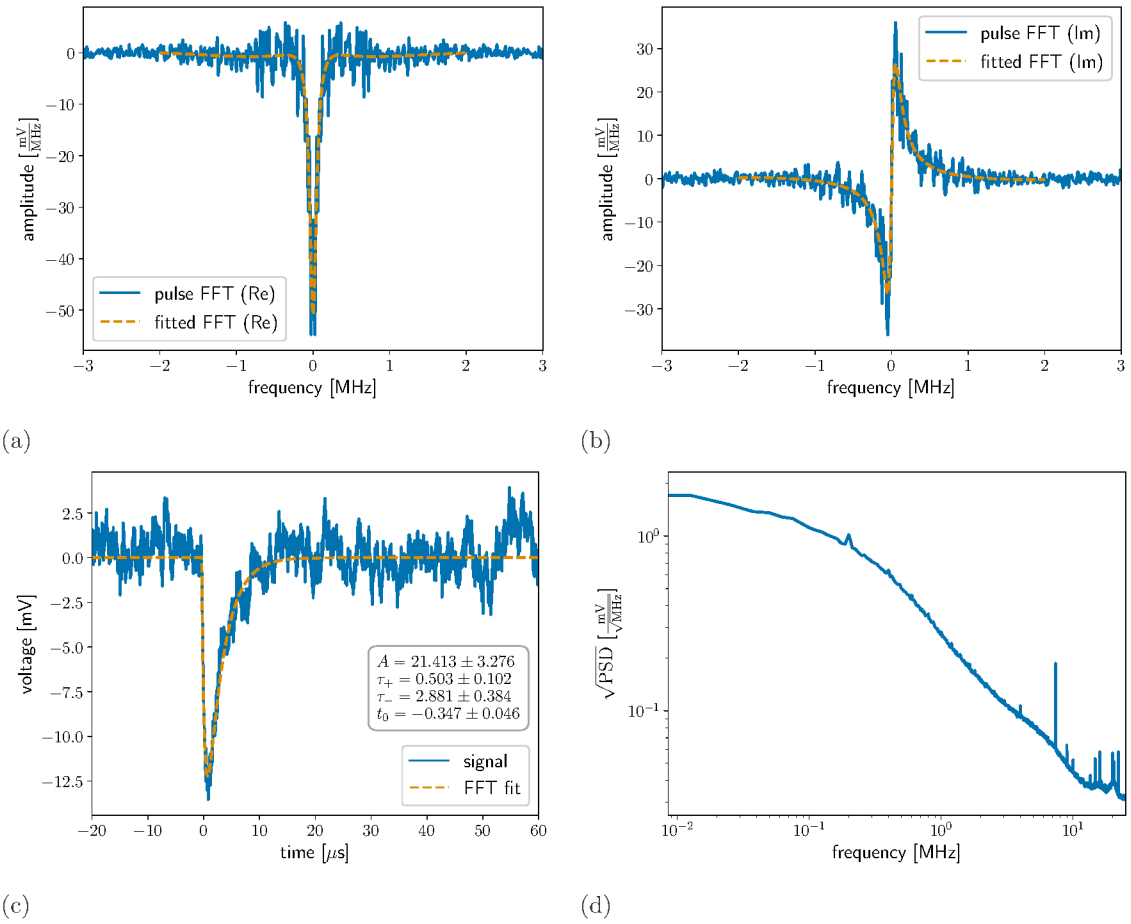

Fig. 3.1.: Example 1064 nm pulse recorded with TES D (working point 0.2 R_N and 5.0 GHz GBWP): (a) Real part and (b) imaginary part of the signal in frequency domain including respective FFT fits. (c) FFT fit in time domain representation, including fit parameters and (d) square root of the PSD based on the corresponding noise of the dataset.

from the fit parameters are the pulse height[1] and pulse integral. Furthermore, the general

[1]Note that the amplitude of the fit function is a scaling parameter and is defined differently from the pulse height, which describes its minimum.

fitting analysis uses functionalities of the *TESPASS* framework such as the pulse finding algorithm, which helps to identify photon-like pulses and can remove noise or double-peaks from the triggered timelines before the actual fitting [58]. The pulse finder needs to be tuned to known signals using a model rise and decay time, e.g. based on a 1064 nm sample. In addition, different combinations of a low pass filter and threshold level for the deconvolved timelines are compared to find the pulse finder configuration optimizing the number of identified signal pulses compared to the number of wrongly identified pulses from noise. The amplitude and starting time of a signal pulse determined by the pulse finder is then used as a fixed parameter for the fitting function. The pulse finder is only employed for the main DM analysis in Ch. 4 once the measurement configurations are set. Therefore, in Sec. 3.2 and Sec. 3.3, the general analysis is performed without the pulse finder.

3.2 Detector Optimization

As discussed in Sec. 1.3.5, the assets of TES sensors over other detection methods, like low energy threshold and energy resolution, need to be exploited properly to probe for advantages over e.g. SNSPDs. The goal of this optimization is to find the configuration with the best dynamic range and comparably low baseline noise, leading to high SNR and good energy resolution. This will ensure to set the lowest possible trigger threshold, directly resulting in increased sensitivity for lower energies in the DM measurements. This increases its sensitivity, especially to lower mass DM.
Therefore, optimizing the settings of each module for these low-energy searches is of great importance. In the first step, this optimization refers to finding the proper SQUID settings for the most stable locks in FLL mode. In a second step, this regards the selection of bias current, which translates to a working point on the temperature-resistance curve, in terms of the normal resistance R_N, of Fig. 1.4. Before each measurement, the bias curve is measured[2] and the bias current at different working points is determined from the resistance-current curve. An example from TES F is shown in Fig. 3.2.
Merely the choice of e.g. the working point already greatly influences the SNR and energy resolution [17]. Choosing working points in less linear regions of the resistance-current curve, especially towards the higher working points, leads to a less linear TES response. Close to the normal resistance, the dynamic range for larger energies degrades, since the TES already saturates at comparably low energy depositions. The choice of GBWP also greatly influences the pulse shape, where higher values lead to faster and larger signals, and lower values to smaller and slower ones. The values listed in Tab. 3.1 are investigated to scan a large range of possible configurations, including those GBWPs which provided reliable results in the past. Next, these bias currents are applied to the TES circuit. For each working point, short measurements of light samples are conducted in combination with

[2]This procedure has been previously described in detail in Ref. [17] and [18].

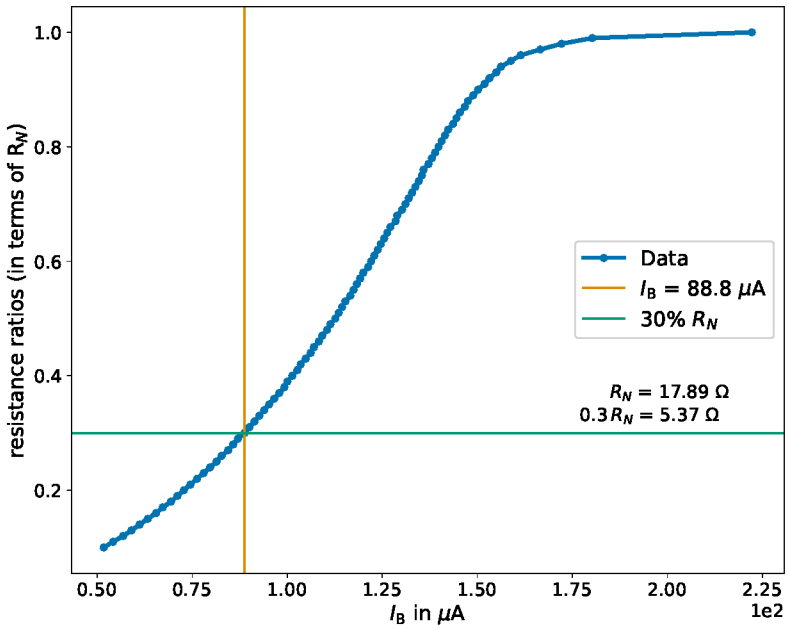

Fig. 3.2.: Measured bias current I_{bias} of TES F in comparison to the working point in terms of the normal resistance R_N. The horizontal and vertical lines represent a possible resistance working point at 30 % R_N and its associated bias current respectively.

Working Points [R_N]	**GBWP [GHz]**
0.2	2.8
0.3	5.0
0.4	6.2
0.5	7.2

Tab. 3.1.: Summary of all working points and GBWPs tested. All combinations across these values are explored independently.

different SQUID GBWPs. The light samples, in this case, are 1064 nm photons from the attenuated S&K laser using the standard setup described in Sec. 2.4.1. It is important to note, that for the DM configuration, the fibers were not plugged into the TES module's fiber sleeves (non fiber-coupled configuration) but are placed above the last cryostat stage on the MXC flange. The same thing applied to the optimization here, as coupling the fiber to the module increases the heat load and influences the detector response. When attenuating the laser less, compared to the attenuation needed for direct fiber connection, the light shining from the fiber tips can reach the TES chips inside of the aluminum can through a small slit that is usually used for routing the fibers from the MXC stage to the TES module. For each working point and GBWP a corresponding trigger value is selected to always trigger at approximately half of the pulse height and avoid triggering on baseline electronic noise. For each configuration, approximately $\sim$ 1000 pulses are recorded to retrieve comparable statistics.

Subsequently, the resulting pulses for each GBWP and working point combination are fitted and the configurations' performances are compared. This includes additional figures of merit such as the average pulse shape or noise PSD, however, as motivated above, in this description the focus lies on the resulting energy resolution and SNR. Since these figures of merit are derived from the determined pulse shape parameters, these are compared for stability within each working point for different GBWPs first. The following sections regards optimization results concerning TES F. Appendix C gives a short discussion for the optimization of TES D.

3.2.1 Pulse Shape Parameters

Differences between the signal shapes can be used to compare the performance of different TES and SQUID configurations, especially since the event selection relies on the pulse shape. A preferable working point should show stability over multiple GBWPs, such that the choice of GBWP does not drastically influence the resulting measurement. It was shown, that higher GBWPs lead to more a narrower fit parameter distribution e.g. for the rise and decay time [58]. This can simplify a cut-based analysis, hence higher GBWPs are preferable from that viewpoint. However, higher GBWPs can also increase noise harmonics and create spikes in the pulse timelines, able to influence the trigger rate in such setups. Therefore, this must be considered as a trade-off.
The fitting parameters for the different working points and GBWPs are compared roughly by using the median of each parameter distribution for each configuration. The resulting comparisons are displayed in Fig. 3.3 for TES F. The uncertainties are derived from the lower and upper 68 % percentile normalized by the square root of the number of events.
In general, the lower working points show more stability for different GBWPs, while there can be larger deviations e.g. for the rise and decay times for higher working points. Especially the lowest GBWP of 2.8 GHz leads to much smaller and slower pulses. The differences between the higher GBWPs are minimal at lower working points.

3.2.2 Energy Resolution

Good energy resolution is important for background discrimination in single-wavelength searches such as those needed in ALPS II, since it helps to identify and reject pulses of lower or higher energies. Also for DM searches, the ability to create energy resolved spectra in contrast to counting experiments, such as SNSPDs, can represent an advantage for setting limits on different DM parameter spaces. Consequently, we are interested in the full spectrum of energies of surviving photon-like pulses, for which the energy resolution is an important parameter that defines the accuracy of our resulting background or DM spectrum.

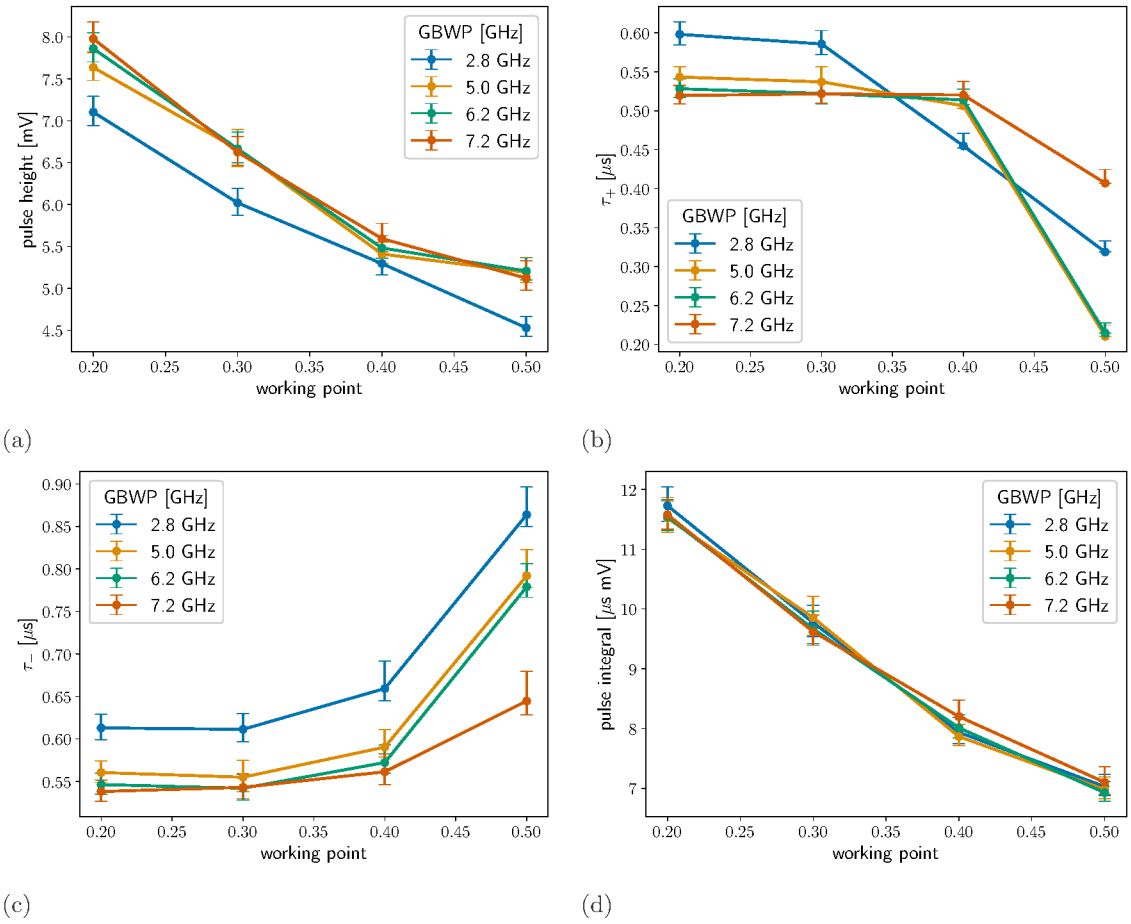

Fig. 3.3.: Pulse shape parameters for different working points and GBWP configurations (see Tab. 3.1) of TES F, namely (a) Pulse height (b) rise time τ_+ (c) decay time τ_- and (d) pulse integral.

Following Ref. [58], the energy resolution is determined using the pulse height derived from the fitting function. From the distributions of fit results for the pulse height and pulse integral the energy resolution is determined by fitting a Gaussian function and dividing the standard deviation by the mean:

$$\frac{\sigma}{\mu} = \frac{\sigma_E}{E} \tag{3.2}$$

which is equivalent to dividing the standard deviation σ_E by the measured energy E. The resulting energy resolutions are shown in Fig. 3.4. For previously used modules, such as TES A[3] (see App. A), an energy resolution as low as $(5.12 \pm 0.06)\,\%$ has been determined [58]. However, the energy resolution here is most likely influenced by the non fiber-coupled setup. The energy resolution of TES A was determined for a fiber-coupled setup, where the photons exiting the fiber are aligned directly onto the TES chip. In the non fiber-coupled

[3]Measured with a GBWP of 1.5 GHz and a working point of 30 % R_N.

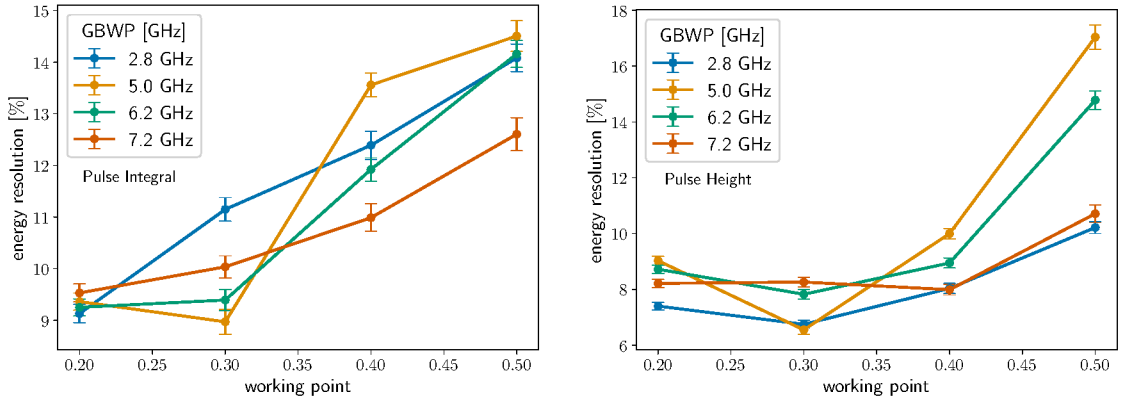

(a) (b)

Fig. 3.4.: Energy resolution for different working points and GBWP configurations (see Tab. 3.1) of TES F, determined using (a) the pulse integral and (b) the pulse height parameters. The uncertainties originate from Gaussian error propagation based on the fitting uncertainties of the Gaussian functions.

setup the photons can scatter from the cryostat's shields, coldfinger, and other components which can reduce the precision of these measurements compared to fiber-coupled setups, due to angled impact on the sensor or energy loss before reaching the sensitive area.

For TES F, the energy resolution declines towards higher working points. Since it was also shown that the energy resolution is primarily dependent on the baseline electronic noise [58], this confirms higher noise levels at higher working points. In general, the pulse height parameter yields improved energy resolution compared to the pulse integral parameter, as previously shown in Ref. [58]. The best energy resolution determined using the pulse height is mostly independent of the GBWP, but concentrates towards lower working points e.g. $0.2R_N$ and $0.3R_N$. The best overall energy resolution of $(6.551 \pm 0.002)\,\%$ is achieved with $0.3R_N$ and 5.0 GHz.

3.2.3 Signal-to-Noise Ratio

The larger the ratio between the signal height and the noise baseline, the lower the trigger threshold in a dedicated DM search measurement can be set, which increases the sensitivity for lower energy depositions, extending the sensitivity to lower DM masses. Therefore, the SNR, influenced by the GBWP and working point of a detector module as well, is another important parameter to consider. Fig. 3.5 shows the SNR of module F for different GBWP values. The uncertainties, mainly arising from the standard deviation of the signal height, are quite large due to the SNR being computed from the average pulse of each raw data set.

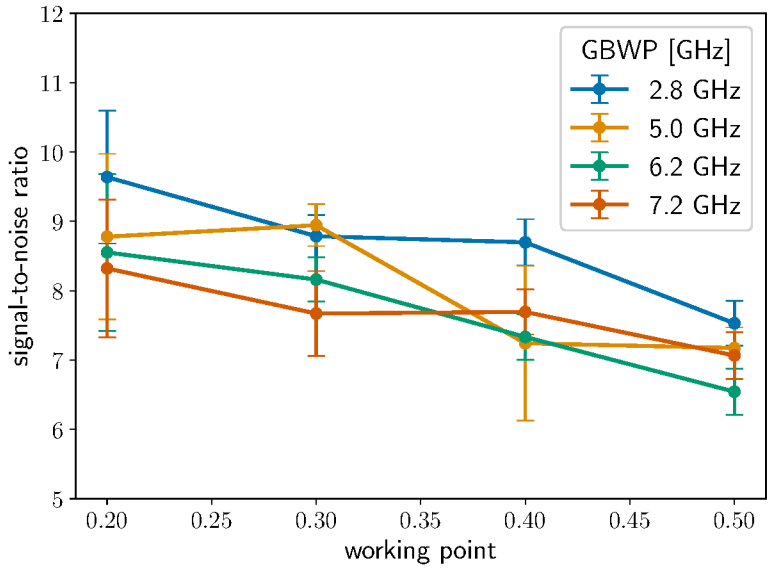

Fig. 3.5.: SNR for different working points and GBWP configurations (see Tab. 3.1) of TES F. The uncertainties originate from Gaussian error propagation.

Therefore, possible outliers and other backgrounds are not filtered here. Overall, the SNR degrades with higher working points, while it increases for lower ones. This is most likely a result of a higher relative noise level, as previously indicated by the poor energy resolution for higher working points.

Overall, there are advantages and trade-offs to each configuration, as no single one of the GBWP-working point combinations stands out significantly in all categories. One can conclude, that lower working points such as $0.2R_N$ and $0.3R_N$ yield preferable performance, and the differences for varying GBWPs are often marginal, but tend to improve for mid-tier GBWPs. In this case, the configuration $0.3R_N$ and 5.0 GHz was chosen. The used configurations for both TES modules D and F for the remainder of this work are listed in Tab. 3.2. It is important to note that the performance of TES D and F is quite different.

	working point in terms of R_N	GBWP [GHz]
TES D	0.2	5.0
TES F	0.3	5.0

Tab. 3.2.: Optimized working point and GBWP configurations chosen for DM searches with modules TES D and TES F.

Especially when comparing the rise and decay time parameters of TES F in Fig. 3.3 and TES D in Fig. C.3, it is evident that the pulses are much faster in TES F, also resulting in a lower pulse integral and pulse height. The energy resolution however is overall comparable (see Fig. 3.4 and Fig. C.4), while the SNR is slightly better for TES D (see Fig. 3.5 and

Fig. C.5). These differences can not be pinpointed directly, but could be a direct result of the difference in the two setups. Especially the difference in material surrounding the TES chips (copper cylinder vs. sapphire rod and zirconium sleeve) resulting in differences in the heat load. Fast signals could e.g. also be a consequence of a higher current sensitivity.

3.3 Energy Response Evaluation

To determine an energy-resolved DM spectrum from a dedicated measurement, it is imperative to understand the detector's response to different energy depositions. This facilitates the application and choice of cuts on fitting parameters for subsequent event selection. For energies around 1 eV we expect a linear response for parameters proportional to signal height [57, 58]. Since other parameters, such as the rise and decay time, are mainly governed by the TES circuit [57], these should remain more or less constant for a wide range of energies. The linearity of the energy response was previously shown for a similar detector in Ref. [64] for energies from 1 eV to 3 eV and simulations of the detector response based on small signal theory predict linearity of both pulse integral and pulse height for lower energies as well [58]. However, the same simulation also shows nonlinearity of the pulse height response for higher energies, since the corresponding heating of the detector reaches non-linear regions of the temperature-resistance curve. On the other hand, the more complex pulse integral response remains linear to a certain extent, including not only voltage but also time information. Therefore, since the pulse integral is expected to be mostly linear in our region of interest, it is well suited for calibration purposes to calculate a DM energy spectrum.
Thus, to conduct dedicated DM search experiments, the following main assumptions must be tested, regarding the detectors' responses to a range of energies:

- linearity of pulse integral response
- stable response of rise and decay time

For this purpose, the light of four different continuous wave diode lasers (introduced in Sec. 2.4.2) is used to gauge the response of the detectors to different energy depositions.

This calibration measurement uses the SQUID and TES settings determined with the optimization procedure listed in Tab. 3.1. As the detector response shifts in different cooling cycles, the focus here is the general behavior of pulse shapes for different energies and not absolute values.
As previously mentioned, the lasers' energies range from 0.756 eV to 1.409 eV (see Tab. 2.2). Exploring the detector response at lower energies is limited by the current experimental setup. Simulations of black body background coupling into the fiber on the warm outside of the cryostat, show a cutoff in transmission for energies below 0.7 eV [72]. The fiber routing

inside the cryostat includes the curling and winding of optical fibers, which can cut off the transmission of higher wavelengths depending on the curling radius and amount of curls. It is therefore not possible to measure photons from lasers of higher wavelengths with the current setup. This has no influence on the detector's actual energy response.

For the calibration, photon pulses from each laser diode were recorded separately, including the installation of each butterfly diode in the laser driver independently, and also changing the settings and configuration of the laser driver for each diode and adjusting the optical setup to attenuate the lasers sufficiently before the fibers enter the cryostat. This also necessitates the use of wavelength-appropriate attenuation equipment. Details regarding this setup are listed in App. B.
Using the non fiber-coupled version of the calibration setup (see. Sec. 2.4.2), the TES D module is used here as an example. Results for TES F can be found in App. D.

When comparing the averaged signals for the different wavelengths in Fig. 3.6, the change in pulse height can already be observed for distinct wavelengths. For lower wavelengths

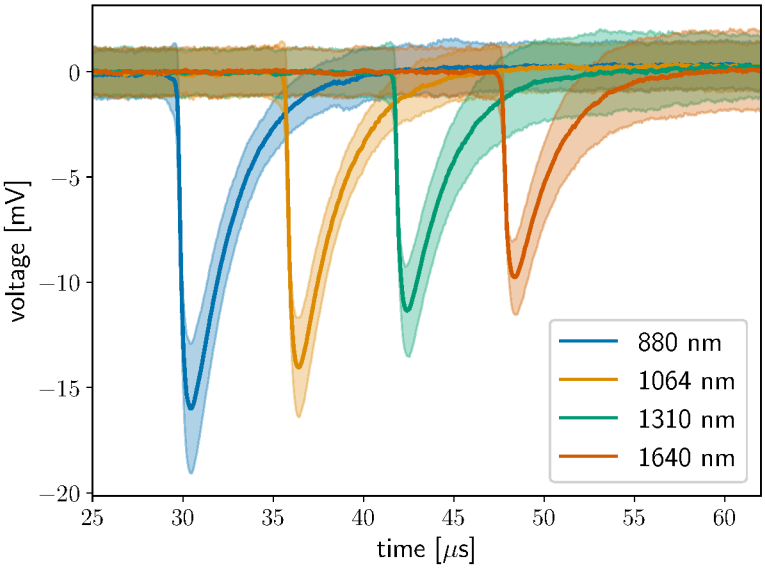

Fig. 3.6.: Average pulses for different wavelengths, measured with the TES D module during calibration, including standard deviations. Measurement performed in the non fiber-coupled calibration setup. The average pulses are arbitrarily shifted in time for simplified comparison.

(higher energies), the pulse height increases, while it decreases for higher wavelengths (lower energies). Similar to the optimization procedure, each pulse of each unique wavelength dataset is fitted and the resulting fit parameters for the different wavelengths are compared, see the histograms in Fig. 3.7. Outliers from possible background triggers have been cut from each distribution. As expected, parameters proportional to the signal's height like the amplitude or pulse integral exhibit an energy-dependent behavior, where higher energies lead to higher values. Fig. 3.8(a) showcases that the most probable values originating from

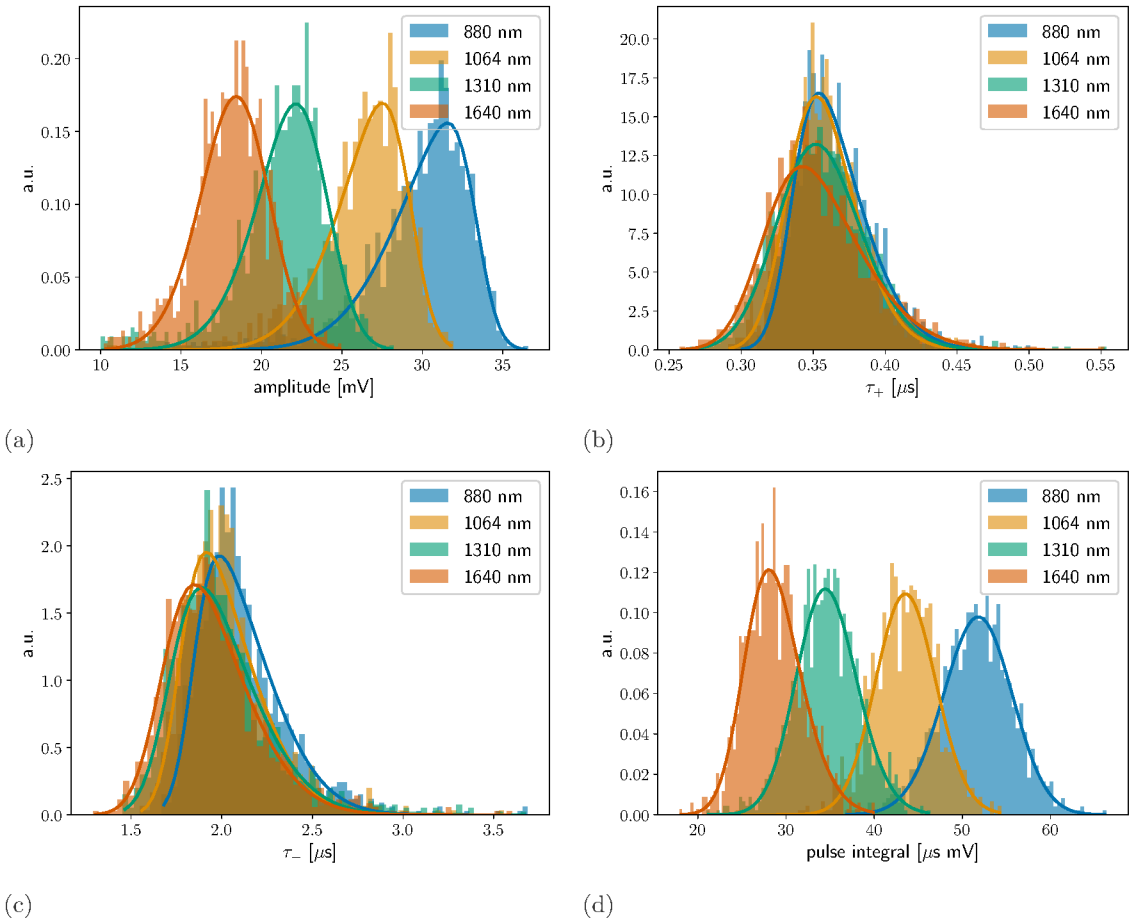

Fig. 3.7.: Fitting parameters for photon pulses of different wavelengths measured with the TES D module during calibration (non fiber-coupled calibration setup). Namely the normalized distributions of the (a) pulse amplitude (b) rise time τ_+ (c) decay time τ_- and (d) pulse integral fitted with a skewed Gaussian function ($G_{\text{skew}}(x, A, \mu, \sigma, \alpha) = 2A \cdot G(x, A, \mu, \sigma)\,\text{erf}(\alpha, x, \mu, \sigma)$ with a Gaussian function G and error function erf.)

the pulse integral and amplitude distributions in Fig. 3.7(d) follow a linear path[4]. The fit parameters of the respective linear fits are listed in Tab. 3.3. For the fitting parameters τ_+

	m	b
amplitude	$(20.4 \pm 0.2)\,\frac{\text{mV}}{\text{eV}}$	$(3.2 \pm 0.2)\,\text{mV}$
pulse integral	$(36.3 \pm 0.3)\,\frac{\text{µs mV}}{\text{eV}}$	$(0.9 \pm 0.3)\,\text{µs mV}$

Tab. 3.3.: Fit parameters based on TES D of the linear fit to the amplitude and pulse integral depending on the laser energy for the linear fit function: $y = mE + b$.

and τ_- describing the rise and decay time of the signals, a clustering around similar values

[4]The pulse integral is derived from an integration over the fitting function in time, yielding a proportionality to the amplitude.

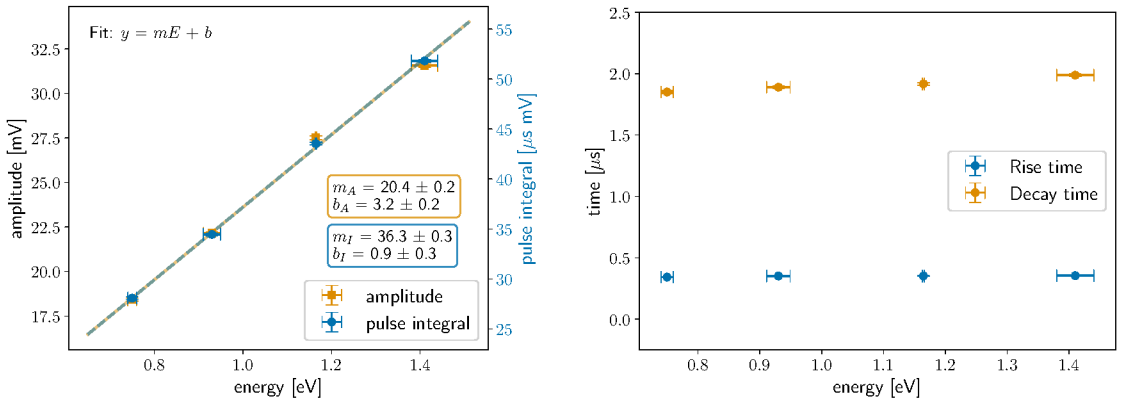

(a) (b)

Fig. 3.8.: Most probable values of fitting parameters for photon pulses of different energies (wavelengths) measured with the TES D module during calibration (non fiber-coupled calibration setup) for (a) pulse integral and amplitude, and (b) rise and decay time parameters τ_+ and τ_-. The uncertainties of the parameters are not visible at this scale and the uncertainties of the energy results from the spectral spread of the used laser diode.

can be observed in Fig. 3.7 (b) and (c), as the distributions tend to be much less separated from each other. The most probable values of these parameters depicted in Fig. 3.8(b), show a mostly constant response of these parameters to photon pulses of different energies, which identifies both as suitable parameters for the isolation of photon-like signals. For non-photon like signals or energy depositions in the Si substrate surrounding the TES (as opposed to depositions in the active W layer) the rise and decay time would differ (more details in Sec. 3.4).

In conclusion, the calibration measurements have shown the energy dependence of the TES response, where especially for the pulse integral (and amplitude) a linear proportionality to the deposited energy can be derived. Simultaneously, the rise and decay time stay mostly constant over the probed energy range. This was confirmed for both modules TES D and F, even though the parameter values differ significantly, due to the faster pulses in TES F. This information is used in Ch. 4 for calibrating and isolating photon-like signals in dedicated DM measurements, where the TES response is assumed to remain stable for lower energies as well.

3.4 Backgrounds

In most particle DM search experiments, extremely low background is imperative. Furthermore, it is crucial to understand the backgrounds and limitations of the used detection system. As has been described for many low-background experiments, understanding low-energy backgrounds is non-trivial. One of the best examples and most coordinated

efforts towards this understanding is probably the Low Energy Excess (LEE) initiative [92], aiming to map and understand excess signals arising at low energies close to the detector thresholds for example in cryogenic (e.g. Ref. [93]) or CCD (charge-coupled device) detection setups [94] searching for DM or neutrinos. These excesses generally arise below 100 eV and close to the detection threshold of each device independent of its energy scale. Such LEE events have been observed in other experiments using TES chips, as well [95, 96]. While the source of these LEEs remains unknown, possible explanations include signals originating from so-called quasiparticle poisoning. Phonons originating from mechanical stress with origins ranging from metal films adjacent to the detector to glue, could potentially break Cooper pairs in the TES chip and imitate photon signals [97, 98]. However, it is unlikely that this excess is due to a single process, since the spectral shapes from different experiments are not compatible with each other.

Due to the region of interest around 1.165 eV, which is way above the noise level of the used TES chips, these LEE backgrounds have not posed an obstacle in the detector development for the ALPS II experiment. By reducing the trigger threshold of the DAQ system closer to the noise level of the detection modules, LEE effects could arise in long-term measurements. For TES D, a trigger level of −9 mV adequately results in a dataset with only a small number of triggered pulses. In contrast, the trigger level chosen for the DM search is reduced to −5.6 mV, resulting in a higher number of triggered pulses.

On the other hand, the thorough research and effort towards reducing the intrinsic background of the TES detection module for the ALPS II experiment, provides in-depth studies and conclusions for known backgrounds in our system, including baseline electronic noise at the DAQ output, charged cosmic rays and ambient radioactivity [58, 66, 68, 72]. This subsection gives a short summary of these known backgrounds and also discusses the role of baseline electronic noise at the DAQ output, called electronic noise for short, in measurements with a low trigger threshold[5], which was mainly investigated with and for the TES D module.

3.4.1 Known TES Backgrounds

As already discussed in Sec. 1.3.1, the original purpose of the previously used TES detectors is their implementation into the ALPS II experiment. Therefore, they were optimized for a photon-wavelength of 1064 nm. For photons of this wavelength, the detection system must be more sensitive than the expected rate of photons reconverted from photon-axion oscillations in ALPS II at its target sensitivity: $\sim 10^{-5}$ cps [99]. Dedicated studies and analysis methods have been developed towards the detectors' viability for ALPS II of previously used modules (see App. A: modules A and B). These have been able to push the

[5] "Low" and "high" triggers generally refers to the absolute value of the trigger level within this work.

dominating extrinsic[6] background for 1064 nm photons, mainly arising from black body radiation entering the fiber from the warm outside of the cryostat, down to $\sim 10^{-4}$ cps. This was first mentioned in Sec. 3.3 and is further discussed in Ref. [72]. Similarly, previous studies have also investigated contributions of the intrinsic[7] background without fiber-coupling, equivalent to the detection mode for DM measurements. In ALPS II's energy range, intrinsic studies already yield sufficiently low rates of $6.9 \cdot 10^{-6}$ cps [67]. Hence, further reducing the black body radiation background presents one of the key goals to prepare TES detectors for use in the ALPS II experiment, with multiple experimental and analytical efforts targeting this obstacle [72, 100].

No optical fiber is coupled to the detector for DM search measurements, but placed with considerable distance on a cooling stage above the detection stage (see Sec. 2.4.3)[8]. Therefore, an in-depth discussion concerning extrinsic black body photon contamination is skipped here. Instead, intrinsic background sources are discussed in more detail: The majority of intrinsic background sources are energy depositions in the Si substrate the TES chip is placed on. Sources of these depositions include charged cosmic rays and radioactive decays close to the detector. As described in Ref. [17], many of these backgrounds can be filtered out easily by applying dedicated cuts, since the pulse shape differs from that of a photon. Fig.3.9 shows examples of these background signals found in a calibration sample and a 1640 nm reference photon pulse. The low-energy photons (such as 0.756 eV in the example) are directly absorbed by the TES chip leading to faster signals defined by a sharp rise and slightly slower decay time of the resulting pulse. Higher energetic cosmic rays or radioactive decays depositing energy in the Si substrate can induce signals in the TES chip as well, since their phonon systems are coupled. However, signals originating from the Si substrate recorded with the TES chip are significantly slower as they have to propagate through the substrate first, resulting in significantly slower rise and decay times. These are called *slow* signals [58] and do not originate from energy depositions within the W substrate of the TES. Their pulse shape is influenced by the deposited energy in the substrate and the distance TES. Furthermore, these higher energetic background sources often deposit such high energies within the substrate in close vicinity to the TES, that the TES is driven to its normal conducting region, therefore leading to even longer decay times to return the chip to its working point—so-called *saturation* pulses.
While most of these backgrounds can be isolated by using suitable analysis methods and event selection, they still increase the amount of data and especially trigger rate recorded in dedicated DM measurements. As mentioned in Sec. 2.2.4, the zirconia fiber sleeves

[6] *Extrinsic* background sources are backgrounds introduced by coupling the optical fiber directly with the TES chip and therefore introduced from outside of the cryostat.
[7] *Intrinsic* background sources are backgrounds prevalent intrinsically in the detection system e.g. ambient radioactivity.
[8] For the ALPS II region of interest, Ref. [18] quantitatively showed for a different setup that placing the fiber inside the cryostat but not coupled to the detector, did not increase photon-like intrinsic background levels.

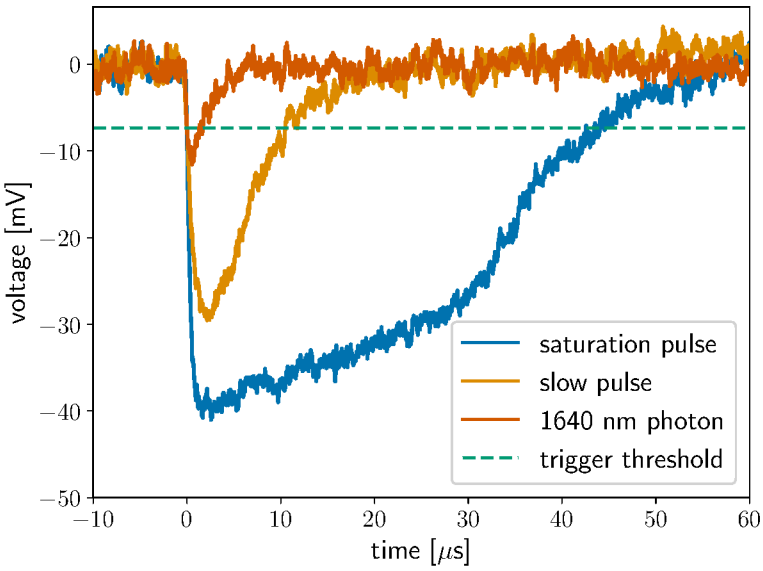

Fig. 3.9.: Different pulses measured during a non fiber-coupled calibration measurement of TES D using the 1640 nm diode. The smallest and fastest pulse is a calibration photon from the laser, while two larger pulses (slow and saturation) were triggered as well.

have been proposed as a leading background contributor[9] using dedicated simulation tools. Therefore, the module adjusted for DM searches, TES F, omitted fiber sleeves entirely. An in-depth discussion on intrinsic backgrounds and their simulation is found in Ref. [58]. The same reference also introduced the pulse finding algorithm used for the analysis of DM search data, which was mentioned in Sec. 3.1 already and aids in background reduction.

3.4.2 Electronic Noise

Due to the significantly lower DAQ trigger level needed to improve the sensitivity of the detector to lower energies, triggered electronic noise fluctuations, including sharp spikes, represent the largest contributor to the data rate recorded in dedicated DM measurements with the detectors. These noise spikes result from current noise at the TES output measured with the SQUID current sensor and readout electronics. In the following, it will be referred to as electronic noise. An example is shown in Fig. 3.10, together with a recorded 1640 nm photon pulse for comparison. These electronic noise spikes are occasional sharp oscillations above and below the noise baseline intrinsic to the recorded timelines, happening with or without additional signals. Even if the mean noise level and its standard deviation remain above the absolute value of the (negative) DM trigger thresholds over long periods, single spikes in the noise timeline can surpass the trigger level and are therefore (in the current DAQ system) saved to disk. When observing such electronic noise spikes in background data, these often only include one to three traces of the saved timeline recorded with a sampling

[9] In dedicated intrinsic background studies for 1064 nm wavelength.

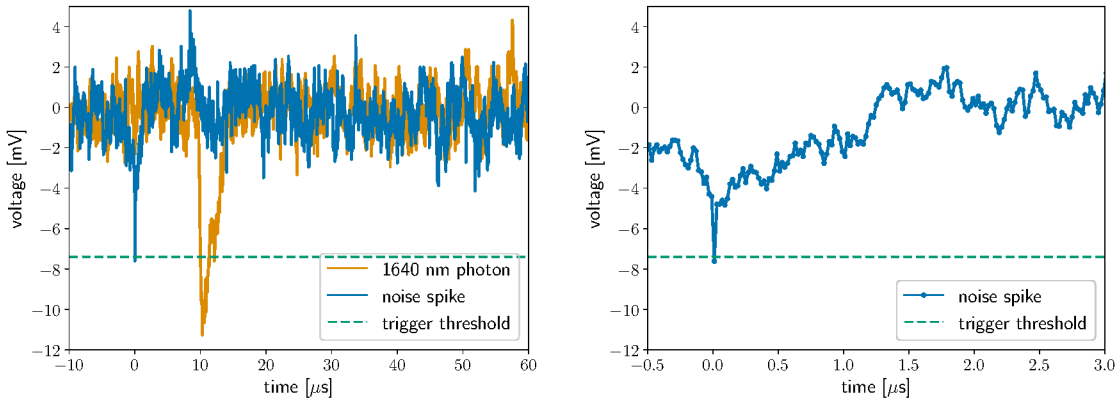

Fig. 3.10.: Example of a triggered electronic noise spike, recorded during a calibration measurement with TES D, (a) together with the shifted signature of a 1640 nm photon pulse and (b) closeup showing the saved time traces of the noise spike. The spiked pulse does not pass the pulse finder of the main analysis in Ch. 4.

rate of 50 MHz. On a recorded timeline of $\sim 80\,\mu$s, these fluctuations happen on the order of less than 100 ns. Based on small signal theory and confirmed by calibration results, the decay time of a pulse induced by a small energy deposition, such as from a DM interaction, should be significantly slower than the rise time. Furthermore, previously measured decay times with TES D were on the order of $\sim 1\,\mu$s, as shown in Fig. 3.8. Therefore, these spikes cannot originate from energy depositions in the TES chip. This electronic noise has been observed in other TES setups with low trigger thresholds and ascribed to electromagnetic interference with the DAQ system [101]. In addition to the custom shields mentioned in Sec. 2.1, the used cryostat is also equipped with an additional Mu-metal shield deployed to reduce electromagnetic interference from other sources[10]. This regards the sensitive SQUID chips, especially. The observed spikes represent the remaining interference, most likely originating from the SQUIDs—Ref. [101] also observed similar noise fluctuations when the TES was set to its superconducting state, confirming the independence of this noise from energy depositions in the TES.

Since these spikes increase the trigger rate significantly, this potentially leads to dead time, as signals begin arriving faster than the system can process them at trigger rates above > 5 Hz, even when using up to seven processors. Hence, the trigger level needs to be chosen carefully to avoid overwhelming the DAQ system, but at the same time be as low as possible to trigger low-energy pulses with smaller pulse height. When analyzing one of the DM measurements conducted with TES D (discussed in more detail in Sec. 4.1), it could be confirmed, that the majority of the 277,691 pulses triggered within 66 h of undisturbed data taking, originates from such spikes. This was investigated by identifying the lowest point of each triggered timeline and counting the number of recorded traces below the trigger

[10]Furthermore, devices in the lab using Wi-Fi, Bluetooth or other forms of electromagnetic communication are turned off or set to airplane mode during data acquisition and no one enters the lab.

threshold. For pulses induced by actual energy depositions in the detector, the number of recorded traces below the trigger should be significantly higher than that of electronic noise spikes. Indeed, the resulting amount of triggers with only a single trace below the threshold, already makes up $> 87\,\%$ of which a large number can be attributed to electronic noise. Using *TESPASS* simulations of triggered timelines including photon-like low-energy signals, the pulse finder can in theory distinguish signals down to at least 0.2 eV from electronic noise [58]. Indeed, the spiked pulse in Fig. 3.10 does not pass the pulse finding algorithm tuned for the DM analysis in Ch. 4. Employed before the fitting procedure in the analysis, the pulse finder can therefore facilitate the identification of the majority of non photon-like signals, including electronic noise, and speed up analysis of large datasets significantly. Dedicated simulations have been performed to confirm this behavior for low trigger thresholds and exclude noise from influencing resulting DM spectra. This includes not only the pulse finding algorithm, but also subsequent event selection cuts based on calibration findings.

Electronic Noise Simulations

As a first test to gauge the suitability of ALPS II's TES detection system for low energy DM searches, the electronic noise baseline was simulated based on the PSD of the previously used TES A module[11] (see App. A) using the *TESPASS* simulation framework. This first short electronic noise simulation had the goal to identify the possibility of beating the energy threshold of 0.73 eV of a competitive SNSPD device [55]. A short noise baseline simulation (500 s at -12 mV trigger level) led to an initial trigger rate of 0.32 Hz. Appropriate triggers and cuts on fit parameters for low-energy photon-like signals were identified using simulated pulses of 0.583 eV. Conclusively, no electronic noise background pulses survived this selection and demonstrates the possibility of lowering the device's trigger threshold without misidentifying electronic noise as signals. Since this preliminary simulation is based on a different module, which is also equipped with different (two-stage) SQUID chips, the simulation, considered in Ref. [102], is not further discussed here. For TES D on the other hand, a significantly longer simulation of the noise baseline was conducted. More than 533 h[12] of electronic noise, based on the PSD of one of the DM runs, was simulated and triggered using the same threshold selected for the actual measurements. The results of this simulation, including the number of surviving pulses at different analysis stages, are listed in Tab. 3.4. Overall, the rate of noise spikes passing the trigger (raw triggered data) underestimates the number of noise triggers in real data estimated at ~ 1 Hz based on the amount of singular traces below the trigger in the above-mentioned 66 h sample. It is likely that a majority of the very fast large noise spikes are not properly represented in the PSD of the data samples. This is because the PSD is determined from much larger time windows

[11] TES module A is no longer in use after both TES chips were found to have cracked in Fall 2023.
[12] Longer than the performed DM search runs.

	triggered pulses	rate [Hz]
raw triggered data	5848	0.003
post pulse finder	3492	0.0018
post loose cuts	1	$5 \cdot 10^{-7}$
post tight cuts	0	0

Tab. 3.4.: Number and rate of surviving pulses after $> 533\,\mathrm{h}$ of electronic noise simulation at different analysis stages. These stages include the number of surviving pulses after the pulse finding algorithm and after dedicated cuts on photon-like signals, which will be discussed in detail in Sec. 4.2.2.

(80 µs) compared to the duration of brief spikes ($\sim 100\,\mathrm{ns}$). As a result, these spikes are underrepresented in the simulation. This is further investigated at the end of this section. The referenced analysis stages include the triggered pulses surviving the pulse finder and the number of pulses surviving dedicated cuts on fit parameters to identify photon-like signatures (τ_+, τ_-, χ^2_{dof} and t_0). This simulation predicts, that the electronic noise baseline should not contribute to the number of surviving photon-like signals after the entire analysis pipeline. It also shows, that $\sim 60\,\%$ of triggered noise pulses can still survive the pulse finder, but are consequently removed by the imposed event selection cuts, which are discussed as part of the detailed analysis discussion in Sec. 4.2.2. However, some noise spikes can even pass such an event selection, since for events with low SNR the probability increases that the fitting function describes a noise fluctuation resembling a photon signal. The single sample surviving the analysis pipeline including the loose cuts is shown in Fig. 3.11. The uncertainties in frequency domain are based on the root-mean-square FFT amplitude of the noise scaled by $1/\sqrt{(2)}$: $\sqrt{T \cdot \mathrm{PSD}/2}$, where T is the window size in µs.

It is evident that the fit function describes a fluctuation in the noise baseline, omitting the contribution of the spike that caused the trigger. The fitted function would not pass the trigger threshold. For such low amplitudes, the separation power of the pulse finder deteriorates. However, the trigger level is set such that these baseline fluctuations would not contribute to the data if they were not on top of an underlying spike fluctuation. The actual single time traces surpassing the threshold are not reproduced by the fit. Therefore, fit parameters like rise and decay time mimic values that might be within photon-like event selection windows. Especially the FFT-χ^2_{dof} still shows a good value due to the low SNR, where noise fluctuations resemble photon signals within the uncertainties[13]. This is evident when examining the real and imaginary part of the signal in frequency domain in Fig. 3.11 (a) and (b). When comparing these to a real pulse as in Fig. 3.1 it is evident that the bins in frequency domain are dominated by uncertainties, resulting in a good χ^2_{dof} value, only based on noise fluctuations.

[13]The χ^2_{dof} is determined using *ROOT*'s TF1 function class.

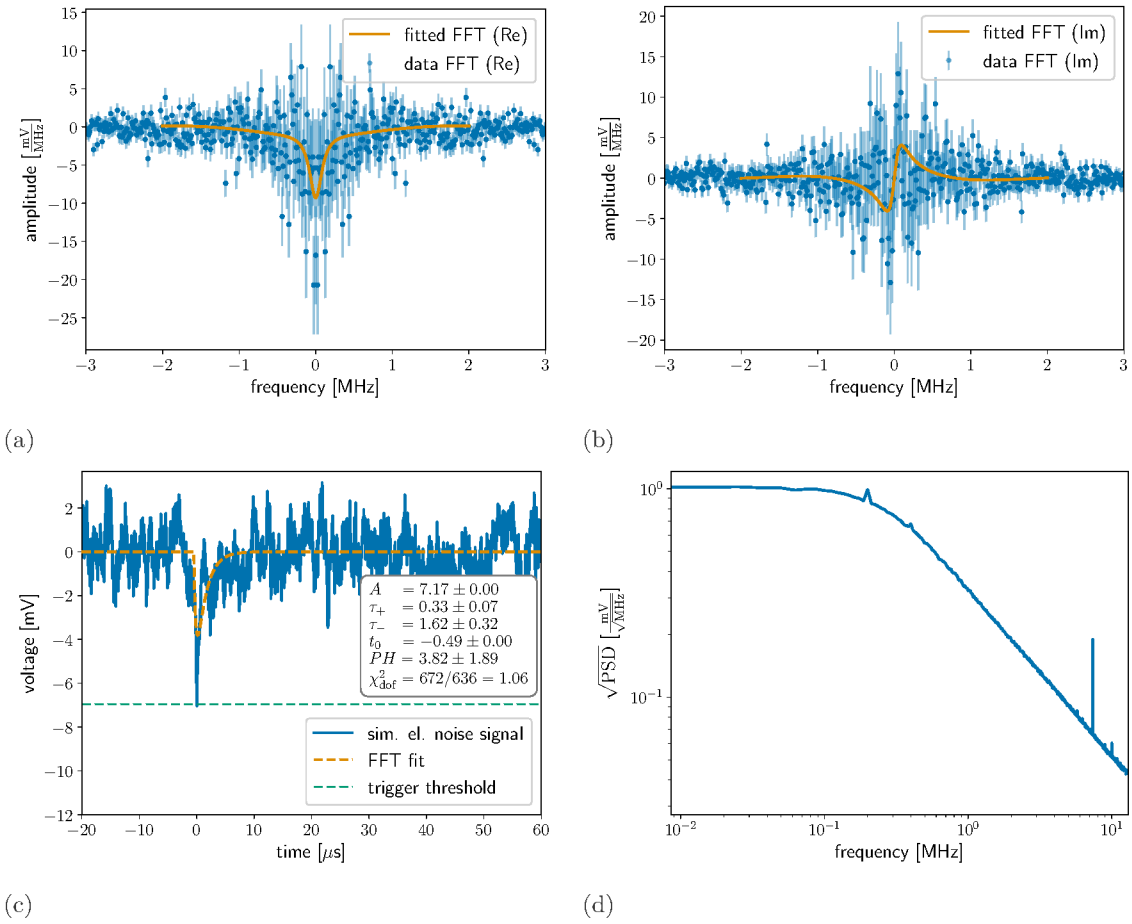

Fig. 3.11.: Example of a fitted (FFT) simulated electronic noise signal: (a) Real part and (b) imaginary part of the signal in frequency domain including respective FFT fits and uncertainties. (c) FFT fit in time domain representation, including fit parameters, (d) square root of the PSD based on the corresponding noise of the dataset. This noise fluctuation slightly surpassing the trigger level shown by the dotted line, passed the analysis pipeline including dedicated cuts supposed to isolate photon-like pulses. The lowest data point of the signal is recorded at −7.04 mV.

As considered in more detail in App. E, a fast spike with a minimum of $V = -15\,\mathrm{mV}$, modeled as a finite-width Dirac delta approximation, does not significantly contribute to the fit in frequency domain, as the modeled spike would only contribute with an amplitude of $0.3\,\frac{\mathrm{mV}}{\mathrm{MHz}}$, much smaller than the uncertainties within the fit range. Compared with the noise, such fast fluctuations would only be present at very high frequencies beyond ∼20 MHz. In this case the maximum fitted frequency at 2 MHz, rendering small spikes invisible. As the high frequencies are dominated by SQUID noise, the fit is usually limited to lower frequencies.

Therefore, while the separating power of the χ^2_{dof} parameter is well-suited to distinguish deviating shapes for slower pulses at high amplitudes, it is limited for fast fluctuations within the noise baseline. Consequently, such cases must be considered in cutting schemes

as well and excluded by introducing additional cuts. This will be discussed in more detail in Sec. 4.2.2. Another option is to take into account fits in the time domain as well, which will be introduced as one of the options for different cutting schemes.

Overall, the optimization procedure positions the setup of both TES modules with optimized conditions for low threshold and low background detection through good energy resolution and signal to noise ratio. The evaluation of the detectors' responses to different energies can be extrapolated to lower energies as well and used for a cut-based event selection in dedicated DM searches. This event selection is supported by the understanding of different intrinsic background sources present in the system, which can be mitigated through dedicated analysis methods.

4 First TES Direct Dark Matter Searches

This chapter discusses the first direct DM searches performed with a TES detector as both target and sensor simultaneously by using the setups and detector modules discussed in previous sections and building on the calibration and optimization work. This includes the first DM search run employing TES module D, also planned for operation in the ALPS II experiment, and a first preliminary run with TES module F specifically adjusted for direct DM searches. Section 4.1 outlines the conducted measurements for both sensors, while Section 4.2 focuses on the analysis pipeline, including preparations, event selection, and resulting energy spectra. The results are presented for TES D and results regarding TES F are found in App. G. Next, the statistical methods used to calculate exclusion limits are considered in Section 4.3, and finally, Section 4.4 compares the results for different modules to each other and discusses the results within the broader framework of light DM searches, as well as possible future prospects.

The analysis pipeline is described and optimized in detail for TES D. The same analysis scheme is applied to the data recorded with TES F as well. As the signals and the noise differ quite heavily for the different modules, the analysis of TES F is discussed as preliminary by employing a similar scheme as with TES D. Due to the differences detector response, further optimization should be considered in the future. Nevertheless, the TES F results can still be used to predict a preliminary sensitivity in the DM-scattering parameter space.

4.1 Dedicated Dark Matter Measurements

After both optimization and calibration of the used TES modules have been performed, dedicated DM runs are conducted. Using the DM experimental setup described in Sec. 2.4.3 and the GBWP and working point combinations found in Tab. 3.2, it is imperative to not only find a suitable and sufficiently low trigger level, but also to record additional calibration samples before starting the measurement. A more detailed description of necessary preparations and instructions to find a suitable trigger level are summarized in App. F. As for the calibration, samples from both 1064 nm and 1640 nm lasers have been recorded before the measurement, to be used for the energy calibration later. In addition 1064 nm samples have been recorded in between consecutive measurements during the same measurement campaign to observe the stability of known pulse shapes and exclude a drift in

detector response. These in-between samples showed a stable detector response overall, as the average signal shape is nearly identical. Measurement campaigns are split into multiple consecutive measurement to investigate the system's stability and for in-between dilution refrigerator maintenance. Table 4.1 shows the different DM runs and their respective data rates and trigger levels for campaigns conducted with both TES modules D and F. Due

TES module	duration [h]	triggers	rate [Hz]	trigger level [mV]
D	66	277 691	1.17	5.6
	166	215 418	0.36	
	166	253 850	0.42	
	91	120 986	0.37	
F	96	497 689	1.44	4
	240	3 673 931	4.25	
	64	695 985	3.02	

Tab. 4.1.: Overview of DM measurement runs for TES modules D and F. The table shows duration, trigger counts, corresponding hardware trigger level, and recorded event rate. All measurements listed for one module have been performed in the same cool-down.

to the lower pulse heights of photon signals in TES F a lower trigger level was chosen for these searches, compared to TES D. This results in a higher trigger rate from the beginning, which showed some fluctuations over the course of the measurement campaign. For TES D, the higher trigger rate in the first measurement was reduced for the second and remained rather stable for the remaining measurements. Figure 4.1 shows the cumulative triggers recorded for both DM runs and the times when each of the single measurements ended. Interestingly, for TES D the rate drops immediately after starting the second run, therefore a connection to the process of starting a new measurement can not be excluded. For TES F the first run has the lowest rate on the other hand, which rises significantly in the first half of the second run and then reduces and remains rather constant throughout the remainder of the measurement campaign. The origin of the differences between the trigger rates for different measurements of the same campaign most likely arises from a shift in the position of the noise baseline. The majority of triggers represent electronic noise spikes, therefore a small shift in the noise baseline can already account for these rate differences. The noise baseline in the DAQ system when triggering is not centered around zero, but has a certain offset. This offset is accounted for in the fitting analysis. When comparing the noise baseline offset of the first run, 1.411 mV, and last run, 1.609 mV of the TES F module, the offset is not the same. Considering the trigger threshold remains stable over these measurements, and since the thresholds are set close to where noise spikes become dominant, this baseline shift can account for the strong fluctuations in trigger rate. However, why these fluctuations appear and how this effect could be mitigated still needs to be investigated and possibly optimized for future campaigns.

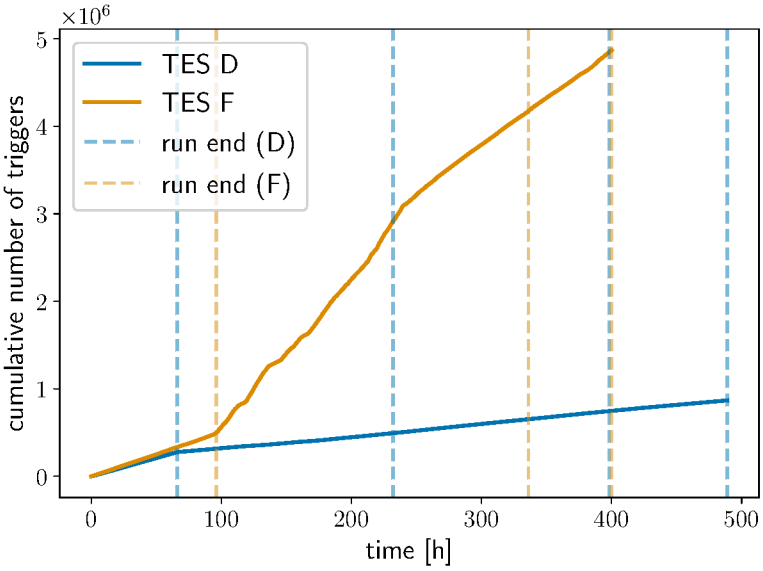

Fig. 4.1.: Cumulative triggers of the two DM run campaigns performed with TES D and TES F. The dashed lines denote the end of a measurement.

4.2 Analysis

The main goal of the analysis is to isolate photon-like pulses from the DM runs. As perviously mentioned in Ch. 1, signals originating from the interaction with DM are expected to equal signals from the energy deposition of photons. Through a dedicated event selection simple cuts are applied on fit parameters. In a previous step, the pulse finder already removes pulses not matching its selection criterion and subsequently additional methods are employed to remove remaining electronic noise spikes and other backgrounds. The parameters used to tune the pulse finder for both modules are listed in Tab. 4.2 and based on the pre-run calibration samples. The event selection is motivated not only by

TES module	**model τ_+ [µs]**	**model τ_- [µs]**	**dec. filter [MHz]**	**dec. threshold [mV]**
D	0.36	1.93	0.5	6.7
F	0.10	0.83	1.0	5.0

Tab. 4.2.: Overview of the pulse finder parameters used for the DM measurement runs for TES modules D and F. The table shows the used model rise and decay time, the low pass filter frequency for the deconvolution and the deconvolution threshold to declare a found pulse.

measured calibration samples, but also by the simulation of a broad energy spectrum to gauge the selection's and detector's acceptance of pulses of a wide range of energies. Cuts yielding sufficient acceptance for photon-like signals are then imposed on the DM datasets

and result in energy spectra representing signals that cannot be accounted for by intrinsic backgrounds from substrate interactions.

4.2.1 Preparation

Calibration samples are required at the beginning of a measurement run. These samples are used for energy calibration to determine the resulting energy spectrum. The samples are also used to calibrate a signal simulation of a broad energy range. Therefore, calibration samples of 1064 nm and 1640 nm are recorded before each campaign[1], providing valuable information, for the analysis. This includes the pulse shapes for the corresponding energies and their energy resolution. Based on the results of Sec. 3.3, the linear relationship between pulse integral and energy for photon-like signals is extrapolated. Hence, linearity is assumed over a broad energy range. New calibration data is needed for each new cool-down or change in TES or SQUID settings[2].
Next, to gauge the total acceptance $\mathcal{A}_i$ in an energy bin i

$$\mathcal{A}_i = \alpha_i^{\text{trig}} \times \alpha_i^{\text{ana}} \times \alpha_i^{\text{cut}} \tag{4.1}$$

over a broad energy range, the acceptance of the hardware trigger α_i^{trig} and the analysis including the pulse finding algorithm α_i^{ana} need to be determined first. The total acceptance is then defined by multiplying the resulting acceptance $\alpha_i^{\text{trig}} \times \alpha_i^{\text{ana}}$ with the acceptance of the respective event selection cuts α_i^{cut}. Therefore, signals of various energies are simulated based on the analyzed calibration samples. These simulated signals, are used to gauge suitable event selection cuts by comparing the fit parameter distributions of both calibration and simulation data sets, since the simulations provide not only a larger energy range beyond what is measured in the laboratory, but also a pure dataset without background triggers. The TES saturates above a certain energy deposition[3], which leads to distorted pulse shapes (see Fig. 3.9). Therefore, the broad band energy simulations, reproduce pulses up to an energy of 3 eV, as this is the highest energy measured with a similar TES chip in the past, which still showed a linear behavior of the average pulse response [64]. The following simulations are performed using the *TESPASS* framework as described in Ref. [58]:

- *calibration*: 1.165 eV (1064 nm) and 0.756 eV (1640 nm) (1000 pulses each)
- *bin-wise*: energy depositions from 0.1 eV to 3 eV (10000 pulses each, evenly distributed in 0.1 eV intervals)

[1] In the same cool-down as the actual DM search.
[2] A full calibration with the current setup takes multiple days, reducing the length of the actual DM search run when performed in the same cool-down. To speed up this procedure, only two wavelengths are recorded before DM runs. See Sec. 3.3 for a full calibration, from which linearity and stability are extrapolated.
[3] This might also concern interactions with higher mass DM particles.

- *spectrum*: evenly distributed signals between 0.1 eV to 3 eV (100000 pulses)

The *bin-wise* simulated intervals of 0.1 eV, wherein the signal energy is evenly distributed between the different samples, will be used to gauge the acceptance $\mathcal{A}_i^{\text{tot}}$ in each energy bin i of the same size. The width of the simulated bins is chosen at 0.1 eV based on the approximate energy resolution of ~ 0.1 eV at 0.756 eV. This refers to the energy resolution determined with the pulse integral, which is the linear parameter used for the energy calibration. Each of the listed simulations reproduces both the baseline noise, signals and also the hardware trigger using the same trigger level as in the DM run. Therefore at first, it can be used to gauge the trigger acceptance α_i^{trig} for different energies. By subsequently conducting the same fitting analysis as for the DM data, the acceptance of the analysis α_i^{ana}, governed by the pulse finding algorithm, can be gauged as well. Table 4.3 shows the trigger acceptance and combined trigger and analysis acceptance for the different simulations. The

Simulation	1.165 eV	0.756 eV	0.1 – 3.0 eV
α^{trig}	100 %	100 %	89.3 %
$\alpha^{\text{trig}} \cdot \alpha^{\text{ana}}$	96.2 %	95.8 %	86.3 %

Simulation [eV]	0.1–0.2	0.2–0.3	0.3–0.4	0.4–0.5	0.5–0.6	≥0.6
α^{trig}	0.11 %	3.2 %	25.6 %	71.2 %	96.6 %	> 99.9 %
$\alpha^{\text{trig}} \cdot \alpha^{\text{ana}}$	0.09 %	3.0 %	24.5 %	68.6 %	93.5 %	> 96.1 %

Tab. 4.3.: Trigger and combined trigger and analysis acceptance across different simulations for TES D: Top: *calibration* simulation for the two wavelengths and *spectrum* simulation, bottom: *bin-wise* simulation. The uncertainties on the acceptances are on the order of 0.1 %.

corresponding acceptances for the measurement with TES F is listed in App. G.1. All simulations are performed using the same trigger as in the DM measurement. Indeed all signals of the two simulated calibration points pass the hardware trigger, but not all of them survive the pulse finder. The signals with a higher amplitude are more likely to be accepted compared to lower amplitudes. Observing the overall full *spectrum* simulation from 0.1 eV to 3.0 eV more than 86 % of pulses survive both the hardware trigger and analysis. However, this value is biased towards larger energies, since the *bin-wise* simulation shows strongly reduced acceptance values for lower energies. Around and below 0.4 eV less than half of the signals do not pass the trigger, although of the ones that do, a majority still survives the analysis. In theory, this shows the low-energy sensitivity of the TES system, which is still able to trigger more than a quarter of signals above 0.3 eV. In a next step, these acceptance values will be used to gauge the total acceptance of the entire analysis pipeline for each energy bin after the event selection.

4.2.2 Event Selection and Acceptance

Before discussing the chosen cuts, the distributions of the fit parameters of the measured DM search run can be compared with the distributions of the measured calibration pulses. First, the performance of the pulse finder is investigated. The amount of events surviving the pulse finder and therefor being fitted is shown in Tab. 4.4. The pulse finder is able to

TES module	duration [h]	triggers	events surviving pulsefinder
D	66	277 691	13.61 %
	166	215 418	18.90 %
	166	253 850	10.24 %
	91	120 986	10.69 %
F	96	497 689	41.68 %
	240	3 673 931	39.39 %
	64	695 985	42.46 %

Tab. 4.4.: Overview of DM measurement runs for TES modules D and F. The table shows duration, trigger counts and the percentage of events surviving the pulse finder. All measurements listed for one module have been performed in the same cool-down. The statistical uncertainty on the fraction of events surviving the analysis is below 0.1 %.

reduce the amount of recorded pulses more effectively for TES D than TES F. Considering this and also the higher rate recorded with TES F, the differences in module setup (no fiber sleeve, copper cylinder) do not seem to reduce the rate of dark counts recorded with the sensor. However, given the low trigger threshold, the background rate mainly depends on the module's noise and not other backgrounds e.g. from radioactivity. For measurements with such low trigger rates it is hard to determine the impact of the adjusted TES F module compared to TES D. Considering the much faster photon-like signals compared to TES D, a higher amount of noise spikes passing the pulse finder is likely. The current pulse finder might not be able to isolate photon-like pulses in this sensor effectively enough. It was originally optimized for sensors with signal shapes of photon pulses similar to TES D [58], whereas $\tau_+ \approx 0.17\,\mu s$ and $\tau_- \approx 0.85\,\mu s$ in TES F (compared to $\tau_+ \approx 0.35\,\mu s$ and $\tau_- \approx 2\,\mu s$ in TES D and $\tau_+ \approx 0.77\,\mu s$ and $\tau_- \approx 3.1\,\mu s$ in TES A[4]). The results of this DM search with TES F will still be used to gauge a preliminary sensitivity of the TES F module as well, which might improve with further optimization e.g. of the pulse finder, which is beyond the scope of this thesis. Figure 4.2 shows the post pulse finder results for the fit parameters from the combined DM searches of TES D listed in Tab. 4.1, compared with the results of the photon calibration samples recorded before the first measurement. A logarithmic depiction without normalization to observe the contribution of outliers is included in App. H. Especially from the distributions of the rise and decay time parameters,

[4]This was the original TES module the pulse finder was developed with. More information see App. A

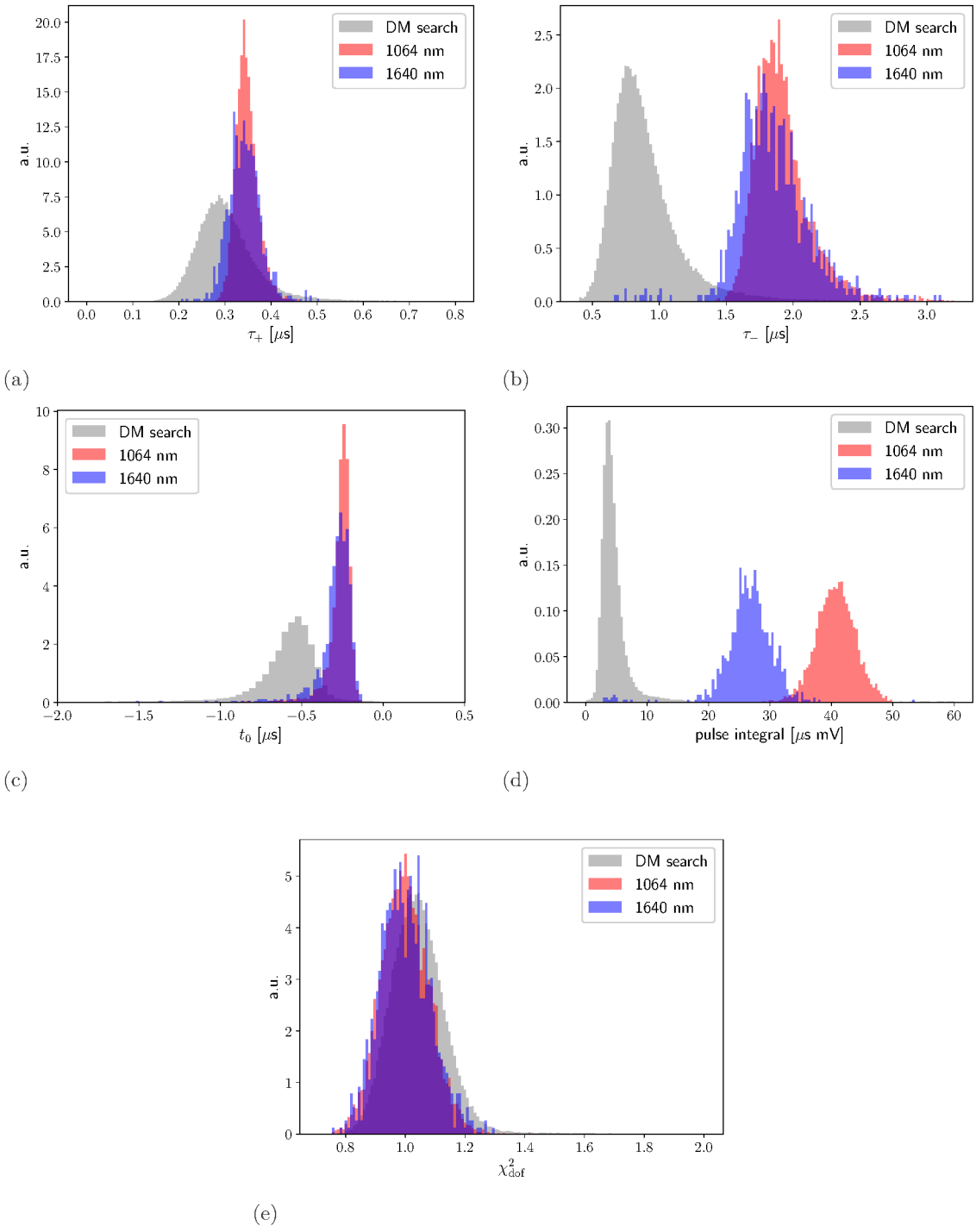

Fig. 4.2.: Distribution (normalized to the same integral) of fit parameters (post pulse finder) showing both DM search measurement and laser calibration data: (a) rise time (b) decay time (c) start time (d) pulse integral and (e) χ^2_{dof}. The x-ranges are zoomed-in to allow comparison between the main features of the datasets, outliers outside of these regions exist.

it is clear that the majority of recorded triggers in the DM search run surviving the pulse finder lie outside of the region of interest for photon-like pulses. There is some overlap for

rise time parameter τ_+ between the DM search and the calibration data, while the majority of triggered pulses show a much lower τ_- parameter. This points toward the majority of recorded background pulses being noise spikes as in Fig. 3.11, as opposed to backgrounds arising from energy depositions in the substrate such as slow pulses (longer decay time, see Fig. 3.9) or photon-like signals.

Even when the majority of signals in the DM search data originates from fast noise spikes, especially the rise time is fast (compared to the decay time) for the photon signals as well. However, large portion of the DM search data still shows rise times below that of the calibration pulses. In addition, the start time t_0 of the pulses, shows an overlap as well, as it pinpoints the time where the pulse starts to rise from the baseline. The start time of the pulse depends mainly on the position of the trigger and the rise time as well. The deviations between the datasets therefore arise mainly from a different trigger level used for the calibration pulses (9 mV for 1064 nm and 6 mV for 1640 nm as opposed to 5.6 mV for the DM search). The trigger levels are adjusted for the calibration samples, to avoid contamination by backgrounds from lower energies. The size of the x-axis still demonstrates the value of the t_0 parameter, which can mainly be used to find distinct outliers and bad fits, where the start time strongly deviates from the position of the trigger. Outliers mostly point towards noise triggers (similar to Fig. 3.11), where the fit describes some noise fluctuation prior to or after the triggered time trace. These arise mainly from noise spikes being triggered and recorded. If the pulse finder subsequently misidentifies a noise fluctuation in the same timeline as a pulse, this fluctuation is fitted instead, leading to the shifted t_0. On the other hand, the decay time parameter τ_- shows a large deviation from the majority of triggers recorded in the DM search run with much shorter decay times. This also points toward the majority of DM search pulses being fast noise spikes, which might have similar rise time than photon pulses, but lacks the characteristic decay time of actual energy depositions in the sensitive TES, as its temperature returns to its equilibrium position. The pulse integral shows a majority of pulses with integrals below 10 µs mV, again pointing towards fast noise spikes with a comparatively small pulse area. Therefore, the distinction from noise for higher energies is more straight forward, while for much lower energies, the signals could reach into the majority of recorded pulses. Overall, the cuts on the timing parameters are the most important and especially their combination will be able to effectively isolate photon-like pulses from backgrounds and fast noise spikes. The pulse integral parameter of the remaining pulses will be used to calculate a resulting energy spectrum. As discussed in Sec. 3.4.2, noise spikes can still mimic a good χ^2_{dof} value in frequency domain, which is visible for the distribution of the DM search as well. Therefore, the χ^2_{dof} cuts are used to isolate outliers, but in this case the parameter is not sufficient to isolate fast noise spikes.

For the event selection, fit parameter distributions of the different calibration samples (simulations and data) are compared in 1D and 2D histograms, and cut regions are chosen,

among others, based on the pulse shape assumptions concerning rise and decay time confirmed in Sec. 3.3. Three different sets of cuts are applied to the DM search data, which will be referred to:

- *loose* cuts
- *tight* cuts
- *systematic* cuts

In applying different cuts, their impact on the sensitivity to DM interactions can be observed and allows for a comparison between these cutting schemes. The first two cut schemes, one broader selection called *loose cuts* and a more narrow selection called *tight cuts* are chosen by visual inspection of respective simulated and measured calibration histograms as described in the following. The goal is to cut away most of the background we see, by placing narrow cuts allowing for a total acceptance of around $\geq 50\,\%$ at $\sim 1\,\mathrm{eV}$ for the *loose* cuts, and around $\sim 10\,\%$ at $\sim 1\,\mathrm{eV}$ for the even stricter *tight* cuts. These are based on the measured and *simulated calibration* samples as well as the simulated energy *spectrum* from $0.1\,\mathrm{eV}$ to $3.0\,\mathrm{eV}$. The higher acceptance in the *loose* cuts allows for higher background levels in the final energy spectrum, while the reduced acceptance in the *tight* cuts attenuates this background. These cuts pose a first simple gauging of the sensitivity of the DM search with the FFT analysis. A third set of *systematic cuts* was subsequently introduced by cutting on results of a combined analysis using fitting schemes in both the frequency and time domain in a more systematic manner. The analysis in time domain therefore uses the phenomenological fitting function from Eq. 1.30. This introduces additional parameters to cut on, while keeping an acceptance comparable to cutting-schemes based on frequency domain fits only.

For this purpose the total acceptance $\mathcal{A}_i^{\mathrm{tot}}$ in each bin is defined by trigger, analysis and cut selection acceptance following Eq. 4.1, and will be discussed at the end of this subsection. The acceptance for signals of certain energies in each bin will later be taken into account when calculating constraints, where even small acceptances yield valuable information regarding sensitivity to DM interactions, due to the long exposure time.

The tables listing the cut parameters for TES F and corresponding figures are part of App. G.1.

Rise and Decay Time

The *loose* and *tight* cut regions are chosen based on the 2D rise and decay time distributions of the *simulated calibration* and compared to the measured samples of 1064 nm and 1640 nm as well, to ensure the cuts accommodate the distributions of both calibration wavelengths. Based on the results from Sec. 3.3, we assume the rise and decay time to be mostly constant

over the entire simulation range for photon-like events. This assumption is also included in the signal simulation already. The *tight* cuts are simply symmetrically shrinking the *loose* cut range. These 2D distributions are shown together with the cut ranges in Fig. 4.3. Especially the *loose* cuts are comfortably accommodating a majority of simulated signals,

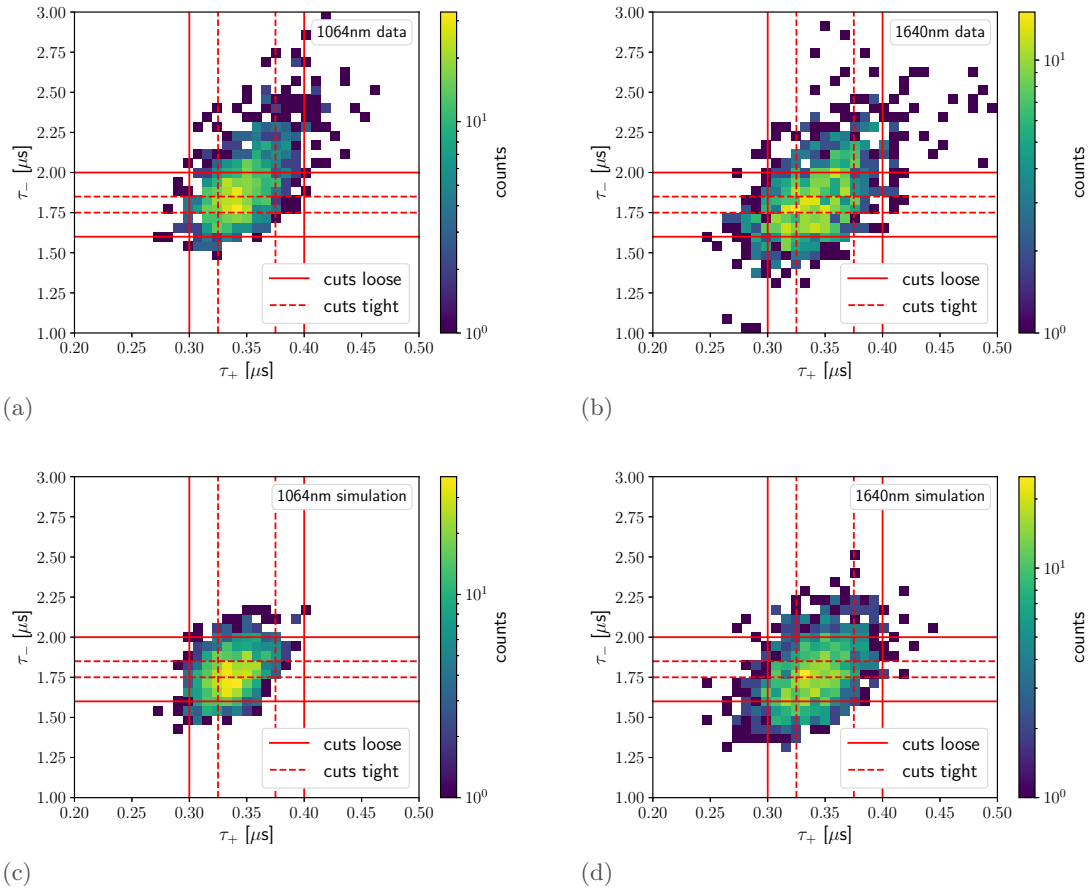

Fig. 4.3.: 2D distribution of the rise and decay time of measured and *simulated calibration* samples: (a) 1064 nm data (b) 1640 nm data (c) 1064 nm simulation (d) 1640 nm simulation. The solid and dashed red lines show the placement of *loose* and *tight* cuts, respectively.

which are more localized compared to the measured data. The measured data shows outliers and backgrounds passing the trigger threshold as well, where a majority is removed by the imposed cuts. Figure 4.4 shows the 2D distribution of rise and decay time parameters for the simulated *spectrum* from 0.1 eV to 3 eV including both cut schemes. As shown in Tab. 4.3, the combined trigger and analysis acceptance shrinks for lower energies, while it is almost 100 % for higher energies. Therefore, the cuts are mainly chosen based on the data and simulation samples around and below 1 eV to accommodate for lower energies. This leads to the *loose* and *tight* cuts being off-center for the *spectrum* distribution ranging from 0.1 eV to 3.0 eV, but allows for increased acceptance to lower energies, while only slightly limiting the acceptance for higher ones. This will be shown at the end of this subsection.

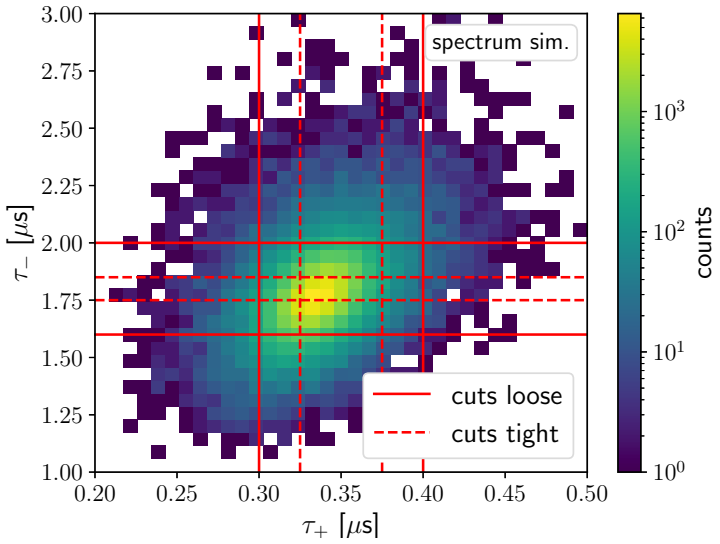

Fig. 4.4.: 2D distribution of the rise and decay time of simulated *spectrum* over the whole energy range from 0.1 eV to 3 eV. The solid and dashed red lines show the placement of *loose* and *tight* cuts, respectively.

The *systematic* cuts for both $\tau_{+/\text{rise}}$ and $\tau_{-/\text{decay}}$ are based on Gaussian distributions fitted to each 1D parameter histogram based on the simulated *spectrum*-only. The cut regions are chosen as the 2σ regions around the mean of each, for both time and frequency domain fit parameters. Therefore, this scheme is based on the entire energy range and not adjusted to lower energies. The same holds true for the cuts on TES F data.

Pulse Arrival and χ^2_{dof}

The pulse arrival time t_0 and the χ^2_{dof} are used for the event selection as well. Signals where the arrival time deviates strongly from the mean value can be mostly traced back to accidental fitting of noise spikes or background signals of strongly deviating pulse shape. Similarly, outliers outside of the central χ^2_{dof} region represent a deviation from the expected pulse shapes. The simulation and data samples together with the cut regions are visualized in Fig. 4.5. As of now, the simulated start time t_0 of the pulse deviates from the t_0 value arising from fits on measured data sets. In *TESPASS*, the signals are simulated such that the start time of the fit function is centered around $t_0 = 0$. For measured signals, t_0 is usually negative, as $t = 0$ is the position where the pulse is triggered on its rising edge. As is visible from Fig. 4.5(b), the measured start times deviate from this. Therefore, the cuts will only be used to cut away distinct outliers (the figure's x-axis is zoomed in, as outliers, especially for negative values reach far beyond this window) based on the measured calibration data, without cutting on the simulated *spectrum* and therefore not influencing the total acceptance $\mathcal{A}^{\text{tot}}$. From the distribution of the measured calibration samples,

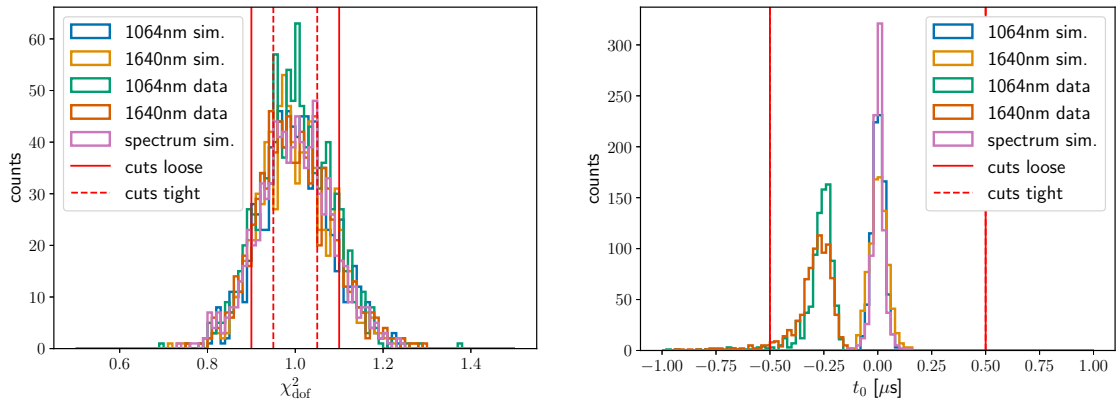

(a) (b)

Fig. 4.5.: Distributions of fit parameters of measured and *simulated calibration* samples: (a) χ^2_{dof} distributions and (b) t_0 distributions. The solid and dashed red lines show the placement of *loose* and *tight* cuts, respectively, which are the same for the pulse arrival time t_0.

$t_0 = \pm 0.5\,\mu\mathrm{s}$ is chosen to cut symmetrically around 0. It should be noted, that this is one of the limiting factors concerning the acceptance determination and should be considered in future improvements. As evident by the example noise spike discussed in 3.4.2, the χ^2_{dof} cut is currently not able to reject all spiked triggers, where the noise baseline is fitted. Therefore, additional cuts need to be introduced to mitigate this.

The *systematic* cuts are based on a Gaussian distribution fitted to the χ^2_{dof} histogram based on the simulated *spectrum*. This approach is different for t_0, where most outliers in real measured data sets are negative and the measured distribution is skewed to the left. The aim is to again reduce the amount of distinct outliers without influencing the acceptance of signal pulses by cutting on the simulated data. Therefore, the 1640 nm measured calibration dataset is used to find a cut region, since it shows most outliers with its comparatively low trigger level of 6 mV. This time, the data is cut below the lower 99.73 % percentile, and vice-versa for the positive value of the corresponding cut parameter. This is again performed for both analyses in time and frequency domain. The same holds true for the cuts on TES F data.

Noise Spikes

In Section 3.4.2 the large contribution of baseline noise spikes to the data rate for low trigger threshold measurements was discussed. Such events passing the pulse finding algorithm are not always rejected by the fit parameter cuts, due to fits mimicking a photon-like contour inside noise baseline fluctuations. As investigated before, these pulses are not always removed by the χ^2_{dof} cuts and could contribute to the final energy spectrum if they are not removed by cuts on other parameters. Since only photon-like pulses with a pulse height above or close to the trigger threshold should be represented in the energy spectrum and

the χ^2_{dof} cuts are not always reliable for these noise spikes specifically, a different approach is needed to isolate these remaining spikes. For this purpose, the compatibility between the minimum of the pulse and fitted pulse height should be considered and investigated with different methods. As visible in the example event of Fig. 3.11, the pulse height of the noise spike derived from the FFT fitting function $PH = 3.82$ strongly deviates from the actual lowest point of the signal $S_{\mathrm{min}} = -7.04$. This can be represented in the deviation ratio $\mathcal{R}_{\mathrm{dev}}$

$$\mathcal{R}_{\mathrm{dev}} = PH/S_{\mathrm{min}}, \tag{4.2}$$

which is $\mathcal{R}_{\mathrm{dev}} \approx 0.54$ in this case. To gauge proper event selection based on the deviation ratio, the measured 1640 nm calibration sample, as the lowest measured signal with possible background contributions, is used to investigate the ratio's distribution for low energy signals. In Sec. 3.4.2, electronic noise baseline spikes from this calibration sample have been observed together with calibration samples already. Therefore, the histogram of this deviation ratio is investigated and fitted with a normal distribution depicted in Fig. 4.6(a). Based on the mean of the normal distribution ideally, the deviation ratio would be close to

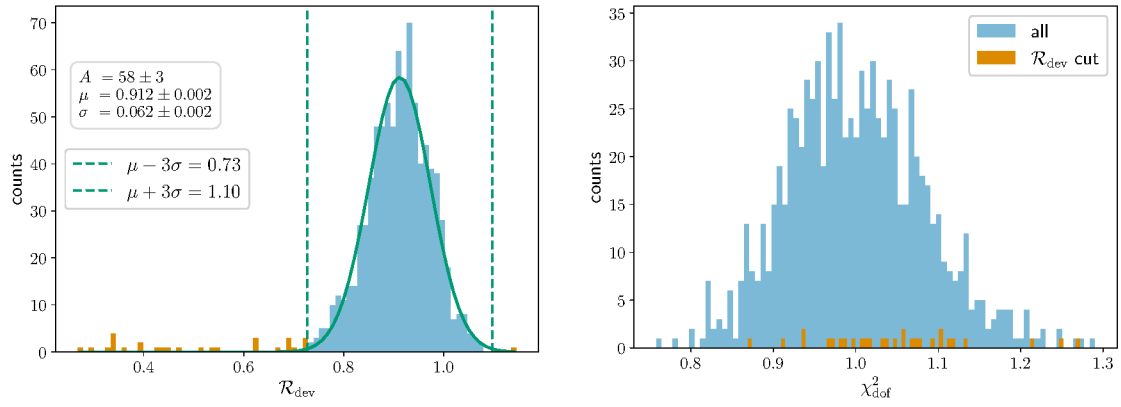

(a) (b)

Fig. 4.6.: Parameter distributions based on the measured 1640 nm calibration sample with all triggers shown in blue and filtered triggers shown in orange for (a) $\mathcal{R}_{\mathrm{dev}}$ distribution fitted with a Gaussian (green line). The green dashed lines shows the 3σ cuts around the distribution's mean. (b) χ^2_{dof} parameter distribution.

~ 0.9. Many outliers outside of the 3σ range, marked by dotted lines, are visible, especially for lower ratios, similar to noise spike discussed before.

This is the lowest available measured energy sample with such a low trigger, therefore also including fits to the baseline noise. The 3σ region around the mean is used as an additional selection parameter to remove fits whose pulse height deviates strongly from the minimum measured signal trace. For the 1064 nm sample with a higher trigger level, the number of triggered noise samples is lower, as the lowest deviation ratio is $\mathcal{R}_{\mathrm{dev}} = 0.6$. For the 1064 nm sample the same process results in a 3σ region of $[0.81, 1.08]$, excluding 1.3 %

of total events, compared to 3.3 % for the 1640 nm samples. Example pulses discarded with this procedure based on the 1640 nm calibration sample are found in App. H.1. In future iterations of these experiments, taking samples with the same trigger level as the DM search measurements, could yield more information on the contribution of triggered baseline noise.

This is applied to all different sets of cuts, respectively. While deviations might also occur for pulses from actual energy depositions, the minima of noise spikes often only incorporate a small number of traces reducing the deviation ratio for these triggers. The fact that this behavior is not necessarily represented in the χ^2_{dof} distribution is evident from Fig. 4.6 b) showing the χ^2_{dof} distribution for all triggers and the ones filtered by the 3σ deviation ratio cuts, which are distributed throughout the histogram and do not deviate strongly from $\chi^2_{\mathrm{dof}} = 1.0$. The $\mathcal{R}_{\mathrm{dev}}$ cuts on TES F, follow the same procedure.

All cut parameters for the *loose* and *tight* cut selection schemes are summarized in Tab. 4.5.

cut scheme	τ_+ [μs]	τ_- [μs]	$\chi^2_{\mathbf{dof}}$	t_0 [μs]	$\mathcal{R}_{\mathrm{dev}}$
loose cuts	(0.3, 0.4)	(1.6, 2.0)	(0.9, 1.1)	(-0.5, 0.5)	(0.73, 1.10)
tight cuts	(0.325, 0.375)	(1.75, 1.85)	(0.95, 1.05)	(-0.5, 0.5)	(0.73, 1.10)

Tab. 4.5.: Summary of event selection cuts for both *loose* and *tight* schemes. The cuts are applied to the rise τ_+, decay τ_- and arrival times t_0 of each pulse, including the χ^2_{dof} and the deviation ratio between the pulse height of the fit and the minimum of the recorded pulse $\mathcal{R}_{\mathrm{dev}}$.

In comparison, the *systematic* cuts not only place cuts on the fit parameters from the FFT analysis, but also from fitting the phenomenological function. The cut parameters for the *systematic* cut selection are listed in Tab. 4.6. Note that both FFT and phenomenological

systematic cuts	$\tau_{+/\mathrm{rise}}$ [μs]	$\tau_{-/\mathrm{decay}}$ [μs]	$\chi^2_{\mathbf{dof}}$	t_0 [μs]	$\mathcal{R}_{\mathrm{dev}}$
FFT cuts	(0.31, 0.36)	(1.61, 1.94)	(0.84, 1.16)	(-1.46, 1.46)	(0.73, 1.10)
Pheno. cuts	(0.10, 0.18)	(1.67, 2.27)	(0.41, 0.61)	(-17.87, 17.87)	

Tab. 4.6.: Summary of systematic event selection cuts including both FFT and phenomenological fitting functions, which are combined for the *systematic* cut scheme. The cuts are applied to the rise, decay and arrival parameters t_0 of each pulse, including the χ^2_{dof} and $\mathcal{R}_{\mathrm{dev}}$ of the FFT fit. In this case the fit parameters, except for t_0 were selected using a 2σ region around the mean of the fit parameter distributions of the simulated *spectrum*.

cuts are applied to the dataset simultaneously and the $\mathcal{R}_{\mathrm{dev}}$ cut introduced for the *loose* and *tight* cut schemes are used here as well. More details and respective distributions are found in App. H.

Combined, the selection criteria summarized in Tab. 4.5 and 4.6 effectively and rigorously isolate photon-like pulses under strict criteria. This is reflected in the total acceptance $\mathcal{A}^{\text{tot}}$ for each energy bin, based on the *bin-wise* simulation, summarized for all cut schemes and both TES modules in Fig. 4.7. All cut schemes show lower acceptance at lower energies,

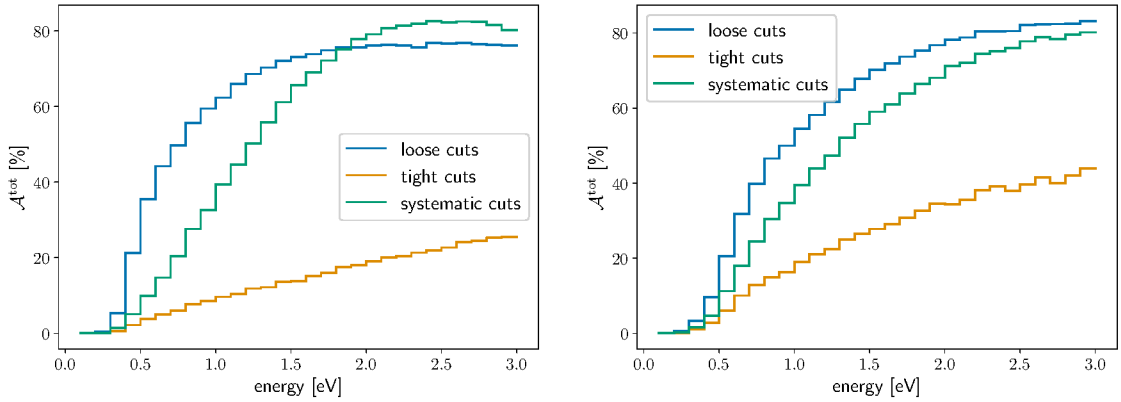

Fig. 4.7.: Total acceptance $\mathcal{A}^{\text{tot}}$ for each energy bin based on the *loose*, *tight* and *systematic* cut schemes for (a) TES D and (b) TES F.

which is dominated by the low trigger acceptance shown in Tab. 4.3. Furthermore, the *loose* and *systematic* cut acceptance saturates for higher energies, while the *tight* cuts linearly increase up to 3.0 eV. Since the systematic cuts where based on the broad energy *spectrum* simulation, they show an overall lower acceptance for lower energies compared to the *loose* cuts. The *tight* cuts rigorously cut away much of the signal space and therefore show an overall lower acceptance for all energies.

4.2.3 Energy Spectra

Finally, the event selection is applied to the fitted DM run data (shown in Fig. 4.2) based on the *loose* and *tight* cuts listed in Tab. 4.5, and the *systematic* cuts listed in Tab. 4.6, respectively. For the resulting data sets, the pulse integral $\mathcal{I}$ parameter is used to translate the results to an energy spectrum based on a calibration relation from the measured 1064 nm and 1640 nm calibration samples and the linearity assumption from Sec. 3.3. The underlying calibration relation

$$E = \frac{\mathcal{I} - 1.76\,\mu\text{s}\,\text{mV}}{33.53\,\mu\text{s}\,\text{mV}\,\text{eV}^{-1}} \tag{4.3}$$

is approximated by a line through two measured calibration points (see App. I). For TES F the relation is

$$E = \frac{\mathcal{I} - 0.49\,\mu\mathrm{s\,mV}}{7.41\,\mu\mathrm{s\,mV\,eV^{-1}}} \tag{4.4}$$

(see App. I). These lines are not drawn through the origin, as the fluctuations in the noise baseline lead to offsets. The same goes for the linear fits for the full calibration, as in Fig. 3.8. This was observed in similar TES systems as well [101].

While this procedure is not ideal for two data points and introduces a potential systematic uncertainty, we use this as an adequate approximation. Comparison with the fit through more calibration points in Fig. 3.8, shows that the resulting deviation in reconstructed energies when drawing the line through two points only, is smaller than the TES energy resolution of approximately $\sim 0.1\,\mathrm{eV}$ at energies around 1 eV.

The resulting energy spectra are shown in Fig. 4.8 (a) and (b). They can also be scaled by the acceptance in each energy bin for the *loose*, *tight* and *systematic* cutting schemes. These are shown in Fig.4.8 (c) and (d), for TES modules D and F respectively. With the lowest bin centered around 0.35 eV pulses for all three cutting schemes are distributed across the entire energy range for TES D. For TES F, the *systematic* cuts yield the lowest number of events (at higher acceptance than the *tight* cuts), showing the improvement of using time domain cuts in addition to the frequency domain ones. This difference is less pronounced for the TES D results, which could indicate further need for optimization in the FFT analysis and pulse finder for TES F. The majority of both spectra is made up of lower energy signals below 1.1 eV, which could point towards LEE contributions, see Sec. 3.4. For TES F, this is even more obvious where the majority of events are below 0.6 eV. On the other hand, this excess is suppressed to some extent with the *systematic* cutting scheme, which could account for a better background reduction with the extended cutting scheme employing both time and frequency domain cuts. The origin of remaining events is unknown, but assuming absence of DM particles, could be attributed to stray photons in our setup or thermal deposits induced by electromagnetic interference in the bias line.

These energy spectra can be compared to the shape of the predicted signal model rate $\mathcal{M}$ based on the scattering rate Γ defined in Eq. 1.39. Therefore, the signal model rate $\mathcal{M}_{i,\mathrm{raw}} = \Gamma_i$ for each energy bin i can be compared to the modified signal model rate, by taking into account the acceptance of the different cutting schemes:

$$\mathcal{M}_{i,\mathrm{cut}} = \Gamma_i \mathcal{A}^{\mathrm{tot}}_{i,\mathrm{cut}} \tag{4.5}$$

The resulting predicted signal model rate for DM-electron scattering signals, is a smooth recoil spectrum as demonstrated in Fig. 4.9 (a) (TES D) and (c) (TES F). The exact

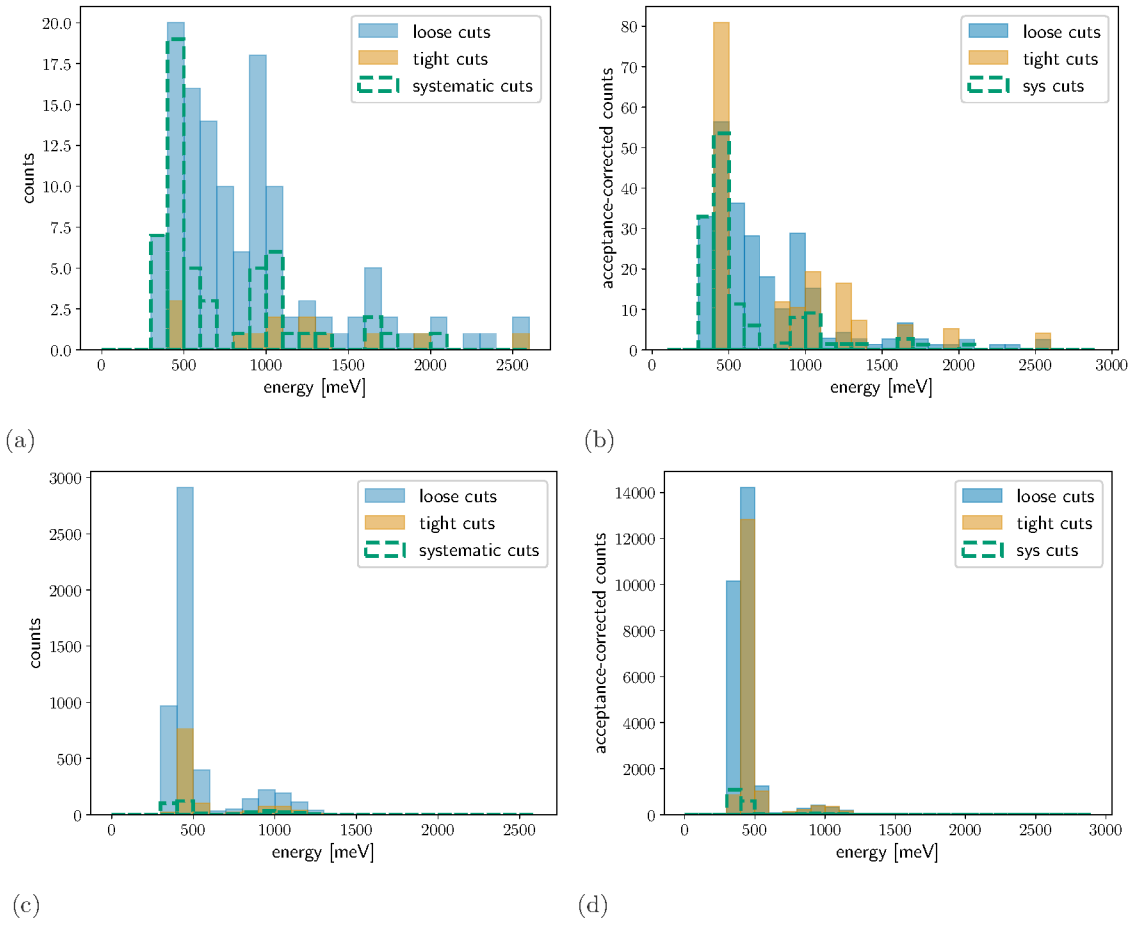

Fig. 4.8.: Energy spectrum for *loose*, *tight* and *systematic* cuts for (a) TES D and (c) TES F. Acceptance corrected energy spectrum for (b) TES D and (d) TES F. The contribution of lower energy signals is enhanced by the low acceptance of the cut schemes for these energies.

numerical rates depend on the coupling constants g_e and g_{DM}, mediator mass m_ϕ, and DM mass m_{DM}. Considering the logarithmic scale, all cut schemes attenuate the detectable signal rate. In comparison, the *loose* cut scheme for TES D and F only slightly attenuates the detectable signal rate above 1 eV, the *tight* cut scheme reduces the same by over an order of magnitude. For all schemes the rate is heavily suppressed below 500 meV.

These curves can be compared to the unscaled energy spectra measured with TES D in Fig. 4.9 (b) and TES F in Fig. 4.9 (d). As no conclusive background model is available, conservative upper limits are calculated instead of fitting the spectra. Therefore, it is assumed that the surviving pulses in the energy spectra are dark counts based on unknown background sources and do not originate from DM-electron scattering. These could originate from unknown photon sources within our setup or scatter from the fiber tip in the vicinity of the TES modules needed for calibration. Further signals could be induced by electromagnetic interference influencing the readout electronics. However, these results can still be used to

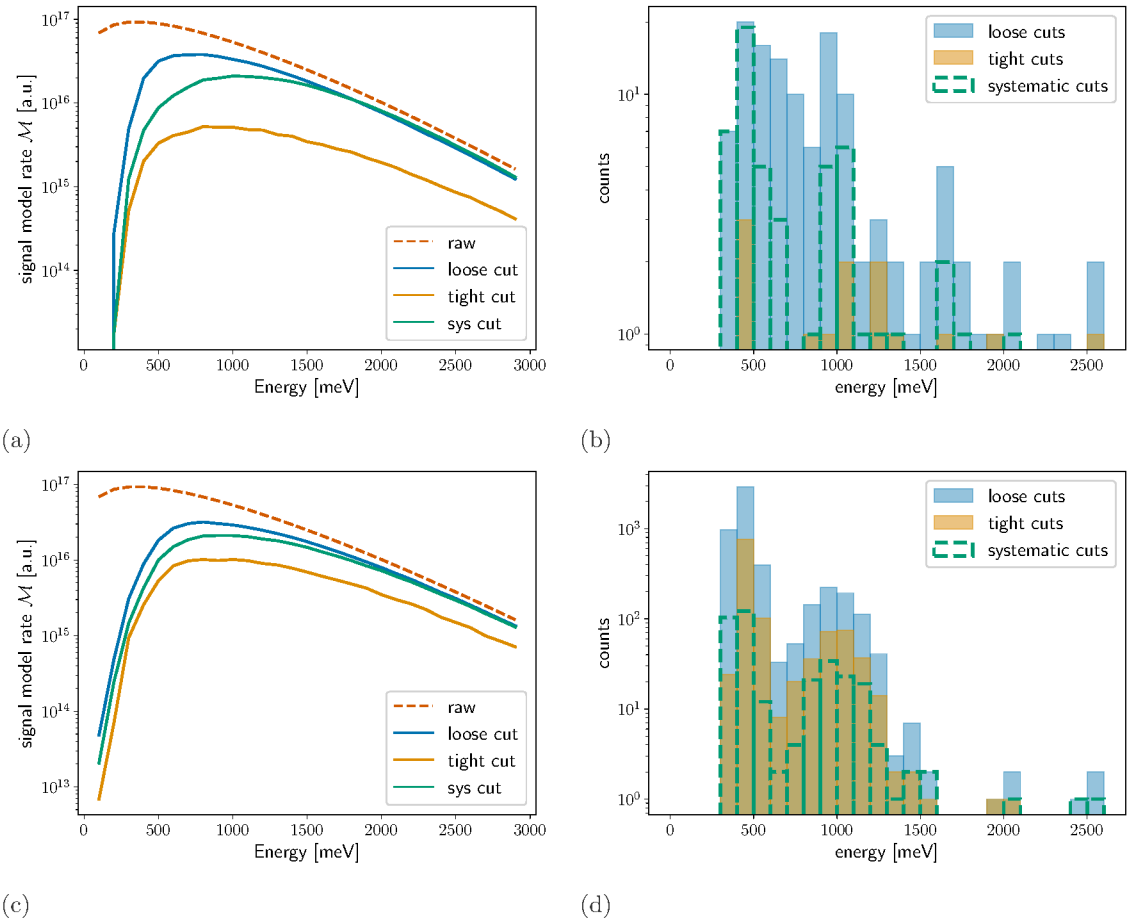

Fig. 4.9.: Expected DM signal models (logarithmic scale) based on the raw DM-electron scattering rate and the modified rates, taking into account the acceptance for each energy bin in arbitrary units for the *loose* and *tight* cutting schemes, respectively. The exact rate depends on the coupling constants g_e and g_{DM}, mediator mass m_ϕ and DM mass m_{DM}, for (a) TES D and (c) TES F. Energy spectrum based on the TES D DM run for the *loose*,*tight* and *systematic* cutting schemes for (b) TES D and (d) TES F

constrain the DM-electron scattering parameter space, even without a dedicated background model. The statistical considerations are discussed in the next section.

4.3 Exclusion Limit Calculation

In a next step, statistical considerations need to be taken into account to calculate constraints in the DM-electron scattering parameter space, based on the findings of the previous section. The procedure is carried out for the *loose*, *tight* and *systematic* cuts, respectively. Considering the lack of a known background model, no assumptions are made on the origins of measured pulses. Therefore, they could originate from both uncontrolled backgrounds or from DM interactions. Conclusively, the following analysis, based on Ref. [103–105], is not able to discover DM, is however capable of setting conservative exclusion limits, taking into account the shape of the recorded energy spectra.

The events in the energy spectra of Fig. 4.9 define the observed event distribution N_i^{obs}, where i represents the energy bins. In a next step, the signal model predicting the expected number of events in each bin is compared to the observed events. These expected DM events N_i^{DM} are again based on the signal model rate first introduced in Eq. 1.36 and is used as a function of the mediator mass m_ϕ, DM mass m_{DM} and interaction cross-section $\bar{\sigma}_e(g_e, g_{\text{DM}})$. For the DM velocity distribution function in the laboratory frame f_{DM}, the standard halo model following Ref. [106] is used: $f_{\text{DM}}(\mathbf{v}_{\text{DM}}) \propto e^{-(\mathbf{v}_{\text{DM}}+\mathbf{v}_{\text{E}})^2/v_0^2}$, with the Earth's velocity $\mathbf{v}_{\text{E}}$ and DM velocity dispersion v_0. The parameters in the galactic frame are listed in Tab. 4.7. Otherwise the calculation follows the definitions in Sec. 1.3.5. Similarly

	halo model parameters
DM density	$0.4\,\text{GeV/cm}^3$
DM velocity dispersion	$220\,\text{km/s}$
local galactic escape velocity	$550\,\text{km/s}$
Earth velocity	$232\,\text{km/s}$

Tab. 4.7.: Halo model parameters used for the calculation of the DM velocity distribution function $f_{\text{DM}}(\mathbf{v}_{\text{DM}})$. The Earth's velocity refers to the velocity relative to the DM halo.

to Eq. 4.5, the expected number of DM events is multiplied with the acceptance $\mathcal{A}_i^{\text{tot}}$ in each energy bin, yielding the expected number of events in the signal model prediction, corrected for the energy-dependent acceptance of the detector:

$$N_i^{\text{signal}}(m_{\text{DM}}, m_\phi, \bar{\sigma}_e) = \mathcal{A}_i^{\text{tot}} N_i^{\text{DM}} \tag{4.6}$$

For the mediator particle, two different cases are considered when comparing the mediator mass with the momentum transfer q to tungsten:

- light mediator: $m_\phi \ll q$
- heavy mediator: $m_\phi \gg q$

For each considered DM and mediator mass the maximum interaction cross section $\bar{\sigma}_e$ (see Eq. 1.38) is determined, which is still compatible with N_i^{obs} and at the same time allowing for subsets to arise from background. Therefore, m_{DM} and m_ϕ are fixed and a profile likelihood-test is performed, where the spectral information gained through the energy-resolving capabilities of the TES are taken into account. As mentioned before, no assumptions about the backgrounds are imposed during this analysis. Therefore, the goal is to constrain the scattering cross-section $\bar{\sigma}_e$ with undetermined nuisance parameters N_i^{bg}, defined as the mean of the Poisson distributed background rate. Subsequently, two hypotheses are defined, one where the observed events incorporate DM signals as well

$$\ell_{\mathrm{DM}} \equiv \log \mathcal{L}_{\mathrm{P}}\left[N_i^{\mathrm{obs}} | N_i^{\mathrm{bg}} + N_i^{\mathrm{signal}}(\bar{\sigma}_e)\right], \tag{4.7}$$

and the background-only hypothesis:

$$\ell_{\mathrm{bg}} \equiv \log \mathcal{L}_{\mathrm{P}}\left[N_i^{\mathrm{obs}} | N_i^{\mathrm{bg}}\right]. \tag{4.8}$$

Here, $\mathcal{L}_{\mathrm{P}}(N_i|M_i)$ is the Poisson likelihood of a sample N_i of a multivariate Poisson with mean M_i, defined as the event rate in each energy bin. The profile likelihood test statistic is then calculated as

$$\lambda \equiv 2\left[\max_{\{\bar{\sigma}_e, N_i^{\mathrm{bg}}\}} \ell_{\mathrm{DM}} - \max_{\{N_i^{\mathrm{bg}}\}} \ell_{\mathrm{bg}}\right], \tag{4.9}$$

with the $\bar{\sigma}_e$ as the only signal model parameter. The statistic is then maximized over the possible mean background rate vectors N_i^{bg}. For the background-only hypothesis, it should be noted that l_{bg} is always maximized by $N_i^{\mathrm{bg}} = N_i^{\mathrm{obs}}$. The defined test statistic λ is evaluated following Wilk's theorem as a χ^2-distributed random variable with one-degree of freedom ($\bar{\sigma}_e$). A parameter point is hence excluded if it lies above the 95 % quantile, corresponding to a Confidence Level (C.L.) of 95 %, equaling $\lambda > 2.71$ for a one-sided confidence interval. This procedure yields constraints on the DM-electron scattering parameter space for the light and heavy mediator limits, for a range of light DM masses.

4.4 Results and Discussion

In this section, the constraints on the DM-electron scattering parameter space derived in the previous section are considered. For their discussion and interpretation it is important to view them in the light of existing constraints based on other earth-based DM searches. These so-called terrestrial constraints are based on limits imposed by the SENSEI [107], SuperCDMS [108], DAMIC [109], DarkSide [110], and Xenon-based [111, 112] experiments. Figure 4.10 shows the constraints imposed by the TES D detector and preliminary constraints imposed by TES F, with *loose*, *tight* and *systematic* cutting schemes for both the light

(massles) and heavy (10 GeV) mediator case. The mentioned existing terrestrial constraints are shown in gray, for now without the constraints imposed by SNSPDs. Differences between

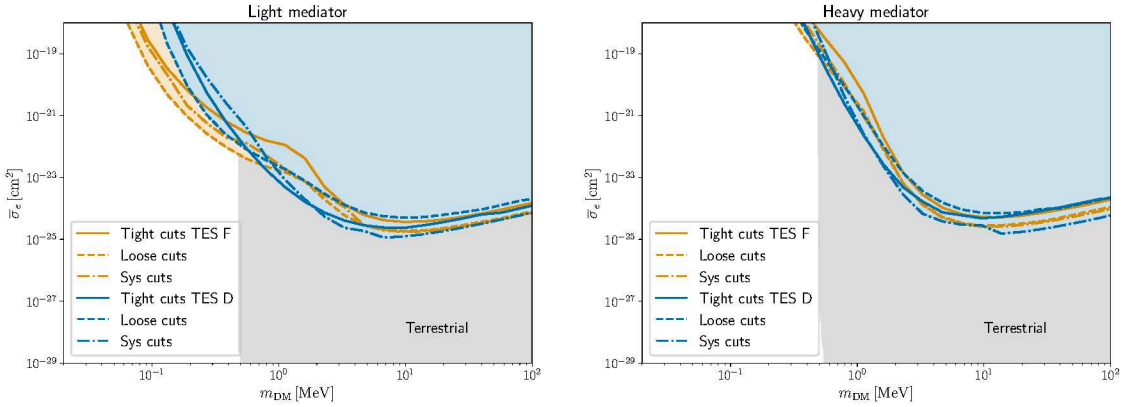

(a) (b)

Fig. 4.10.: DM-electron scattering constraints at 95 % C.L. imposed by the DM search performed with TES D and F (preliminary) based on *loose*, *tight* and *systematic* cuts in the (a) light and (b) heavy mediator limits. The constraints are compared to existing terrestrial constraints. These do not include the constraints imposed by SNSPDs used for DM searches.

the different cutting schemes are visible, but do not heavily impact the overall sensitivity, especially for the heavy mediator case. For the light mediator case and both modules, the *systematic* cuts are dominant at higher DM masses, since more of the background is filtered, mitigating the overall smaller acceptance of the *systematic* cuts. For lower masses, *loose* cuts are the most sensitive, since the acceptance for lower energies is very small in the other cases. This has again less impact on the heavy mediator case, where the cuts have an overall similar performance for both modules. The preliminary TES F constraints surpass the sensitivity of TES D for the light mediator for DM masses below 0.7 MeV, which can be attributed to the higher trigger acceptance for lower energies (see Tab. G.4).

As already mentioned in Ch. 1, advancements were made in developing dedicated SNSPD-based DM searches. With a low energy threshold down to 0.11 eV, a second generation SNSPD experiment (see Ref. [56]) surpasses both the TES and first generation SNSPD limits for both the light and heavy mediator, respectively. As this work is a first proposal and proof-of-principle of employing TES for light DM searches, it is not yet able to surpass the performance of dedicated detector designs. However, future scenarios of specifically optimized detection setups can be compared to the most recent exclusion limits as well. The improvement from first to second generation SNSPD searches demonstrates impressive room for improvement in sensitivity with dedicated optimization efforts, even for small scale searches. These improvements are mainly based on a larger active detector area (600 µm × 600 µm compared to 400 µm × 400 µm) and lower energy threshold (0.11 eV compared to 0.73 eV) of the second-generation device, requiring dedicated nanofabrication. The same is expected for TES technology. Two different cases are considered, both able

to represent steps towards large scale TES DM detection efforts. The tiny detection volume is one of the biggest obstacles for increasing the sensitivity to lower scattering rates. Increasing the size of the TES chip however, leads to an increase in noise levels and would reduce its sensitivity to lower energies. Thus, enlarging the volume while preserving the TES advantages, can only be achieved by large multiplexed TES-arrays. Advances in multiplexing technologies and employing a sophisticated Kinetic Inductance Current Sensor (KICS) readout will enable multiplexing many TES chips without losing sensitivity or energy resolution [113]. In addition, the energy resolution of optical TES chips is improving significantly over the last years and will improve further in the years to come [114]. Together with the optimization of TES chip design for ever lower energies, via optimization of (TES) absorber materials, this will open up sensitivity to lower DM masses as well. Therefore, two future devices based on such TES-arrays are considered and their sensitivity is predicted, by assuming the same volume and single-chip dimensions as the ones used in this thesis. The configurations used for the predicted sensitivities are listed in Tab. 4.8. The 16-pixel array

device	**exposure**	**threshold**	**background**
16-pixel array	1 year	same as TES D	scaled from TES D (loose cuts)
1000-pixel array	1 year	$\sim 70\,\mathrm{meV}$	none

Tab. 4.8.: Suggestions for future TES-based light DM searches employing detection systems based on multiplexed TES arrays.

device, is the most conservative prospect following already existing design proposals for multiplexed TES-arrays based on KICS readout instead of SQUIDs [115]. These multiplexed KICS already show comparable noise levels with regular SQUID readouts and therefore pose a promising alternative for low-noise detection schemes. Hence, such a device can already be imagined using a similar threshold and background as the one measured with TES D. For the calculation of exclusion limits, the background measured with TES D is scaled directly to match the larger device and longer exposure time. The *loose* cut scenario is used as an example. Another realistic, but more ambitious, device can be imagined, incorporating 1000 TES pixels. For such a device, a lower energy threshold can be imagined as well, following the energy resolution of the TES detector reported in Ref. [114]. In addition, a zero background scenario is considered for this device, assuming improvement in background and noise mitigation, as well as identification. The future constraints imposed by such devices on the DM-electron scattering parameter space are shown in Fig. 4.11, together with the TES D (*loose* cuts) and F (*systematic* cuts) constraints as well as both first and second generation SNSPD limits. For the light mediator, the TES constraints are competitive with the first generation SNSPD constraints, surpassing their performance at lower masses. As a reminder, the first generation SNSPD measurement lasted 180 h assuming no background for an energy threshold of 0.73 eV. Due to the background-free supposition and larger active volume, the constraints are more sensitive to lower scattering

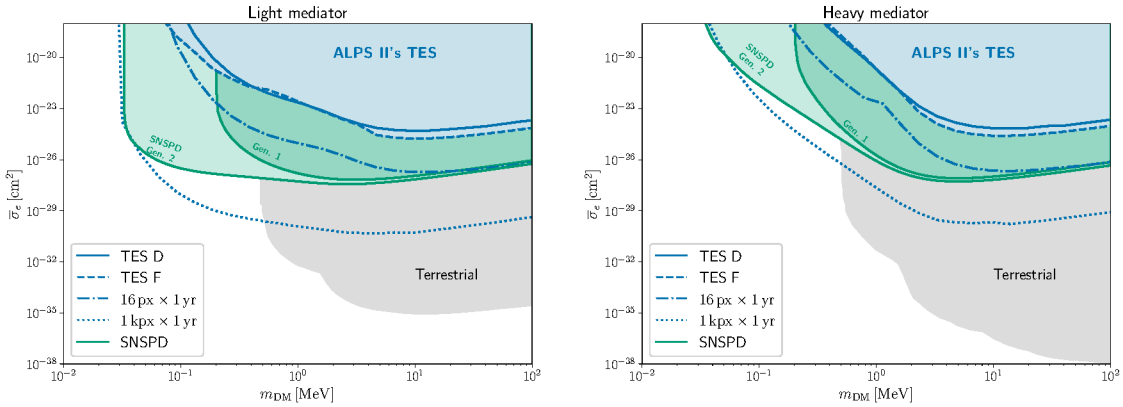

(a) (b)

Fig. 4.11.: DM-electron scattering constraints at 95 % C.L. imposed by different light DM searches in the (a) light and (b) heavy mediator limits. The limits are compared to existing terrestrial constraints. The limits shown for TES D are based on the *loose* cuts and the (preliminary) limits for TES F are based on the *systematic* cuts. Projections for future upgrades are shown with dot-dashed and dotted lines as well.

rates. However, the TES' sensitivity, even with reduced acceptance, to energies below this threshold enables sensitivity to lower masses in the sub-MeV range. This effect is less relevant for heavier mediators in the region of interest.

While the 16-pixel device does improve the existing limits mainly due to an increase in detection volume, more could probably be gained by sensitivity down to lower energy depositions with sufficient acceptance. However, increased area and background mitigation push the limits for the 1000-pixel array far into the existing terrestrial constraints and beyond existing constraints for sub-MeV DM masses. When considering future devices, these should aim for a competitive architecture addressing these technological limits.

In addition, all results shown in Fig. 4.10 and 4.11 need to be considered carefully, keeping overburden effects in mind. Overburden effects arise from obstacles between the DM particle's path and the DM detector. These obstacles include the reduction of the DM number density through atmospheric scattering, as well as shielding by, e.g., concrete. Considering the TES detector is placed underground and inside a cryostat consisting of multiple shielding stages, these effects may be significant for cross-sections $\bar{\sigma}_e \gtrsim 10^{-24}\,\mathrm{cm}^{-2}$ (see Ref. [116, 117]). This again highlights the importance of further exploring dedicated TES-arrays, which can improve the sensitivity to lower cross-sections, where overburden effects are reduced.

In direct comparison, the energy-resolving capabilities and sensitivity to small energy depositions of the TES enable the sensitivity to lower DM masses than the first generation SNSPD device. Since the TES acts as a microcalorimeter, it does not have an inherent energy threshold comparable to the SNSPDs, but is rather limited by the magnitude of baseline noise at the readout. Due to a smaller area and more dark counts compared to the

SNSPDs, the TES detector is not able to significantly gain sensitivity over them. However, without energy resolution SNSPDs can only set limits on the DM parameter space, but cannot necessarily discover DM. Energy-resolving detectors such as the TES will be needed to record and detect energy spectra resulting from DM interactions and therefore enable discovery. Hence, TES are promising DM detectors for DM-electron scattering.

However, while TES detectors are best suited for DM-electron scattering, they are also sensitive to further DM detection channels. The sensitivity to DM absorption and DM-nucleon scattering, including exclusion limits, is discussed in the next chapter.

5 Additional Dark Matter Interactions

The focus of this thesis lies on the interaction of DM particles with the TES detectors via DM-electron scattering. Exploring the respective parameter space is therefore the main objective. However, with the same measurements performed for this purpose, it is also possible to investigate other DM interaction mechanisms using the same TES data sets. Next to the scattering of DM with electrons, the absorption of kinetically-mixed dark photon DM on electrons in the TES can be explored as well. Recently, a new proposal also revealed possibilities of exploring DM-nucleon interactions with detectors optimized for DM-electron scattering [118].

Therefore, further DM interactions with the TES detector can be considered beyond DM-electron scattering and subsequently used to place constraints on the respective DM parameter space as well. This chapter will shortly circumscribe these options for the TES detectors and present constraints to the DM parameter space based on these effects. Section 5.1 will consider the electronic absorption of dark photons and Section 5.2 the effect of DM-nucleon interactions in the TES detectors. Finally, Section 5.3 will present exclusion limits and discuss the results in the context of adjacent DM searches.

This chapter represents an overview describing the steps to calculate constraints, based on Ref. [104, 105, 119], for the given DM interactions. Further details on the calculations regarding absorption can be found in Ref. [55, 84] and additional details on the nucleon scattering are found in Ref. [118].

5.1 Dark Matter Absorption

Beyond scattering of DM particles off electrons, the TES is also able to interact via the electron system in a different manner. The rule-of-thumb (see Eq. 1.1) for the comparison of energy and mass scales for DM-electron scattering introduced in Sec. 1.2 can be adjusted for absorption as well. When comparing these scales as in Fig.1.2, the DM mass m_{DM} matches the deposited energy E_D in this case. The described formalism follows Ref. [55]. A dark photon mediator A' is kinetically mixed with the SM photon. Similar to the cross-section in scattering experiments, constraints can be set on the coupling constant κ, which is the kinetic mixing parameter, referring to the kinetic mixing between the field strength tensor

of the photon $F_{\mu\nu}$ and the dark photon $F'_{\mu\nu}$. These field strengths are defined by the (dark) photon field $A^{(\prime)\mu}$ as

$$F^{(\prime)}_{\mu\nu} \equiv \partial_\mu A^{(\prime)}_\nu - \partial_\nu A^{(\prime)}_\mu. \tag{5.1}$$

The Lagrangian describing the interaction between the dark and SM photon is described as

$$\mathcal{L}_{\text{int}} = -\frac{1}{2}\kappa F_{\mu\nu} F'^{\mu\nu}. \tag{5.2}$$

The resulting absorption rate Γ_{A} depending on the kinetic mixing parameter, can then be calculated using the loss function in Eq. 1.31:

$$\Gamma_{\text{A}} = \kappa^2 m_{\text{DM}} \,\text{Im}\left(-\frac{1}{\epsilon(m_{\text{DM}}\mathbf{v}_{\text{DM}},\, m_{\text{DM}})}\right). \tag{5.3}$$

The calculation of constraints on the parameter space follows the exclusion limit calculation in Sec. 4.3, where the kinetic mixing parameter κ replaces the scattering cross section $\bar{\sigma}_e$ as the free parameter in Eq. 4.9. The loss function (see Eq. 1.31) depends on the DM's momentum defined by its velocity. Using the same velocity as in the halo model of Tab. 4.7, it can be approximated to $|\mathbf{v}_{\text{DM}}| \sim 10^{-3}$ in natural units. It follows that the momentum transfer is much smaller than the DM mass: $m_{\text{DM}}|\mathbf{v}_{\text{DM}}| \ll m_{\text{DM}}$. Therefore, the dielectric function ϵ is evaluated in the long wavelength limit, where the momentum transfer approaches zero: $\mathbf{q} \to 0$. The calculated constraints based on this interaction are shown and compared with other experiments in Sec. 5.3.

5.2 Dark Matter-Nucleon Scattering

Even beyond the module's sensitivities to DM-electron scattering and absorption, the DM search data can be used to set limits on the nucleon scattering parameter space, as well. Originally, DM-nucleon scattering is not an interaction known to be accessible by superconductors. The majority of the experimental landscape relies on liquid cryogenic targets based on liquid Xenon or Argon, or semiconductors such as Germanium or Silicon. While these experiments can be used to probe DM-electron scattering, too [45], it was, vice-versa, recently proposed that DM-electron scattering experiments could probe DM-nucleon scattering, as well [118]. DM can interact with nuclei via different processes, including the interaction with singular or multiple phonons. The description in this section follows the elastic nuclear recoil approach in Ref. [118]. A DM particle could scatter on a nucleon instead, leading to the same calorimetric output as with DM-electron scattering. The scattering rate follows Eq. 1.39, where the dynamic structure factor is adjusted for elastic nuclear recoils (following Ref. [87]). The dynamic structure factor describes the target's

response, for nuclei taking into account the atomic mass number $A_N (= \frac{m_N}{\mathrm{u}} \approx 183.85)$ for W, defined by the atomic mass m_N. For this case, the nuclear form factor $F_N(\mathbf{q})$ needs to be introduced, for which the Helm form factor [120] is used:

$$F_N(|\mathbf{q}|) = \frac{3j_1(|\mathbf{q}|r_N)}{(|\mathbf{q}|r_N)} e^{-(|\mathbf{q}|s)^2/2} \tag{5.4}$$

where j_1 is the spherical Bessel function of the first kind and uses the nuclear skin thickness $s = 0.9\,\mathrm{fm}$ and the effective nuclear radius $r_N \approx A_N^{1/3} \times 1.14\,\mathrm{fm}$. The structure factor for nuclear elastic scattering is then defined as:

$$S(\mathbf{q}, \omega) = \frac{2\pi\rho_\mathrm{T}}{\sum_N A_N} \sum_N \frac{A_N^3}{m_N} F_N(\mathbf{q})^2 \delta\left(\omega - \frac{\mathbf{q}^2}{2m_N}\right). \tag{5.5}$$

For the form factor used for spin-independent interactions introduced for the event rate in Eq. 1.40, the reference momentum for nuclear scattering is $q_{0,n} \equiv m_\mathrm{DM} \langle \mathbf{v}_\mathrm{DM} \rangle$. Just as for the electron scattering case, the event rate function is then evaluated with the scattering cross section σ_n as a free parameter, following the calculations in Sec. 4.3. The results are discussed and compared with other experiments in Sec. 5.3.

5.3 Results and Discussion

Following the calculations outlined in Sec. 5.1 and 5.2, constraints can be set on the respective parameter space similar to the exclusion limits on DM-electron scattering set in Ch. 4. Projections based on larger TES-arrays are considered for these cases of dark photon electronic absorption and DM-nucleon scattering as well. Furthermore, the results are compared, where applicable, to the two generations of SNSPD devices.

For the case of electronic absorption already existing terrestrial constraints need to be taken into account. For dark photons, these also include further constraints, among others [121], based on results from FUNK [122], SuperCDMS [123] and EDELWEISS [124] experiments. In addition, model-dependent stellar constraints, e.g., from the sun, horizontal branch, and red giant stars, need to be considered [121, 125]. The results for constraints on the absorption of a kinetically-mixed dark photon are demonstrated in Fig. 5.1. While the limits imposed on the DM-electron scattering parameter space are mostly smooth over the mass range for the *loose*, *tight* and *systematic* cuts, they show sharp edges and zigzag shapes for the absorption. This is due to an increased influence of the background spectrum on the TES limits compared to DM-electron scattering. The zigzag shape arises, because the expected absorption rate for a certain energy corresponds directly to the DM mass. For each DM mass, the expected absorption rate is therefore a narrow spike, as opposed to a smooth spectrum. When comparing the cutting schemes with each other, similar to

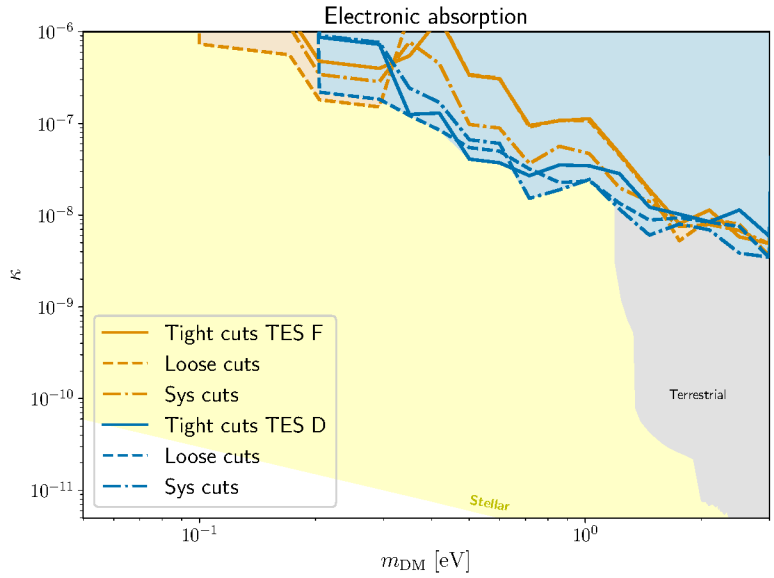

Fig. 5.1.: Electronic absorption of dark photon DM. TES limits and projections at 95 % C.L. imposed by a DM search performed with TES D and F (preliminary) based on *loose*, *tight* and *systematic* cuts. The constraints are compared to existing terrestrial limits in gray and model-dependent stellar constraints in yellow. This does not include the constraints imposed by SNSPDs used for DM searches.

electron scattering, the *loose* cuts are able to set lower constraints at low masses compared to the *tight* and *systematic* cuts based on their cuts' low acceptance at lower energies. The preliminary results for TES F are able to extend the sensitivity to lower mass ranges compared to TES D, due to the higher acceptance for lower energy depositions. However, TES D is more sensitive to lower kinetic mixing parameters κ for the remaining covered parameter space. This arises from the lower background rate measured with TES D, compared to TES F. Naturally, these results can be compared to the two generations of SNSPDs, too. Figure 5.2 shows the *loose* cut constraints for TES D, *systematic* cut constraints for TES F, SNSPD limits, as well as projections for future TES arrays.

The results based on the depicted TES modules do not surpass the exclusion limits set by the second generation SNSPDs and especially show less sensitivity to the coupling constant. However, the 1 kpx array would be able to decrease their limits by about two orders of magnitude, considering the sensitivity to the coupling parameter. It is important to note, that none of these experiments or proposals are able to exceed the stellar constraints, which are nevertheless model-dependent. The TES results' zigzag shape is not present for the SNSPD limits, where zero background is assumed. Reducing the background, as shown with the 1 kpx array, where zero signal and background is assumed as well, is therefore a very powerful approach to increase sensitivity for smaller mixing parameters. When comparing these measurements with the projections of a similar setup with 16 pixels (and scaling the background) the projection only significantly gains over the current configuration for both lower and higher masses. This follows the relatively high background shown in the energy

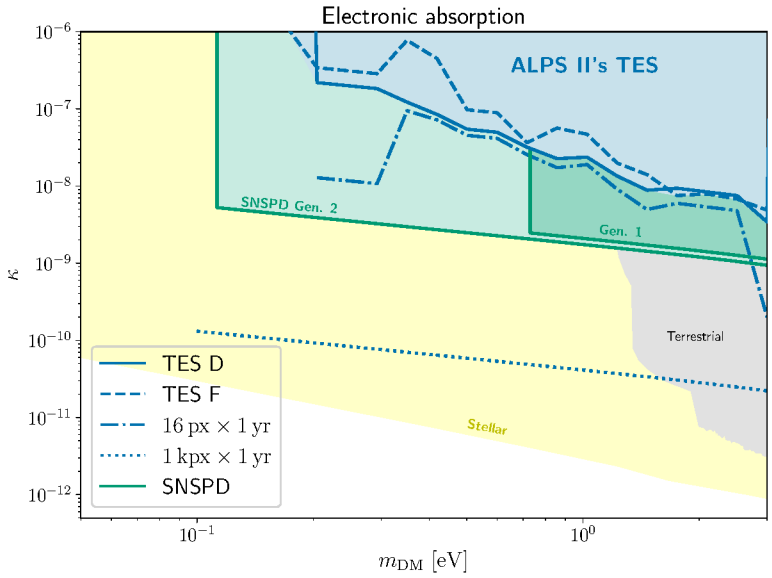

Fig. 5.2.: Electronic absorption of dark photon DM. TES limits and projections at 95 % C.L. imposed by a DM search performed with TES D and F. The limits shown for TES D are based on the *loose* cuts and the (preliminary) limits for TES F are based on the *systematic* cuts. The constraints are compared to existing terrestrial limits and constraints imposed by the first and second generations of SNSPDs used for DM searches, as well as projections based on the TES results. In yellow, model-dependent stellar constraints are depicted as well. Projections for future upgrades are shown with dot-dashed and dotted lines as well.

spectrum in Fig. 4.9 (b) and (d) in the range from 0.5 eV to 1.0 eV. Hence, this effect also arises due to the scaling from the TES D background for the 16 kpx projection, where no dark counts were observed below 0.3 eV. Due to the nature of the expected absorption rate, the higher backgrounds limit the constraints in the corresponding mass range. On the contrary, as a smooth recoil spectrum is expected for scattering experiments, the difference in shape to the measured energy spectrum aids in the background mitigation.

This fact can be exploited when considering DM-nucleon scattering, as well. In this case, other existing terrestrial constraints have to be considered, namely arising from the Migdal effect [126] and constraints based on other elastic scattering experiments. The Migdal effect describes the excitation or ionization of nuclear electrons, after a nuclear scattering event [127, 128]. This excitation (ionization) arises from the time lag introduced by displacement of the nucleus through the scattering process, which the electrons are not instantly following. Therefore, these secondary processes can also increase the sensitivity of DM-nucleon scattering experiments (e.g. semiconductors or liquid targets) to even lower masses, where nuclear recoil signals are too small to be measured. While the Migdal effect has not been directly observed yet, ongoing experimental efforts such as the MIGDAL experiment are underway and aim for a first direct observation [129]. Even so, analyses exploring DM search data based on electronic signals for the Migdal effect, can already

set preliminary constraints on the DM-nucleon scattering parameter space. Among others, the constraints for using both effects include results from EDELWEISS [28, 130], the DarkSide-50 experiment [131, 132], SuperCDMS [24, 133], CRESST [36], SENSEI [134], PandaX [135] and LUX [31]. The results for constraints on the elastic scattering of DM off nucleons are demonstrated in Fig. 5.3. Naturally, compared to electron scattering, nuclear

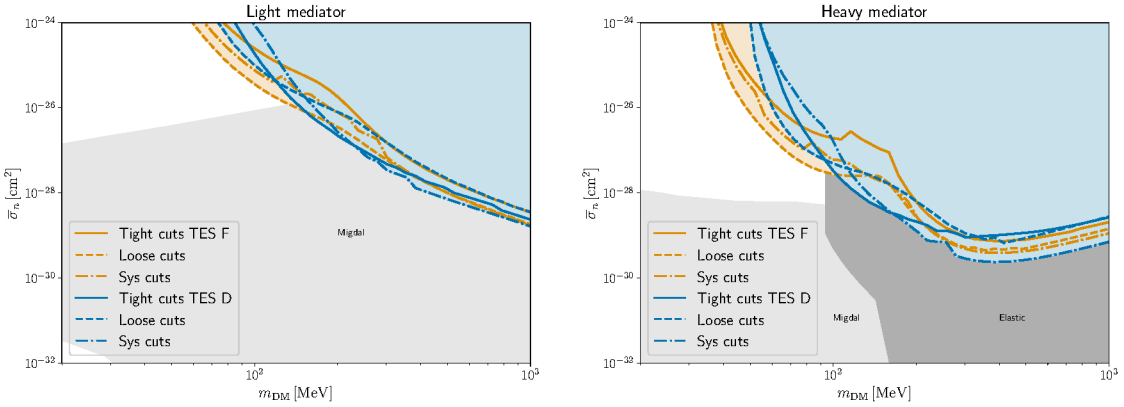

(a) (b)

Fig. 5.3.: DM-nucleon scattering constraints at 95 % C.L. imposed by DM searches in the (a) light and (b) heavy mediator limits. The limits imposed by the DM search performed with TES D and F (preliminary) are based on *loose*, *tight* and *systematic* cuts. The constraints are compared to existing elastic nuclear scattering limits denoted as *elastic* and constraints based on the Migdal effect. These do not include the constraints imposed by SNSPDs used for DM searches.

scattering investigates higher DM masses. The results of both TES modules with *tight*, *loose* and *systematic* cuts, respectively, are in comparison somewhat similar to those of DM-electron scattering shown in Fig. 4.10. While the *loose* cuts are able to exclude more parameter space for lower masses, the high background around 1 eV for the *loose* cuts leads to a better performance of the *tight* and *systematic* cuts in the masses' mid-range. While for the light mediator it is mostly the Migdal effect posing similar constraints, additional limits from elastic scattering need to be considered for the heavy mediator as well.

The *loose* cut results for TES D and *systematic* cuts for TES F are compared to the second generation SNSPD results[1], as well as the TES-array projections for the light and heavy mediator case in Fig. 5.4. The constraints imposed by the second generation SNSPD experiment reach about two orders of magnitude lower than the TES limits. The 16 pixel projection could improve over the SNSPD limits at higher masses, where elastic scattering constraints exist already. The 1 kpx array projection shows a large improvement compared to the SNSPD limits, and would be able to improve the sensitivity to the DM-nucleon cross-section by about four orders of magnitude. However, even so, the sensitivity would not surpass limits set by the Migdal effect so far. Again, it should be mentioned that overburden effects might become relevant above 10^{-25} cm^2 for DM-nucleon scattering.

[1]No published DM-nucleon scattering limits are available for the first generation SNSPD experiment.

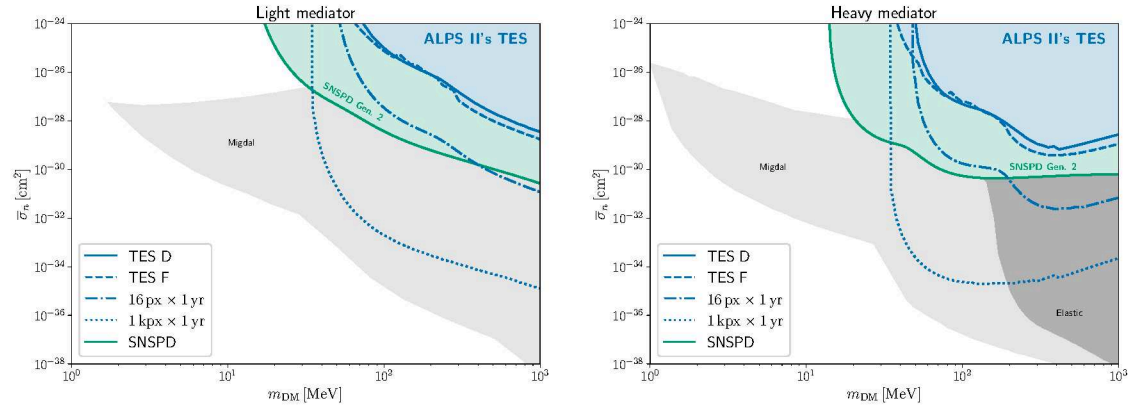

(a) (b)

Fig. 5.4.: DM-nucleon scattering constraints at 95 % C.L. imposed by different DM searches in the (a) light and (b) heavy mediator limits. The limits imposed by the DM search performed with TES D are based on the *loose* cuts and the (preliminary) limits for TES F are based on the *systematic* cuts. The constraints are compared to existing elastic nuclear scattering limits denoted as *elastic*, constraints based on the Migdal effect, and constraints imposed by the second generation of SNSPDs used for DM searches, as well as projections based on the TES results. Projections for future upgrades are shown with dot-dashed and dotted lines as well.

Nonetheless, even when currently not reaching into new parameter space, the theoretical sensitivity to additional DM interactions exemplify the strength and possibilities for using superconductors and specifically TES for direct DM experiments and possibly beyond. Sensitivity to unexplored regions in the parameter spaces could be specifically realized by even larger TES arrays for the absorption and sensitivity to even lower energies for the nucleon-scattering case.

6 Conclusion and Outlook

The identification and detection of Dark Matter (DM) presents one of the biggest challenges in modern physics. For decades, ever-larger experiments have been aiming to detect and investigate DM particles in earth- and space-based experiments. In the next years, a majority of the GeV-mass DM-nucleon scattering parameter space will have been explored down to the so-called neutrino fog, where neutrino interactions dominate. These experiments search for DM-nucleon scattering signatures, using large target volumes paired with sensors to measure possible interactions. If these experiments are unsuccessful in finding DM signatures in this mass range, other regions must be explored. The focus of many experimental efforts currently shifts to lower DM mass ranges with light DM or ultra-light axions as prime candidates.

As DM-nucleon scattering loses sensitivity with reduced DM mass, DM-electron scattering becomes accessible. Based on similar experiments conducted using superconductors such as the Superconducting Nanowire Single Photon Detector (SNSPD), a Transition Edge Sensor (TES) was used to explore MeV and even sub-MeV DM masses. The Any Light Particle Search II (ALPS II) experiment is currently developing such a TES system as a low-flux photon detector. These TESs, most commonly employed as single photon detectors, are sensitive microcalorimeters based on a superconducting chip operated in its transition region, read out via a Superconducting Quantum Interference Device (SQUID) chip. Within the scope of this work, the applications of ALPS II's TES detection system for direct DM searches has been considered. In contrast to the majority of DM-nucleon scattering experiments, where TES are already employed as sensors attached to larger target volumes, this work proposes and employs the TES as both target and sensor simultaneously. This has not been attempted in another context, so far. As such, the TES detection system is sensitive to deposited energies down to below 1 eV induced by DM-electron scattering, where resulting energy depositions are expected to resemble signals originating from single photons. Compared to SNSPDs, functioning as counting detectors, the energy resolving capabilities of the TES enables the investigation of resulting energy spectra, which aids in background mitigation.

In order to perform a proof-of-principle measurement using ALPS II's TES system, certain requirements need to be met. This includes sufficient sensitivity to low energy depositions, since this increases the sensitivity to DM of lower masses. At the same time, the background and noise levels need to be as low as possible. Furthermore, a linear response to energy depositions in the sensor's sensitive region will enable the determination of energy spectra

resulting from possible signals. Therefore, the system's energy response is investigated using lasers of different wavelengths from 0.76 eV to 1.41 eV. Based on these measurements and theoretical expectations, the integral of a photon-like signal pulse is linearly dependent on the deposited energy, while the rise and decay time of the signal pulses are approximately constant over the same energy range. This is investigated using dedicated fit functions for the photon pulse shape. This relation enables the identification of signals based on energy depositions in the sensitive TES, such as those originating from DM or photon interactions. During this preparation, different noise sources are investigated as well, where the baseline noise is the limiting factor in setting a low trigger level, capable of detecting lower energies. Other background sources such as cosmic rays or radioactive trace materials, can be discarded based on the signal shape. A direct DM search has been prepared and performed with ALPS II's TES detection system using a TES module dedicated for single-photon detection in ALPS II. Based on the analysis of this module, a preliminary study is performed with an additional module, as well. This module includes modifications aiming for a reduced background in dedicated DM searches. The electronic and Data Acquisition (DAQ) setup of each module is optimized for a high signal-to-noise ratio and good energy resolution to enable proper discrimination between triggered pulses from energy depositions and noise.

Dedicated DM searches of > 400 h have been performed using low trigger levels with both modules. Dedicated simulations investigate the trigger and analysis acceptance regarding signal pulses of a broad spectrum of energies from 0.1 eV to 3.0 eV. Together with further calibration datasets based on single photons (from lasers), these simulations are used to select cut regions to identify photon-like pulses, based on fit parameters such as the rise and decay time of the signal pulses. These different cutting schemes are used on the fitted DM search datasets, cutting away everything outside of the regions of interest. Based on the pulse shape of the calibration laser pulses, the resulting pulse integral distributions can be translated to an energy spectrum representing photon-like signals surviving the cut selections. These energy spectra are compared with expected DM signal model rates, however do not resemble their shape, even when taking into account the energy-dependent acceptance of the detection systems and analyses. Therefore, while no DM is found in the resulting background spectrum, it can still be used to place constraints on the mass-dependent DM-electron scattering cross-section. Using a profile-likelihood test, the parameter space can be constrained for different scattering cross-sections at 95 % confidence level. For this approach, the case where part of the measured energy spectrum could originate from DM is compared to the case where all of it is background. Based on these calculations, competitive limits can be set on the DM-electron scattering parameter space for both the light and heavy mediator limit with the ALPS II device, including a preliminary prediction of limits for the adjusted second TES module. The signal and noise properties of the second device differs significantly from the ALPS II module, but shows promise already with the off-the-shelf analysis based on the latter. Data taking and analysis, especially considering the pulse

finding algorithm, regarding the second device in additional DM search measurements will be optimized elsewhere. Compared with a first generation of SNSPD experiments, the TES modules exceed the limits for all cutting schemes in the light mediator limit in the lower mass range. However, an optimized second generation of SNSPDs enhances the sensitivity from the first generation by almost an order of magnitude, therefore bypassing our first generation TES limits as well. This improvement demonstrates the power of enhancement through an upgraded detection system and motivates calculating projected constraints for future generations of TES detection systems as well. The measured constraints are therefore compared with similar devices based on a 16 and 1000 pixel TES array as well, motivated by already existing and recently proposed configurations for multiplexed TES devices. Especially the 1000 pixel array is able to surpass the second generation SNSPD experiment for lower scattering cross-sections, as well.

Even beyond DM-electron scattering, the modules can be used for other DM searches as well, namely dark photon absorption and DM-nucleon scattering. Similarly to the results for DM-electron scattering, the first generation TES modules used in this work are not able to surpass limits set by second generation SNSPD detectors, could however set new constraints when considering future multiplexed devices as well.

At the current sensitivity of the superconducting experiments based on TESs and SNSPDs, standard cosmological DM models, such as those arising from freeze-in production [136, 137], still require improved sensitivity by many orders of magnitude [53]. Nonetheless, the parameter space regions that could be investigated by future upgraded TES DM detectors, are feasible for DM models arising from different production mechanisms such as asymmetric DM [138], thermal relic DM in the form of strongly interacting massive particles (SIMPs) [43] or elastically decoupling relic (ELDER) DM [139, 140].

In addition to the improvements in volume and exposure introduced for the proposed TES arrays, which mainly enhances the sensitivity to the coupling parameters, enhancements in TES fabrication could improve sensitivity as well. In reducing the critical temperature of these devices further, sensitivity could be enhanced to even lower energies and therefor lower DM masses. Deeper underground placement, such as in well-shielded laboratories, could reduce backgrounds, though it may also further attenuate DM signals. Furthermore, dedicated background models could be explored, as well.

Even beyond these more general developments, small scale improvements could be employed to improve the sensitivity for direct DM searches of the used TES system. The sensitivity to lower masses is currently governed by the level of the DAQ trigger, where lower trigger levels enhance the sensitivity for lower DM masses. However, the position of the current triggers is limited by the measured rate, since the DAQ computer's buffer is overwhelmed at high rates, which can lead to dead time. Hence, the raw DM search data is dominated by

fast noise spikes arising at these lower trigger levels, which might originate from remaining electromagnetic interference. Possible solutions for this problem include:

- improvement of understanding of baseline noise with subsequent mitigation and reduction of fast noise spikes
- enable a higher trigger rate in an upgraded DAQ system without overwhelming the computer's buffer
- adjustment of the DAQ system to only save timelines with more than three traces below the set trigger threshold, to reduce the amount of fast noise spikes corrupting the data set

Furthermore, shifts in the noise baseline should be investigated in detail. Once the fast noise signals are under control, the remaining backgrounds should be reduced further to increase the sensitivity to possible DM signals. One approach is to reduce the amount of backgrounds arising from energy depositions in the Si substrate. Depositing the TES onto a SiN_x membrane instead, reduces the active material surrounding the chip and therefore the number of background signals. Apart from the modules considered in this work, an additional TES module including such a membrane is currently being assembled at PTB Berlin for use in further DM search measurements. Additionally, the understanding of the modules' energetic response currently extrapolated from a smaller energy range, could be enhanced by employing a more broadband calibration procedure, testing for the response at higher energies as well. For example, pulsed lasers of wavelengths λ could be employed, where the energy of n photons could be used for a larger number of calibration points of wavelength λ/n. Even beyond this another option could be to dissipate a well defined amount of energy into the TES via its bias line, to add a pulse on top of the bias current, which could mimic deposited energy. This might even enable a completely dark calibration, without the need of any fibers in the vicinity of the modules.

In conclusion, ALPS II's TES detection system was successfully employed as a first generation TES experiment for the direct detection of light DM. The limits set in the respective parameter spaces for different DM interactions are competitive with a similar first generation experiment based on SNSPDs. Improvements demonstrated by a second generation SNSPD device, motivate further research regarding enhanced TES detection systems with increased sensitivity. Since the beginning of this work, further developments concerning TES detectors in DM searches have been made, including similar proposals to the experiments described in this thesis or further adjacent light DM searches employing TES with superior energy resolution for light DM searches with separate targets [141, 142]. This emphasizes the timeliness and importance of advancing these searches further, and the proof-of-principle based on the actual measurements performed in this thesis could contribute to the onset of a new generation of earth-based DM detection experiments.

Appendices

A TES Modules Details

A.1 SQUID Wiring

The SQUIDs used on the modules TES D and TES F differ slightly from the SQUIDs used in previous works ([17, 18, 58]). While previous modules used two-stage SQUIDs, these used single-stage SQUIDs reducing, among other things, the set-up time of the SQUID electronics and improved measurement reliability. The wiring scheme needed between the module in the cold, including the TES, and the Lemo readout adapter in the warm is shown in Fig. A.1.

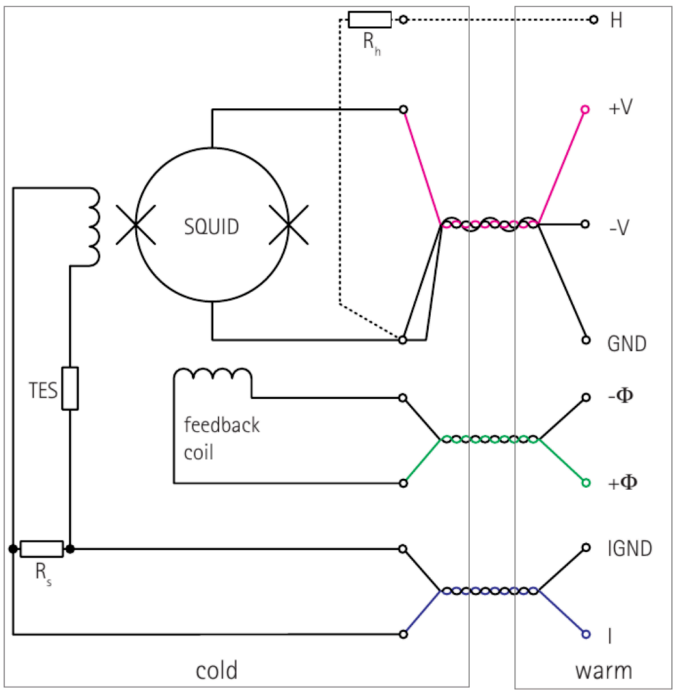

Fig. A.1.: The left part of the scheme shows the single-stage SQUID and TES in the cold connected via twisted wires to the warm parts outside of the cryostat. $\pm V$ are the voltage connections to the SQUID, while $\pm\Phi$ are the connections to the feedback coil, I is the output of the TES as a current source and IGND is the ground return of the TES. Image from Magnicon GmbH.

The circuit scheme used on the modules with single-stage SQUIDs is shown in Fig. A.2.

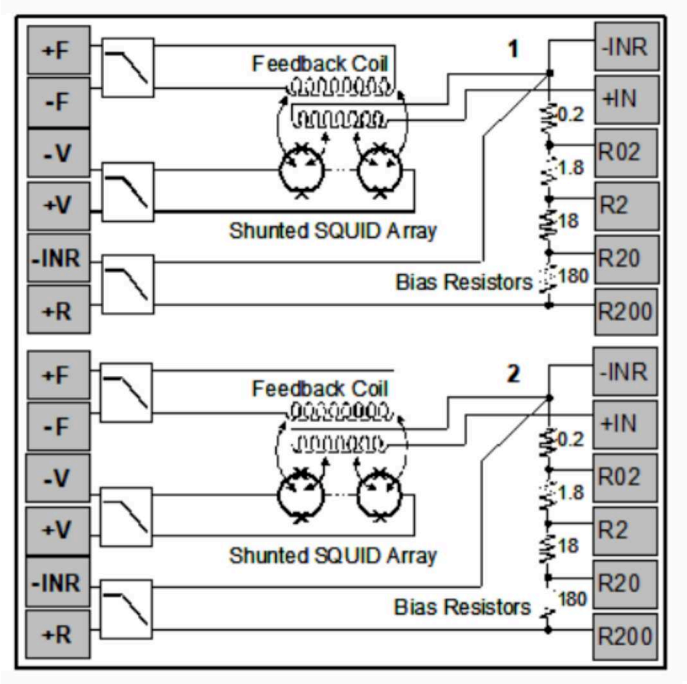

Fig. A.2.: Single-stage SQUID circuit for a SQUID chip with two channels as installed on modules TES D and F. The gray boxes represent the bonding pads of the chips and their respective circuit elements. The shunted SQUID array is inductively coupled to the feedback coil and the TES circuit's input coil. Image from PTB.

A.2 TES Modules

Different TES modules have been measured, tested, planned and assembled during the making of this thesis, which are listed in Tab. A.1.

Module	**TES chips & SQUIDs**	**Wiring**	**Information & Status**
UHH	2x2-stage SQUIDs (PTB) and 2x NIST 1064 nm optimized TES Chips	Micro sub-D connector	Borrowed from University of Hamburg (Horns Group) in October 2023; suboptimal SNR; returned in March 2024; should be used between 40 mK to 145 mK
A	2x2-stage SQUIDs (PTB) and 2x NIST 1064 nm optimized TES Chips	Curled copper wires with LEMO connectors	Heating issues; TES 1 & 2 broken; SQUIDs fine (tested at PTB)

Continued from previous page

Module	TES chips & SQUIDs	Wiring	Information & Status
B	2x2-stage SQUIDs (PTB) and 2x NIST 1064 nm optimized TES Chips	Curled copper wires, Micro sub-D connector, LEMO connectors	TES 1 & 2 broken; SQUIDs still fine (tested at PTB)
C	`X123L` 2x2-stage SQUIDs (PTB), 1x NIST 1064 nm optimized TES Chip, intermediate bonding pad	Micro sub-D connector, braided copper wire, LEMO adapter needed	Glasgow module; Channel B SQUID broken; Currently stored in the laboratory
D	`C638_I15_X16FL` single-stage SQUID, 2x NIST 1064 nm optimized TES Chips (H7 & H8), intermediate bonding pad	MWDM-25 socket	Channel A TES package moved in December 2024 — fixed by PTB in January 2025, currently installed in Cryostat B
E	`C7002_J34_X114HW` 2x2-stage SQUIDs, 2x NIST 1064 nm optimized TES Chip, intermediate bonding pad	MWDM-25 socket	Brass screw stuck in one mounting thread; stored in laboratory
F	`C646_I14_A_B` single-stage SQUID, 2x NIST 1064 nm optimized TES Chip (A6, B9)	MWDM-25 socket	Adjusted module with TES chip on copper cylinder and option for a copper cover instead of Zirconia sleeves; Stored in laboratory, currently only equips one TES chip (Channel A), as the other fell off (still intact)
G	2x `W221216` TES devices on SiN membranes	-	No optical stack; At PTB, awaiting assembly.

Tab. A.1.: Overview of TES Modules used or worked on within this thesis.

Except for E and G, all of the listed sensors have been tested and measured at some point during the making of this thesis. The borrowed UHH module and modules C-G have been organized during the making of this thesis, enhancing the amount of fallback

options if problems with TES modules arise. Modules have been made more reliable overall, by introducing a MWDM-25 socket for TES D onward, providing increased stability and lifetime of the readout cables. A DM search with TES D was performed in April 2024, and with TES F in February 2025.

B TES Calibration Setup

For the calibration setups, described in Sec. 2.4.2, different settings and components are needed for each laser wavelength. Table B.2 show the different lasers used in the calibration setups and their respective settings, as well as attenuation equipment used especially for the non fiber-coupled configuration. Note that no clean (i.e. without significant contribution of noise triggers) light samples could be recorded using the 2051 nm diode laser, which is still listed here for the sake of completeness. In order to record clean samples with as little outliers as possible, the trigger level was adjusted in each of these measurements to amount to about 75 % of the pulse height of an example pulse.

Laser	**Eblana** 2051 nm	**InPhenix** 1640 nm	**InPhenix** 1310 nm	**InPhenix** 880 nm
Energy	0.6 eV	0.75 eV	0.93 eV	1.41 eV
Power	2 mW	3 mW	1 mW	2 mW
Butterfly Diode	Type 2	Type 1	Type 1	Type 1
TEC Limit	1.2 A	1.2 A	1.5 A	1.5 A
Driver Current	350 mA	100 mA	300 mA	300 mA
Attenuation Equipment	V2000	V1550	V1550, FA15T-APC	VOA850-APC
Trigger-Levels TES D	/	−6 mV	−6 mV	−10 mV
Trigger-Levels TES F	/	−5.8 mV	−6 mV	−6 mV

Tab. B.2.: Overview of settings and equipment used for different calibration wavelengths for the calibration setup (non fiber-coupled).

For the 1064 nm laser, −9 mV was used as a trigger threshold for TES D and −7 mV for TES F during the full calibration.

C Optimization Results TES D

Continuing the optimization discussion of TES F in Sec. 3.2, this section shows the results of the optimization process regarding TES D. As for TES F, Fig. C.3 shows selected pulse shape parameters derived from the fitting analysis for different working points and GBWPs. Even clearer than for TES F, a GBWP of 2.8 GHz shows large deviations from the other

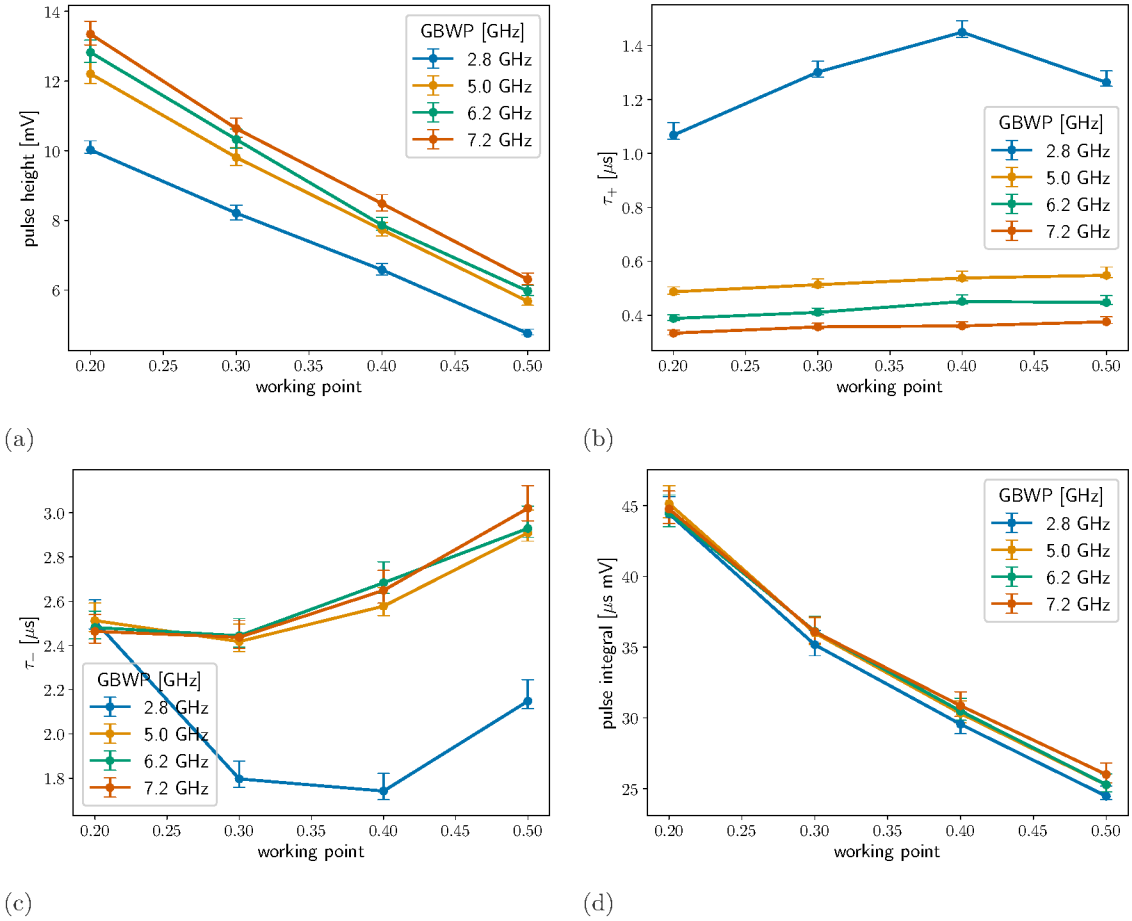

Fig. C.3.: Pulse shape parameters for different working points and GBWP configurations of TES D, namely (a) Pulse height (b) rise time τ_+ (c) decay time τ_- and (d) pulse integral.

GBWPs. With the exception of 2.8 GHz, the detector response for different working points is mostly stable for different GBWPs.

Similar to TES F, the energy resolution is degrading for higher working points as well, see Fig. C.4. The best energy resolution of $(7.09 \pm 0.16)\,\%$ is achieved for 2.8 GHz and $0.2 R_N$. Again, the pulse height parameter yields better results compared to the pulse integral parameter.

In addition, the SNR shows a similar behavior as well, shown in Fig. C.5. The SNR improves for lower working points, due to lower relative electronic noise level. Within its

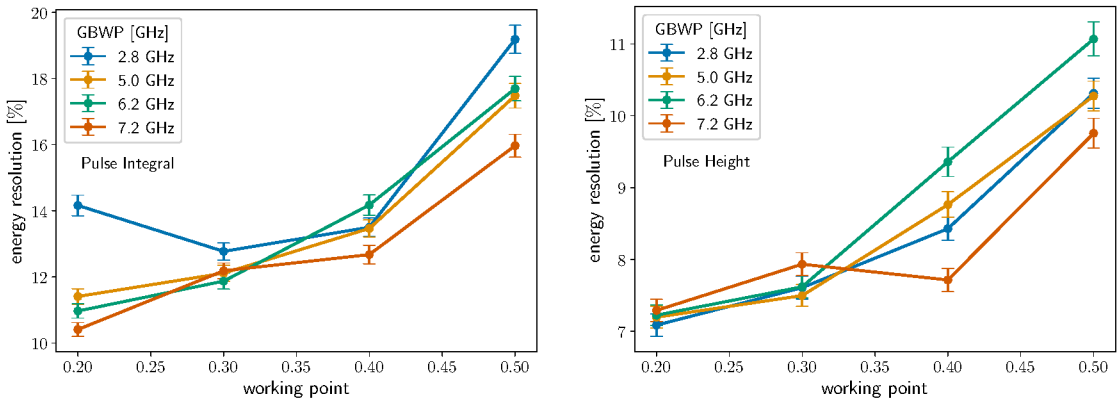

(a) (b)

Fig. C.4.: Energy resolution for different working points and GBWP configurations of TES D, determined using the (a) pulse integral and (b) pulse height parameters. The uncertainties originate from Gaussian error propagation based on the fitting uncertainties of the Gaussian functions.

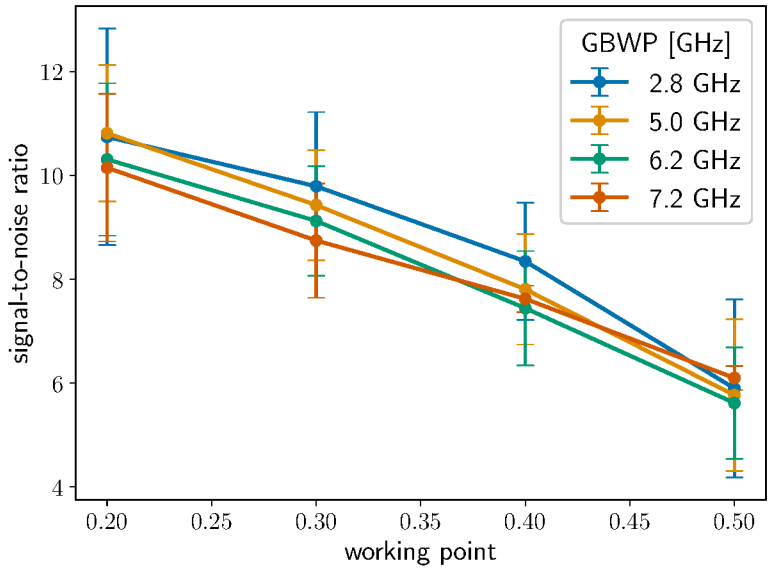

Fig. C.5.: SNR for different working points and GBWP configurations of TES D. The uncertainties originate from Gaussian error propagation.

uncertainties, it is independent from the GBWP.

Consequently, a working point of $0.2R_N$ yields the best results for both energy resolution and SNR with a comparably stable signal shape for different GBWPs. While the lowest GBWP yields very good energy resolution and SNR, the timing parameters of the pulse shape vary significantly for different GBWPs, possibly pointing toward non-linearity in the TES response. Additionally, higher GBWPs will simplify the cut-based analysis due to more concentrated fit parameter distributions [58]. Therefore, 5.0 GHz is chosen, also providing a good energy resolution of $(7.20 \pm 0.14)\,\%$ at $0.2R_N$.

D Calibration Results TES F

Continuing the calibration discussion of TES D in Sec. 3.2, this section shows the results of the optimization process regarding TES F. As for TES D, Fig. D.6 shows an increase of the pulse height for higher energies (lower wavelengths). Compared with the signal

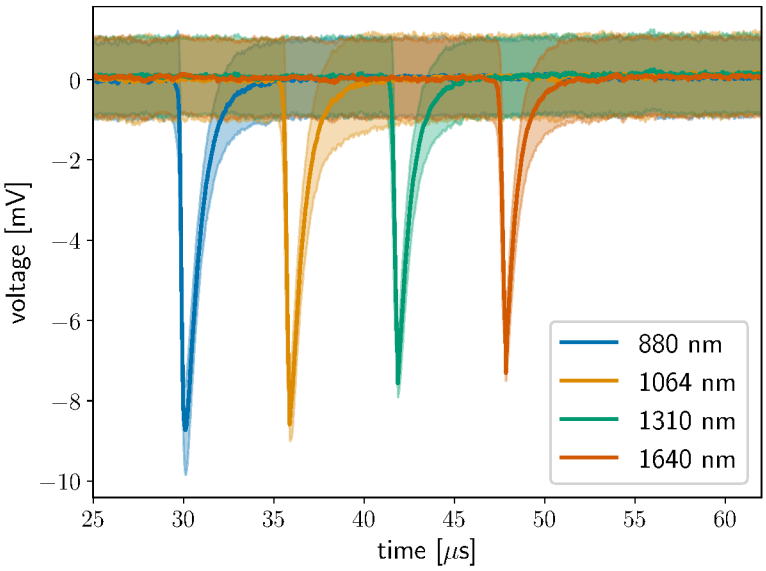

Fig. D.6.: Average pulses for different wavelengths, measured with the TES F module during calibration, including standard deviations. Measurement performed in the no-fiber calibration setup.

shape of the same wavelengths in Fig. 3.6 based on TES D, the signals have lower pulse height and appear much faster within the same time window. In addition, the fit parameter distributions shown in Fig. D.7, show a similar response to different energies as well. The rise and decay times are more localized (see Fig. D.8(b)), while the amplitude and pulse integral show an energy dependent shift of their distributions (see Fig. D.8(a)). Following the same approach as in TES D. The fit parameters of the respective linear fits are listed in Tab. D.3. In conclusion, TES F demonstrates a similar energy response as TES D, where

	m	b
amplitude	$(8.35 \pm 0.08)\,\frac{\mathrm{mV}}{\mathrm{eV}}$	$(4.16 \pm 0.08)\,\mathrm{mV}$
pulse integral	$(5.58 \pm 0.05)\,\frac{\mu\mathrm{s\,mV}}{\mathrm{eV}}$	$(2.66 \pm 0.05)\,\mu\mathrm{s\,mV}$

Tab. D.3.: Fit parameters based on TES F of the linear fit to the amplitude and pulse integral depending on the laser energy for the linear fit function: $y = mE + b$. See Fig. D.8.

the pulse integral (and amplitude), and rise and decay time are suitable parameters for energy calibration and event selection, respectively. The magnitude of these parameters is however shifted to lower values in comparison, resulting in smaller and faster signals.

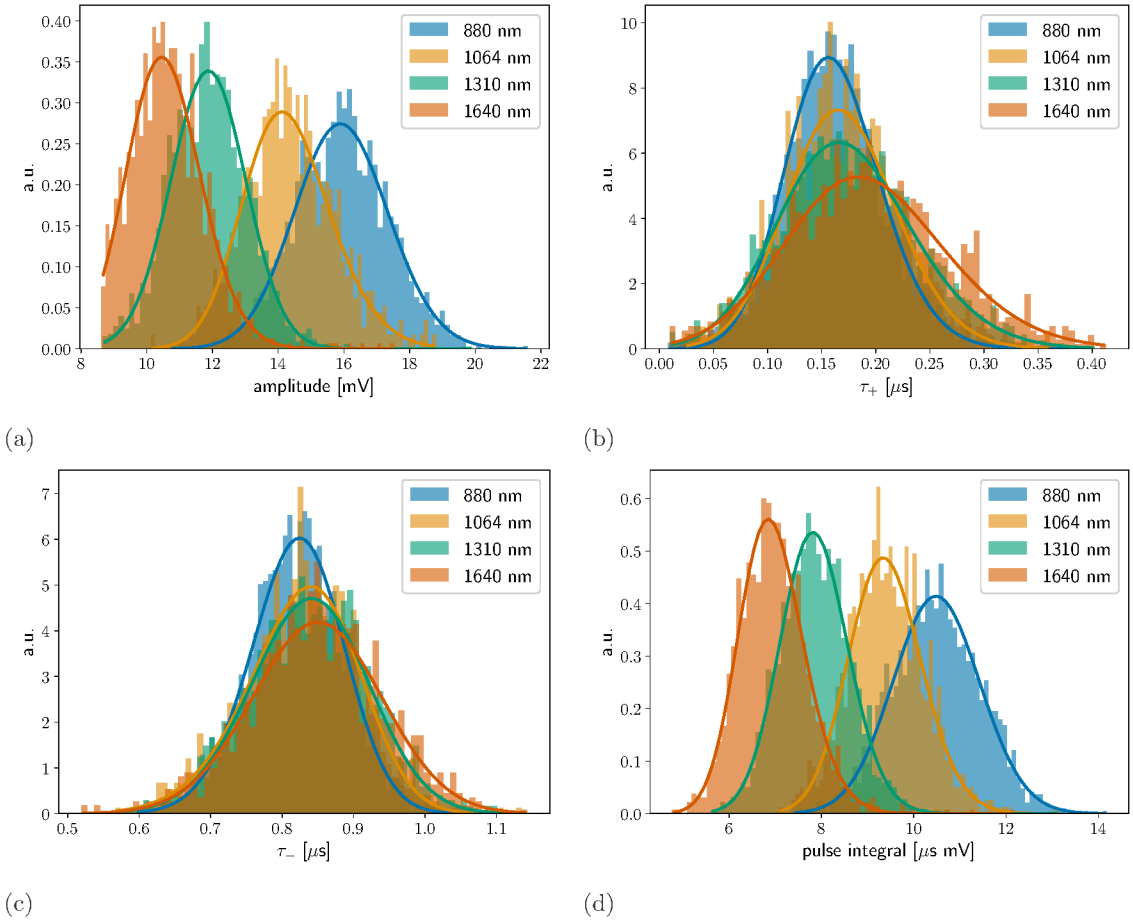

Fig. D.7.: Fitting parameters for photon pulses of different wavelengths measured with the TES F module during calibration (no-fiber calibration setup). Namely the normalized distributions of the (a) pulse amplitude (b) rise time τ_+ (c) decay time τ_- and (d) pulse integral fitted with a skewed Gaussian function.

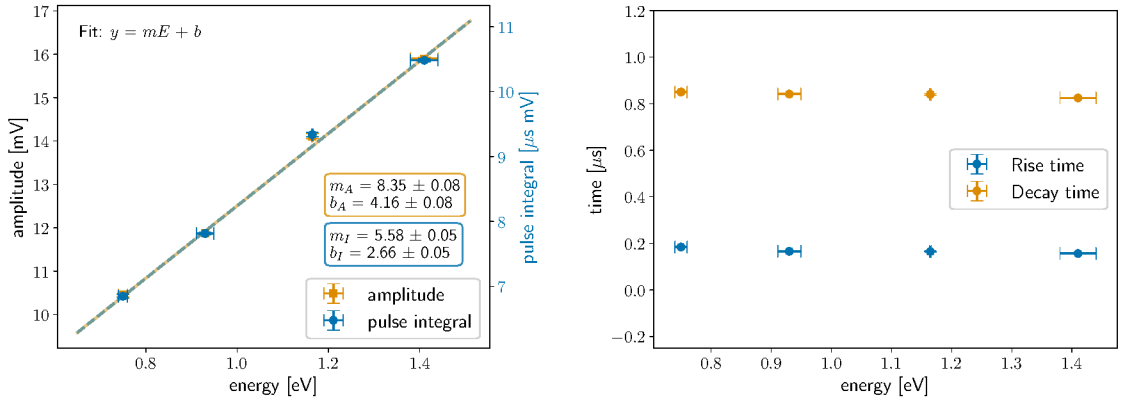

(a) (b)

Fig. D.8.: Most probable values of fitting parameters for photon pulses of different energies (wavelengths) measured with the TES F module during calibration (no-fiber calibration setup) for (a) pulse integral and amplitude, and (b) rise and decay time parameters τ_+ and τ_-. The fit uncertainties of the pulse integral are not visible at this scale and the uncertainties of the energy results from the spectral spread of the used laser diode.

E Electronic Noise: χ^2_{dof} in Frequency Domain

Continuing from Sec. 3.4.2: Taking the example from Fig. 3.10 (b), the fast noise spikes can be modeled by a finite-width Dirac delta approximation on top of the noise baseline. A data sample x_i of N samples at time t_i with a time bin size Δt is considered:

$$x_i = \begin{cases} V', & \text{if } t_0 - \frac{\Delta t}{2} \leq t_i \leq t_0 + \frac{\Delta t}{2} \\ 0, & \text{else,} \end{cases} \tag{E.1}$$

where t_0 is the position of the delta function. The discrete Fourier transform of the sample at frequency ν_i is then given by

$$f_i = \sum_{j=1}^{N} x_j e^{-i2\pi t_j \nu_i} \approx V' e^{-i2\pi t_0 \nu_i} \tag{E.2}$$

resulting in the Fourier transform of $\mathcal{F}(\nu_i) = f_i \Delta t$, when scaling with the bin-size Δt, which yields the amplitude and phase of the FFT:

$$\mathcal{F}(\nu_i) = V' \Delta t e^{-i2\pi t_0 \nu_i}. \tag{E.3}$$

This would result in a sine wave with amplitude $V'\Delta t$. The usual bin size for the measurements is at $\Delta t = 0.02\,\mu\mathrm{s}$ due to the sampling rate of 50 MHz. Therefore, even with an example voltage pulse as large as $V' = 15\,\mathrm{mV}$, this would result in an amplitude of $V'\Delta t = 0.3\,\mathrm{mV}\,\mu\mathrm{s} = 0.3\,\frac{\mathrm{mV}}{\mathrm{MHz}}$. Therefore the model spike would in frequency domain only contribute to the signal amplitude at $0.3\,\frac{\mathrm{mV}}{\mathrm{MHz}}$. When comparing this with Fig. 3.11 (a) and (b), the value is much smaller than the uncertainties within the fit range.

It can be gauged, where the signal would have an amplitude comparable to the uncertainties. For a recorded time window of $T = 80\,\mu\mathrm{s}$, the bin size in frequency domain is $\Delta\nu = 1/T = 12.5\,\mathrm{kHz}$ and the Fourier transformation of the noise depends on the time window and the PSD:

$$\mathcal{F}_n(\nu_i) = \sqrt{T \cdot \mathrm{PSD}(\nu_i)}. \tag{E.4}$$

Therefore the model spike would in frequency domain only contribute to the $\sqrt{\mathrm{PSD}}$ at $\sqrt{\mathrm{PSD}} = 0.0335\,\mathrm{mV}/\sqrt{\mathrm{MHz}}$. Comparing this value with the $\sqrt{\mathrm{PSD}}$ in Fig. 3.11 (d), the modeled spike will only contribute at very high frequencies beyond ~20 MHz.

F Dark Matter Measurement Instructions

The following outlines the measurement preparations for DM measurements mentioned in Sec. 4.1.

Setup

The setup follows the setup for DM measurements described in Sec. 2.4.3. The fibers should be left uncovered and the slit on top of the aluminum can should not be covered with tape either, to allow for some laser light to scatter into the can, which can be used for calibration.

Determination of lowest trigger level

In order to perform intrinsics measurements for direct dark matter searches sensitivity to low energies needs to be as high as possible. This directly correlates with the trigger threshold we can reach with our measurements, which should be as low as possible to be able to probe interesting parameter space. First, the TES and SQUIDs need to be set up, preferably with settings similar to ones from a recent successful run with light samples.

Start Measurement

Once the Alazar card is connected, the Alazar GUI can be opened with the DAQ PC and record a 1 s continuous timeline without a trigger for both channels. The sampling frequency should be set to 50 MHz. The used working point, GBWP settings as well as correct cool-down number should be noted and meaningful comments inserted into the metadata field. Once the timeline has been recorded, a trigger finding algorithm for intrinsic measurements can be used to find the lowest trigger threshold without overextending the sampling rate of the DAQ. Next, the lowest trigger threshold should be chosen from the output list of the algorithm, which has a trigger rate around 0 cps. With this trigger level, a 1 min test run can be performed. The maximum possible number of processors (up to 7 currently) should be used for this measurement, in case errors appear at lower processor numbers. The test run should confirm a trigger rate below 5 Hz, but preferably around 1 Hz. After a suitable trigger threshold without errors in the Alazar GUI is found, a multiple day measurement for DM searches can be started immediately using the found trigger threshold. The used SQUID channel can be set to sleep mode for this measurement in the SQUIDViewer software. The measurement should be started once the light has been turned off and just before leaving and closing the lab and a "no entry" sign should be prepared for the laboratory. The room should not be entered until the end of the measurement. If the room needs to be entered e.g. for cryostat maintenance, the measurement should be stopped immediately and consecutively a new one should be started after finishing maintenance work.

Taking Light samples

For proper calibration light samples from laser light from the top of or below the MXC stage is needed. The following procedure outlines this calibration:

The laser should be connected to one of the TES fibers outside of the cryostat and attenuated accordingly. The equipment used for attenuation and setup of each laser is listed in App. B. The 1064 nm can also be used to record photon samples between consecutive DM search measurements to monitor the stability of pulses. In the past it proved efficient to use a 1 % beam splitter and 25 dB attenuator to achieve about ~ 80 nW of energy (enough to see light and not heat up the MXC stage). With the AlazarGUI at least a 1 min long triggered (either using a trigger level at 75 % of the 1064 nm pulse height or the same trigger level as for the DM search) timeline should be recorded to record some laser light for calibration - there need to be enough pulses to have statistics for fitting. It is important to remember to turn the laser off afterwards.

G Analysis Results TES F

G.1 Analysis and Trigger Acceptance

The following summarizes and shows the analysis results for TES F regarding Ch. 4. The analysis and trigger acceptance determined for different energy bins and additional simulations is listed in Tab .G.4. As for TES D, all simulations were performed using the

Simulation	1064 nm	1640 nm	$0.1 - 3.0$ eV
α^{trig}	100 %	97.1 %	85.9 %
$\alpha^{\text{trig}} \cdot \alpha^{\text{ana}}$	99.5 %	95.9 %	85.0 %

Simulation [eV]	0.1–0.2	0.2–0.3	0.3–0.4	0.4–0.5	0.5–0.6	0.6–0.7	0.7–0.8	≥ 0.8
α^{trig}	0.8 %	3.8 %	13.3 %	33.4 %	60.4 %	84.5 %	95.5 %	≥ 99.2 %
$\alpha^{\text{trig}} \cdot \alpha^{\text{ana}}$	0.7 %	3.5 %	13.0 %	32.8 %	59.7 %	82.7 %	94.6 %	≥ 98.3 %

Tab. G.4.: Trigger and combined trigger and analysis acceptance across different simulations for TES F: Top: *calibration* simulation for the two wavelengths and *spectrum* simulation, bottom: *bin-wise* simulation. The uncertainties on the acceptances are on the order of 0.1 %.

same trigger as in the DM measurement. In contrast to TES D, not all signals of the two calibration points pass the hardware trigger, which is the case for the 1064 nm but not the 1640 nm simulation. However, most of them survive the pulse finder. Observing the overall full spectrum range from 0.1 eV to 3.0 eV more than 84 % of pulses survive both

the hardware trigger and analysis. However, this value is biased towards larger energies, since the bin-wise acceptance shows much lower acceptance values for lower energies. Below about 0.5 eV less than half of the signals do not pass the trigger, although of the ones that do a majority still survives the analysis. Compared to TES D this shows a worse sensitivity for energies above 0.3 eV, but a better one for the lowest energies of 0.1 eV to 0.2 eV most likely due to a lower trigger level, which is lower taking into account the SNR as well, since the significantly higher trigger rate points towards a majority of triggers on the noise baseline. This could also be influenced by the shifts in the noise baseline.

G.2 Event Selection

Figure G.9 shows the post pulse finder results for the fit parameters from the combined DM searches of TES F listed in Tab. 4.1, compared with the results of the photon calibration samples recorded before the first measurement. Compared to TES D the rise and decay time parameters of the DM search run are less separated for TES F, as well as the start time parameter t_0. The pulse integral parameters of the calibration samples are also less separated from the majority of DM search triggers. This points towards a reduced separation power between signals and noise, which is also reflected in the lower SNR compared to TES D. Fig. G.10 shows the distributions in logarithmic scale without normalization and including the full range.

The same three set of cuts used in the TES D analysis are investigated for the TES F analysis. Therefore, calibration data and simulations based on TES F measurements, are used to define *loose* and *tight* cuts, as well. The *tight* cuts are simply shrinking the *loose* cut range. These 2D distributions are shown together with the cut ranges in Fig. G.11 Again the 2D histograms are more localized for the simulation compared to the measured data, which shows outliers and possible backgrounds passing the hardware trigger as well. Figure G.12 shows the 2D distribution of rise and decay time parameters for the simulated spectrum from 0.1 eV to 3 eV including both cut schemes. For the start time of the pulse and the χ^2_{dof} distributions, the simulation and data samples together with the cut regions are visualized in Fig. G.13. For the deviation ratio $\mathcal{R}_{\mathrm{dev}}$, the histogram is investigated and fitted with a normal distribution depicted in Fig. G.14 (a). Compared to TES D, less outliers were recorded with the used calibration sample.

All cut parameters for the *loose* and *tight* cut selection schemes are summarized in Tab. G.5. In comparison, the *systematic* cuts not only place cuts on the fit parameters from the FFT analysis, but also from fitting the phenomenological function. The cut parameters for the systematic cut selection are listed in Tab. G.6. Note that both FFT and phenomenological cuts are applied to the dataset simultaneously.

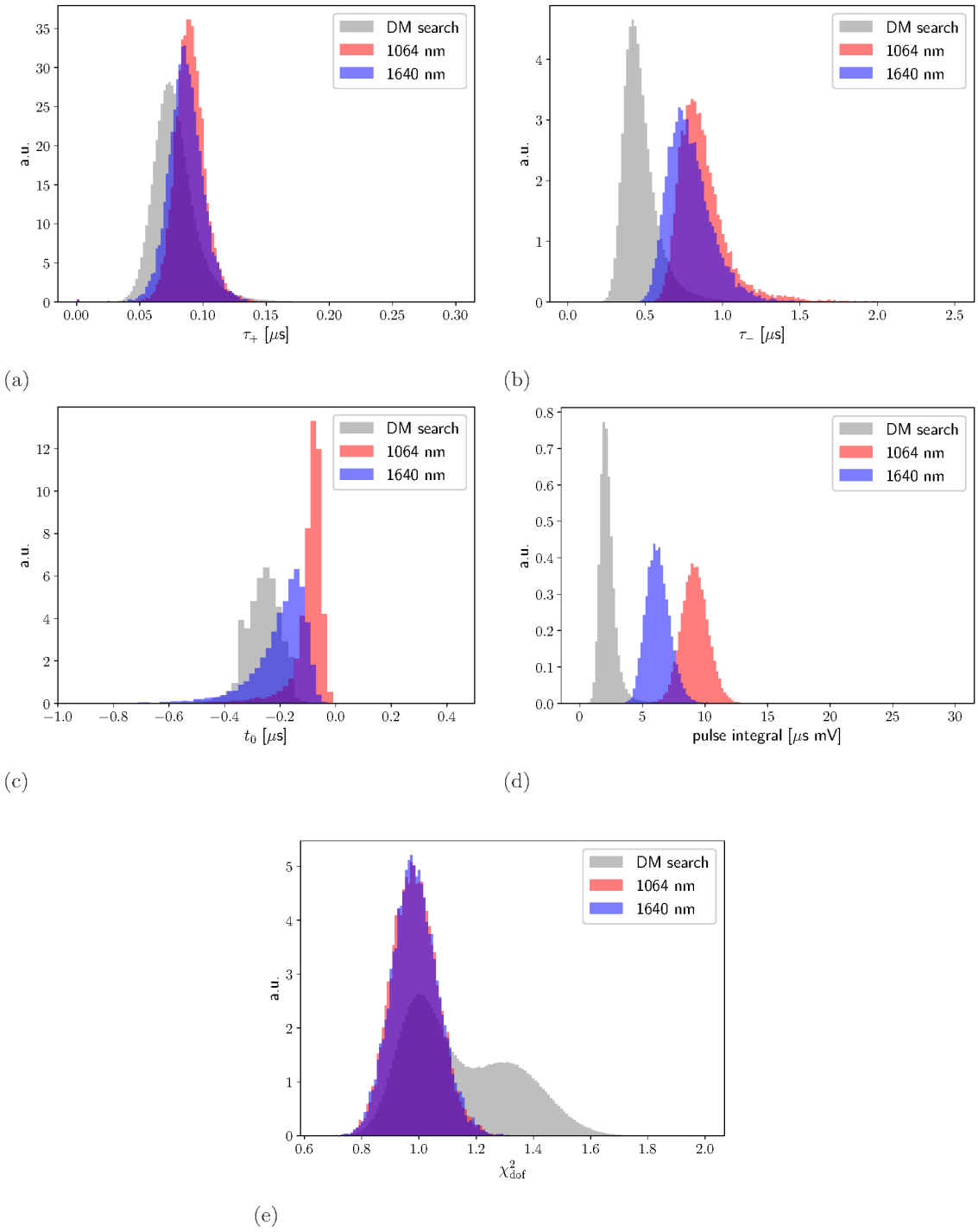

Fig. G.9.: Distribution (normalized to the same integral) of fit parameters (post pulse finder) showing both DM search and laser calibration data of TES F: (a) rise time (b) decay time (c) start time (d) pulse integral and e) χ^2_{dof}. The x-ranges are zoomed-in to allow comparison between the datasets, outliers outside of these regions exist.

The systematic cuts are based on the *spectrum* simulation and both FFT, see Fig. G.15, and phenomenological fits, see Fig. G.16. For this purpose the τ_+, τ_- and χ^2_{dof} distribution

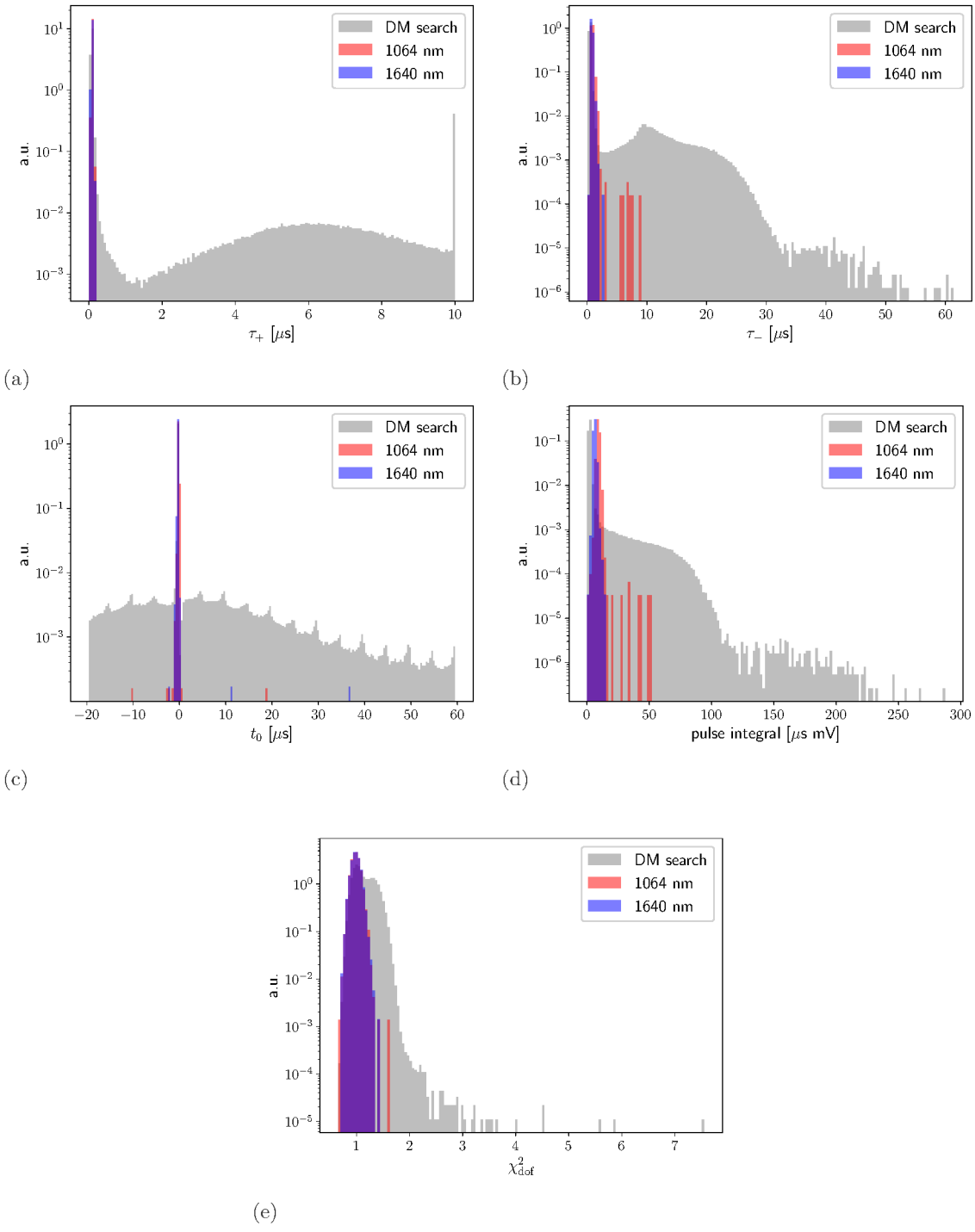

Fig. G.10.: Distribution (normalized to the same integral) of fit parameters (post pulse finder) showing both DM search and laser calibration data of TES F: (a) rise time (b) decay time (c) start time (d) pulse integral and (e) χ^2_{dof}. The x-ranges are zoomed-in to allow comparison between the datasets, outliers outside of these regions exist.

are fitted with a normal distribution around their peak to determine their 2σ distribution to be used for the cuts to constrain contributions outside of these regions. For the start

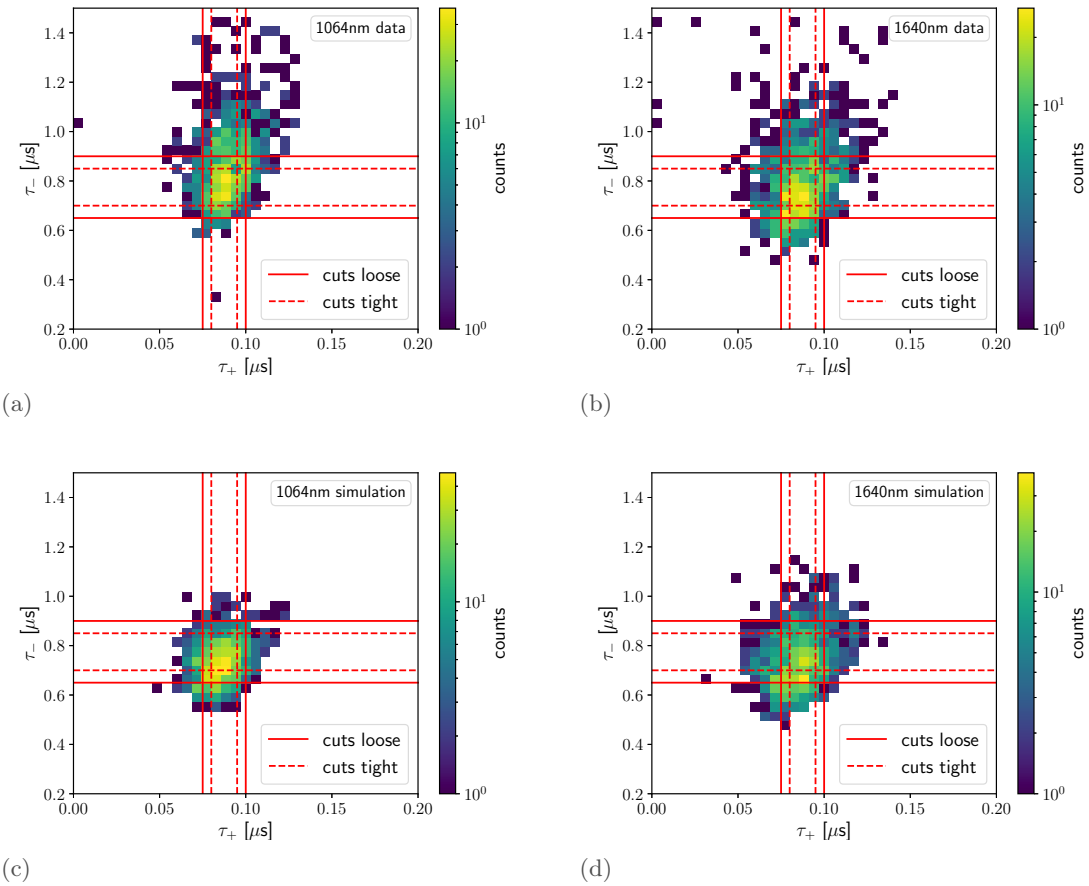

Fig. G.11.: 2D distribution of the rise and decay time of measured and *simulated calibration* samples: (a) 1064 nm data (b) 1640 nm data (c) 1064 nm simulation (d) 1640 nm simulation for TES F. The solid and dashed red lines show the placement of *loose* and *tight* cuts, respectively.

cut scheme	τ_+ [μs]	τ_- [μs]	$\chi^2_{\mathbf{dof}}$	t_0 [μs]	$\mathcal{R}_{\mathrm{dev}}$
loose cuts	(0.075, 0.1)	(0.65, 0.9)	(0.85, 1.1)	(-0.4, 0.4)	(0.65, 1.11)
tight cuts	(0.08, 0.095)	(0.7, 0.85)	(0.9, 1.05)	(-0.4, 0.4)	(0.65, 1.11)

Tab. G.5.: Summary of event selection cuts for both *loose* and *tight* schemes for TES F. The cuts are applied to the rise τ_+, decay τ_- and arrival times t_0 of each pulse, including the χ^2_{dof} and the deviation ratio between the pulse height of the fit and the minimum of the recorded pulse $\mathcal{R}_{\mathrm{dev}}$.

time parameter t_0, the lower 99.73 % quantile is determined from the whole distribution of the 1640 nm calibration sample instead, to determine the lower position of the 3σ region. This value is used symmetrically around 0 for the cuts, to account for differences between simulation and data. The start time is therefore mainly used to get rid of outliers, which are not represented in simulation data.

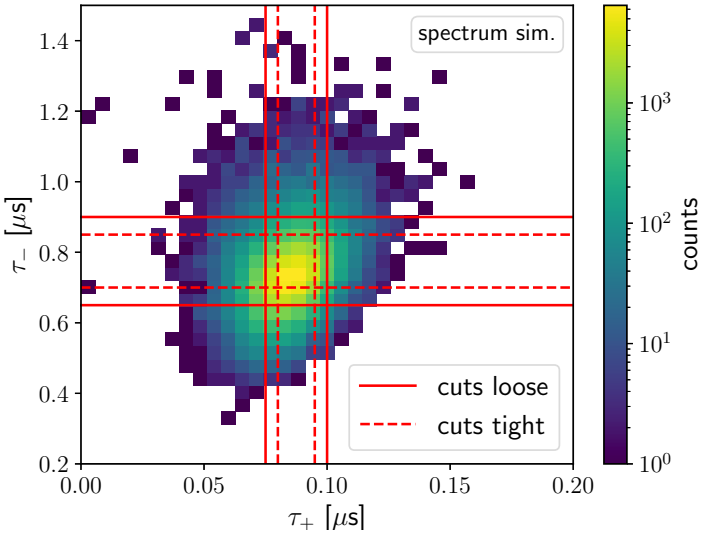

Fig. G.12.: 2D distribution of the rise and decay time of simulated *spectrum* for TES F over the whole energy range from 0.1 eV to 3 eV. The solid and dashed red lines show the placement of *loose* and *tight* cuts, respectively.

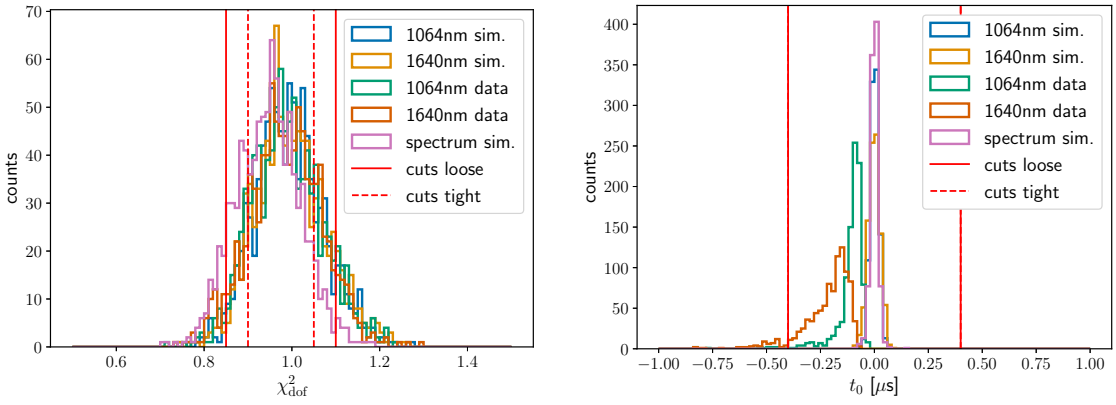

(a) (b)

Fig. G.13.: Distributions of fit parameters of measured and *simulated calibration* samples: (a) χ^2_{dof} distributions and (b) t_0 distributions for TES F. The solid and dashed red lines show the placement of *loose* and *tight* cuts, respectively, which are the same for the pulse arrival time t_0.

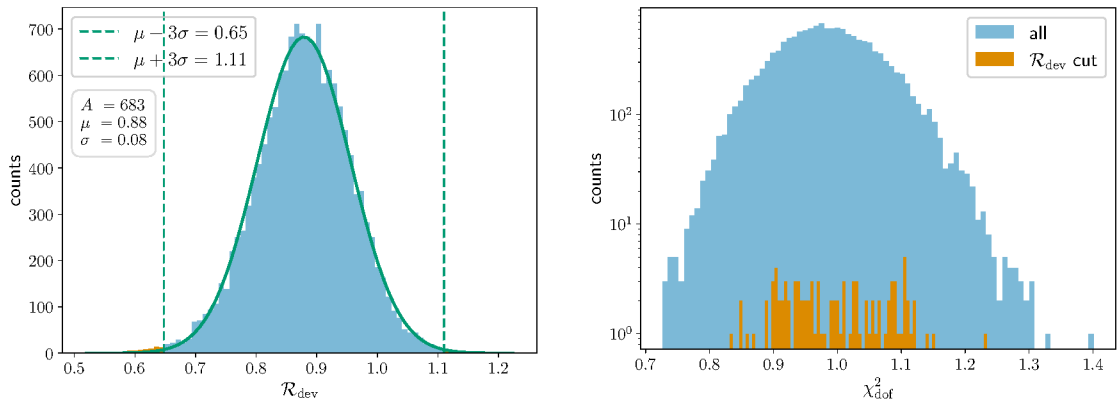

(a) (b)

Fig. G.14.: Parameter distributions based on the measured 1640 nm calibration sample (TES F) with all triggers shown in blue and filtered triggers shown in orange for (a) $\mathcal{R}_{\mathrm{dev}}$ distribution fitted with a Gaussian (green line). The green dashed lines shows the 3σ cuts around the distribution's mean. (b) χ^2_{dof} parameter distribution shown in logarithmic scale to reveal the filtered events.

systematic cuts	$\tau_{+/\mathrm{rise}}$ [μs]	$\tau_{-/\mathrm{decay}}$ [μs]	$\chi^2_{\mathbf{dof}}$	t_0 [μs]	$\mathcal{R}_{\mathrm{dev}}$
FFT cuts	(0.07, 0.10)	(0.62, 0.84)	(0.80, 1.09)	(-0.77, 0.77)	(0.65, 1.11)
Pheno. cuts	(0.02, 0.05)	(0.60, 0.98)	(0.33, 0.42)	(-0.6, 0.6)	

Tab. G.6.: Summary of systematic event selection cuts including both FFT and phenomenological fitting functions of TES F, which are combined for the *systematic* cut scheme. The cuts are applied to the rise, decay and arrival parameters t_0 of each pulse, including the χ^2_{dof} and the deviation ratio between the FFT pulse height of the fit and the minimum of the recorded pulse $\mathcal{R}_{\mathrm{dev}}$. In this case the fit parameters, except for t_0 were selected using a 2σ region around the mean of the fit parameter distributions of the simulated *spectrum*.

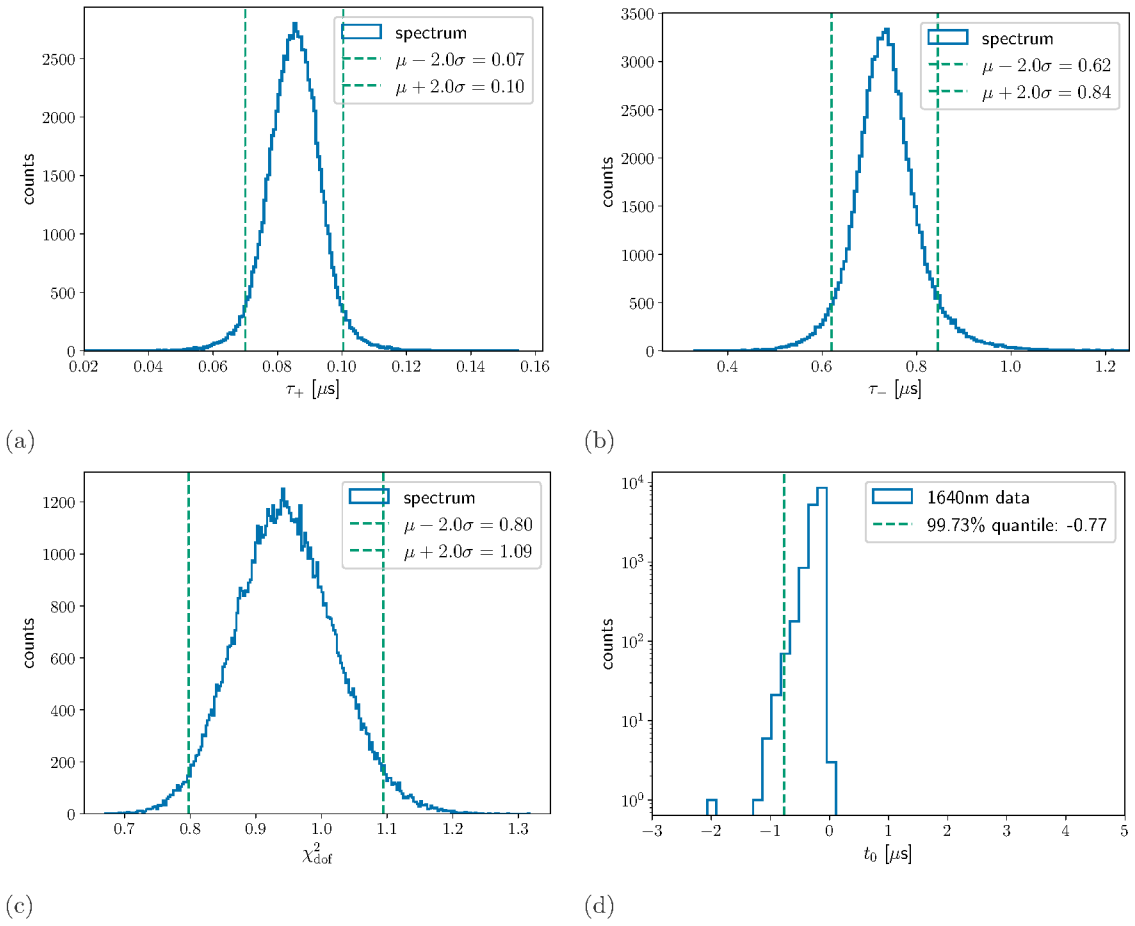

Fig. G.15.: Distributions of the FFT fit parameters of the simulated *spectrum* (TES F): (a) rise time (b) decay time (c) χ^2_{dof} and (d) start time. The dashed green lines show the placement of cuts at the 2σ region, based on a normal distribution. For the start time t_0, the position of the lower 3σ region is determined from the entire distribution. Distributions are zoomed in on the regions of interest.

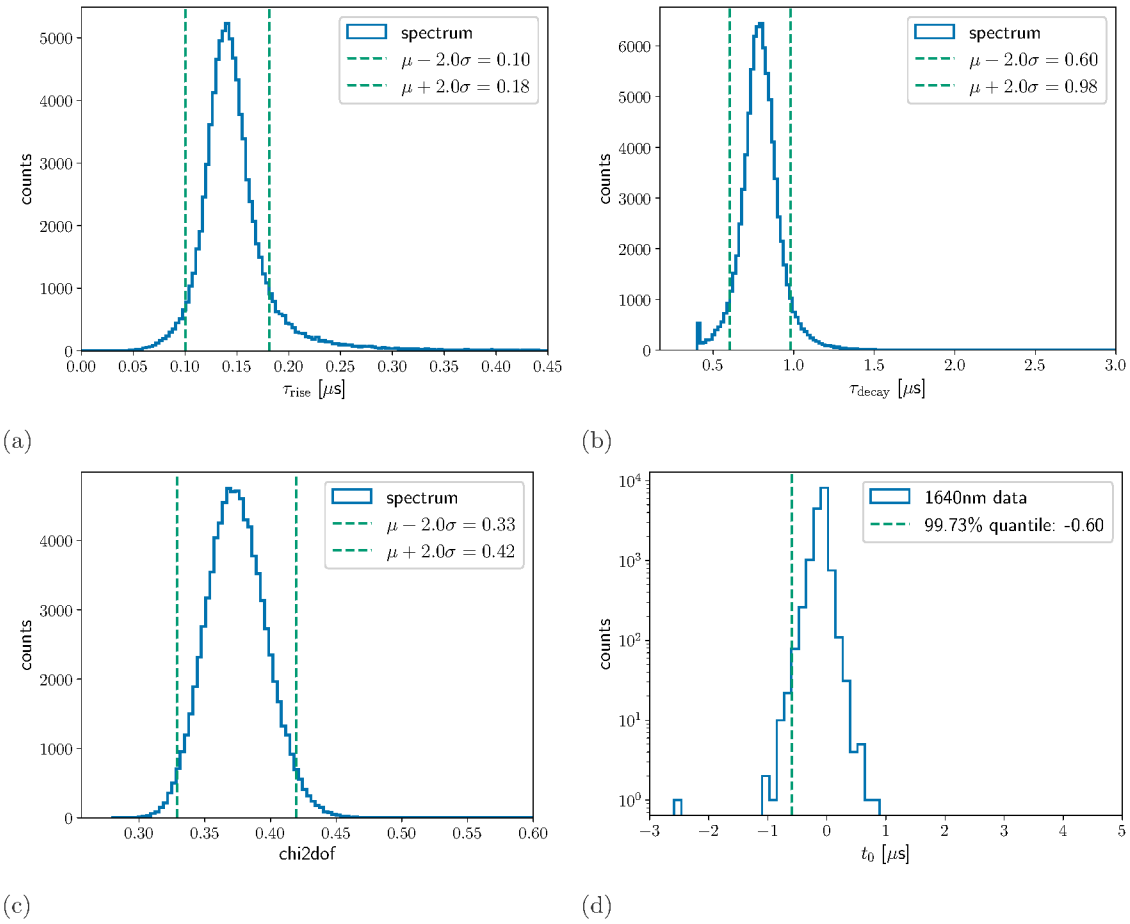

Fig. G.16.: Distributions of the phenomenological fit parameters of the simulated *spectrum* (TES F): (a) rise time (b) decay time (c) χ^2_{dof} and (d) start time. The dashed green lines show the placement of cuts at the 2σ region, based on a normal distribution. For the start time t_0, the position of the lower 3σ region is determined from the entire distribution. Distributions are zoomed in on the regions of interest.

H Analysis Results TES D

The comparison between the distribution of fit parameters of the pre-run calibration samples and the combined TES D DM runs in Fig. 4.2 is shown here in logarithmic scale and without normalization as well to visualize outliers and a true comparison of the events after the FFT fitting analysis. These are shown in Fig. H.17

The following reports on the distributions the systematic cuts placed on TES D are based on, see Sec. 4.2.2. For the systematic cuts these are based on the *spectrum* simulation and both FFT, see Fig. H.18, and phenomenological fits, see Fig. H.19. The cuts follow the same procedure as outlined in App. G.2.

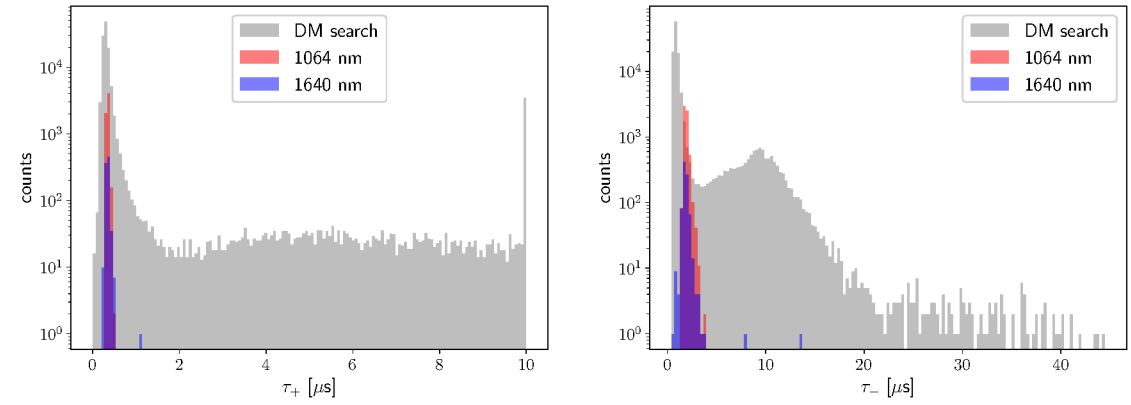

(a)

(b)

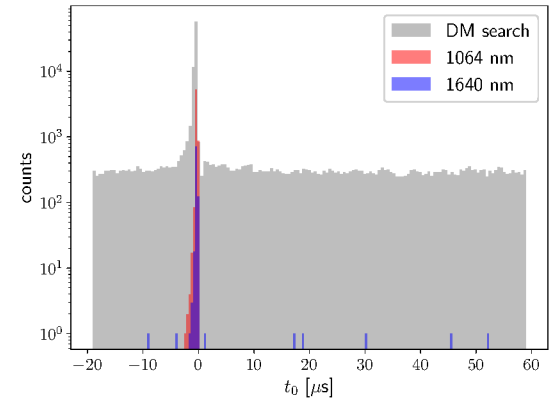

(c)

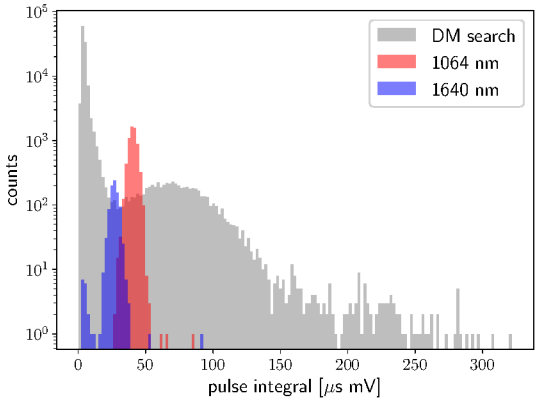

(d)

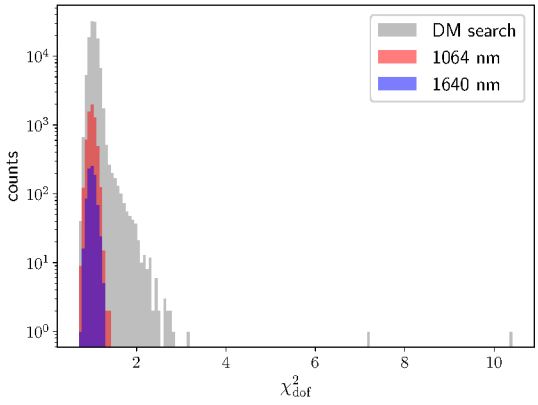

(e)

Fig. H.17.: Distribution (normalized to the same integral) of fit parameters (post pulse finder) showing both DM search measurement and laser calibration data in logarithmic scale for TES D: (a) rise time (b) decay time (c) start time (d) pulse integral and e) χ^2_{dof}.

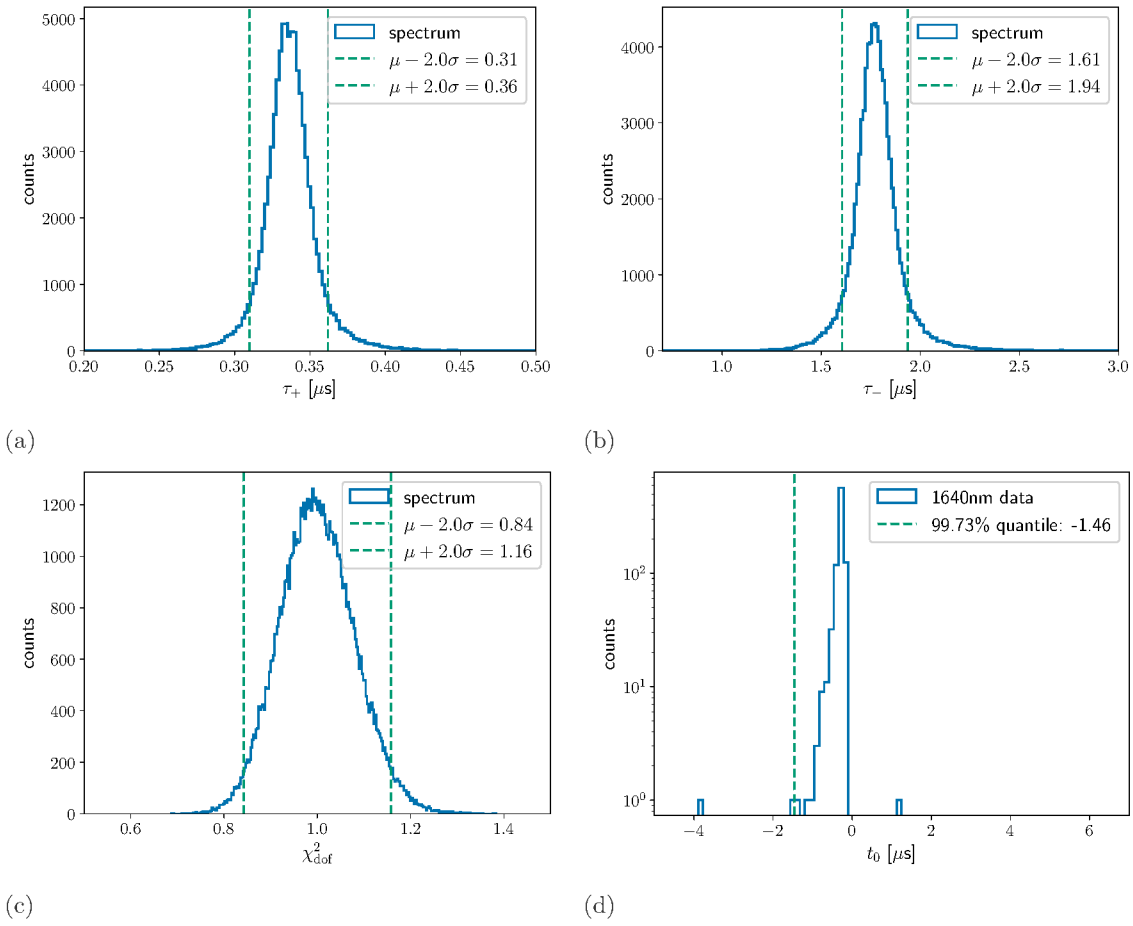

Fig. H.18.: Distributions of the FFT fit parameters of the simulated *spectrum* (TES D): (a) rise time (b) decay time (c) χ^2_{dof} and (d) start time. The dashed green lines show the placement of cuts at the 2σ region, based on a normal distribution. For the start time t_0, the position of the lower 3σ region is determined from the entire distribution. Distributions are zoomed in on the regions of interest.

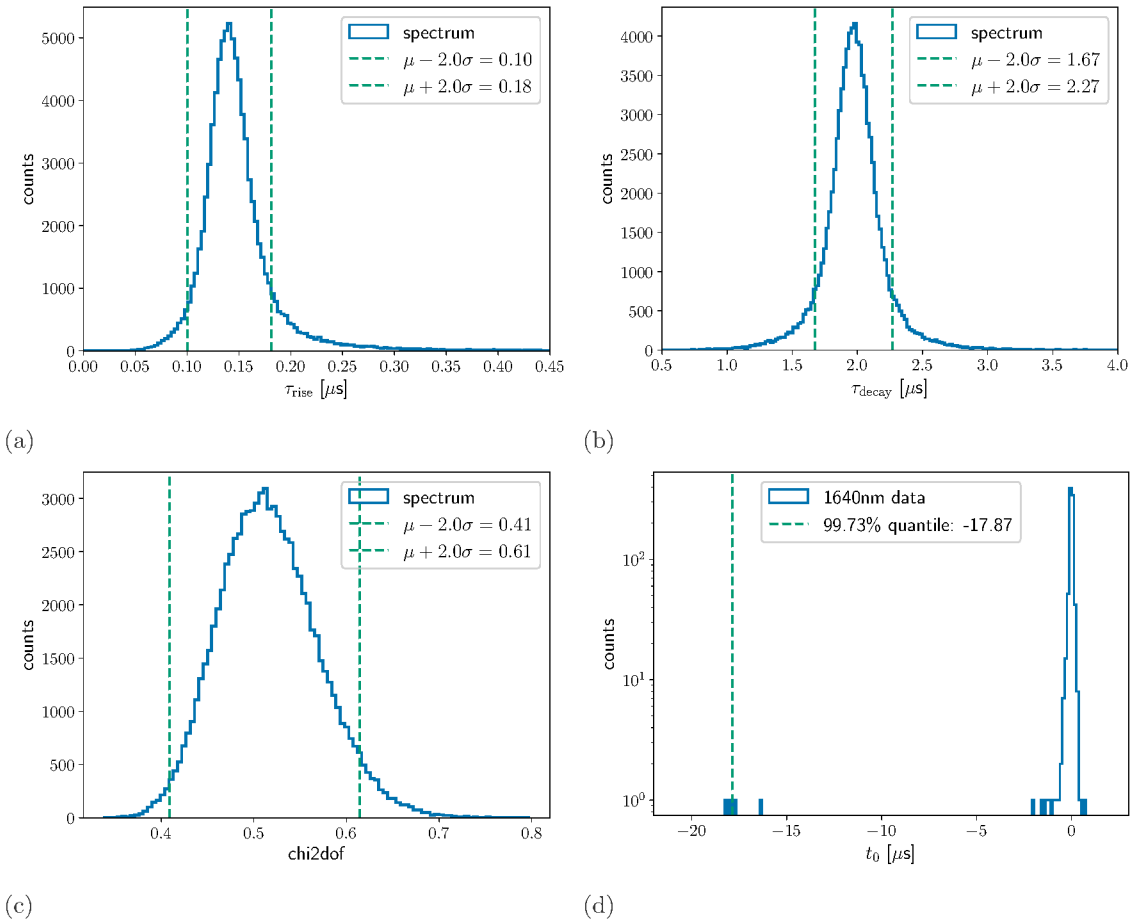

Fig. H.19.: Distributions of the phenomenological fit parameters of the simulated *spectrum* (TES D): (a) rise time (b) decay time (c) χ^2_{dof} and (d) start time. The dashed green lines show the placement of cuts at the 2σ region, based on a normal distribution. For the start time t_0, the position of the lower 3σ region is determined from the entire distribution. Distributions are zoomed in on the regions of interest.

H.1 $\mathcal{R}_{\text{dev}}$: Example Pulses

In Sec. 4.2.2 the $\mathcal{R}_{\text{dev}}$ cuts are introduced using the example of a 1640 nm calibration sample. The trigger level (6 mV) is similar to the one used for the DM search measurement (5.6 mV). Figure H.20 shows examples of pulses outside of the defined 3σ region including their respective $\mathcal{R}_{\text{dev}}$ ratio. Figure H.20 (a)-(c) show examples where the noise baseline

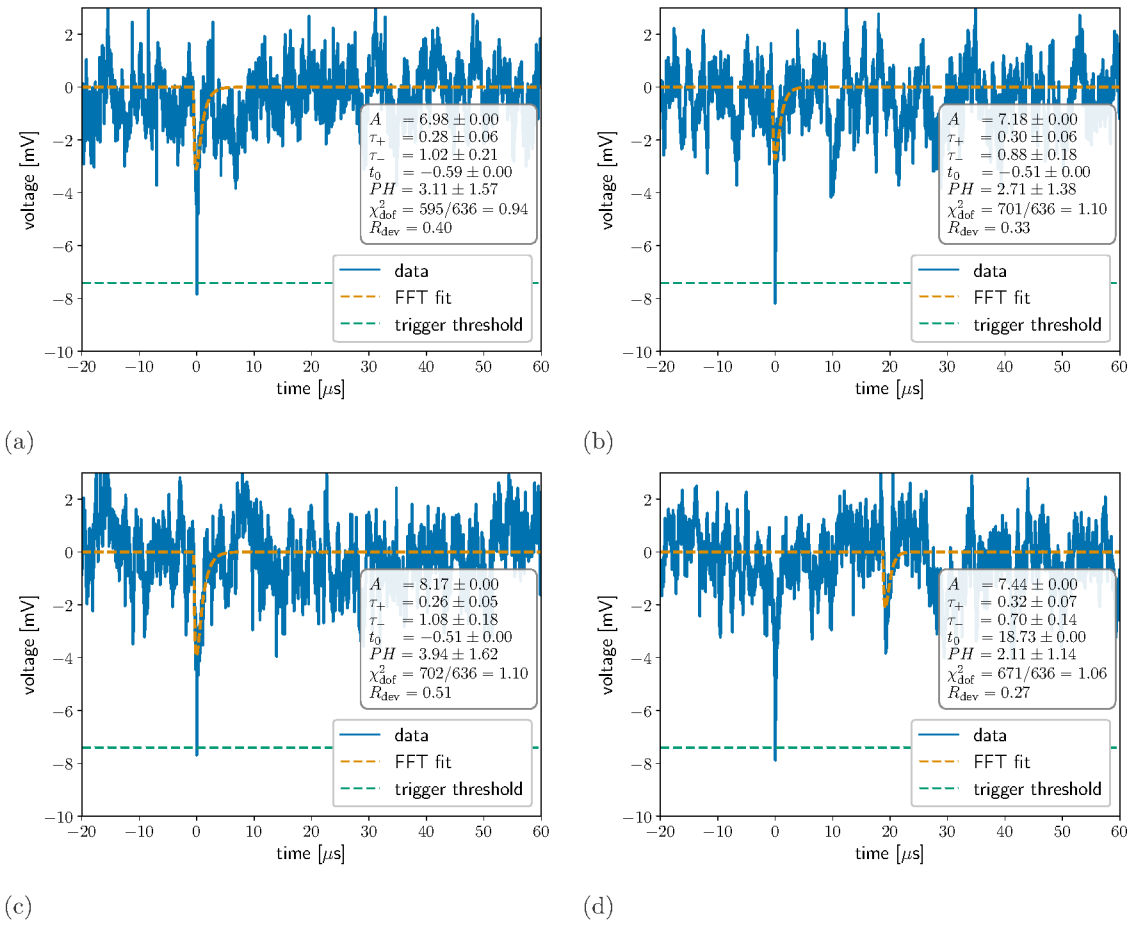

Fig. H.20.: Triggered events based on the pre-run calibration measurement at 1640 nm performed with TES D. (a)-(c) show fits of the noise baseline where a single spike crossed the trigger. The same is true for (d), where the pulse finder identified a fluctuation in the noise baseline as a pulse instead. The trigger level is adjusted regarding to the noise offset, which is corrected in these plots.

was fitted. Depending on the cuts, these pulses would be isolated by other fit parameters. However, for large datasets some could still survive other selection cuts on the fit parameters, as shown in Fig. 3.11. Figure H.20 (d) shows the case where the pulse finder misidentified a noise fluctuation as pulse. Without the previous spike, this would not have been triggered. Most pulses like this would however be discarded based on the t_0 parameter, indicating a large offset of the pulse finder from the trigger position.

I Dark Matter Search Energy Calibration

Figure I.21 shows both the full calibration from a previous cool-down (based on Fig. 3.8), together with the pre-run calibration conducted shortly before starting the DM search run in the same cool-down. Both belong to module TES D and the pre-run calibration data

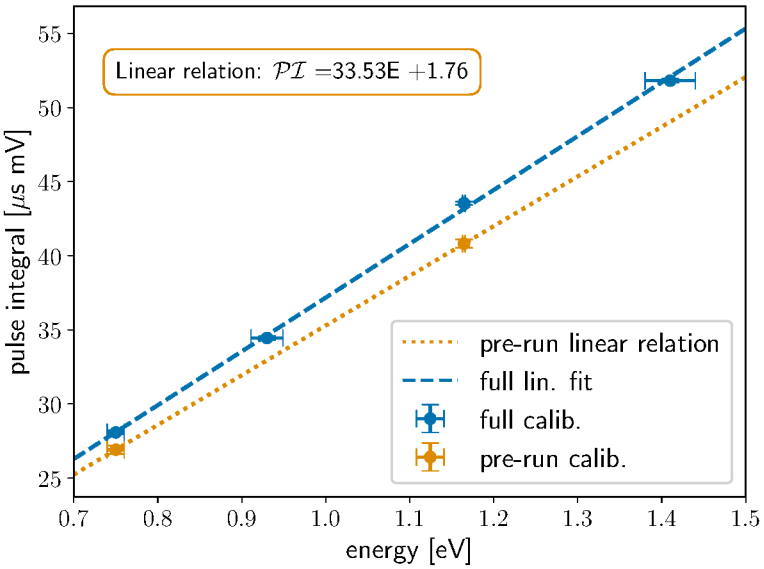

Fig. I.21.: TES D: Most probable value of the pulse integral (based on a skewed Gaussian) for different energies for the full calibration (blue, see Fig. 3.8(a)) and the pre-run calibration (orange), including the linear fit through the calibration and a line drawn through the two pre-run calibration points.

shows the linear relation reported in Eq. 4.3. The offset between the two data points from the same laser in each calibration run emphasize the importance of recording additional calibration data before a measurement. While more data points would be preferable, the complexity of the calibration measurements significantly increases the cool-down time. Therefore, only two data points are recorded and used to approximate the relation. The differences for the pulse integral for an energy of 1 eV when a line is drawn through two points each of the full calibration, instead of fitted through four points, is below the energy resolution of the TES of about ~ 0.1 eV around 1 eV.

The same holds true for TES F, where the calibration relation is shown in Fig. I.22. The pre-run calibration data shows the linear relation reported in Eq. 4.4. The differences between the pre-run and full calibration in TES F is more pronounced compared to TES D and the overall calibration relation deviates more from the fit performed on the pre-calibration data.

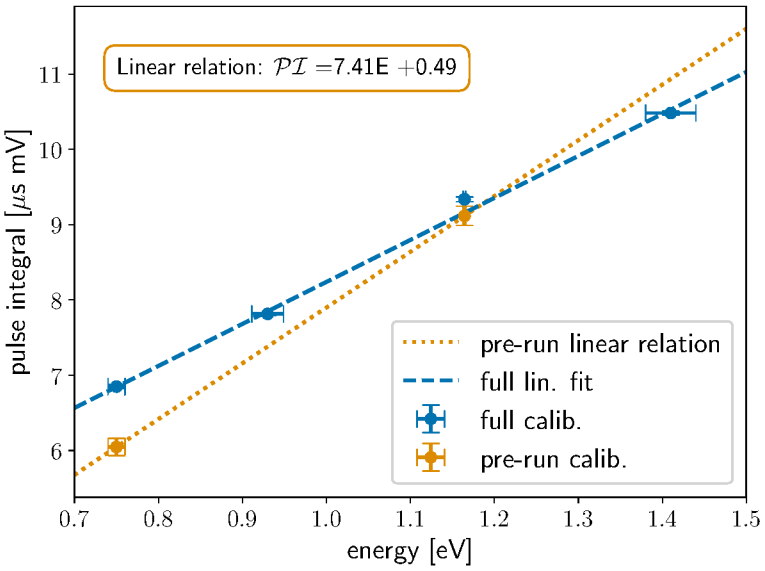

Fig. I.22.: TES F: Most probable value of the pulse integral (based on a skewed Gaussian) for different energies for the full calibration (blue, see Fig. D.8(a)) and the pre-run calibration (orange), including the linear fit through the calibration and a line drawn through the two pre-run calibration points.

Acronyms

ALP Axion Like Particle.

ALPS II Any Light Particle Search II.

C.L. Confidence Level.

CMB Cosmic Microwave Background.

DAQ Data Acquisition.

DM Dark Matter.

ETF Electro-Thermal Feedback.

FFT Fast Fourier Transformation.

FLL Flux-Locked Loop.

GBWP Gain Bandwidth Product.

KICS Kinetic Inductance Current Sensor.

LEE Low Energy Excess.

LSW Light-Shining-through-Wall.

MXC Mixing Chamber.

NIST National Institute of Standards and Technology.

PCB Printed Circuit Board.

PMT Photo-Multiplier Tubes.

PSD Power Spectral Density.

PTB Physikalisch-Technische Bundesanstalt.

Si Silicon.

SM Standard Model.

SNR Signal-to-Noise Ratio.

SNSPD Superconducting Nanowire Single Photon Detector.

SQUID Superconducting Quantum Interference Device.

SST Small Signal Theory.

TES Transition Edge Sensor.

TFN Thermal Fluctuation Noise.

TPC Time Projection Chamber.

W Tungsten.

WIMP Weakly Interacting Massive Particle.

List of Figures

List of Tables

Bibliography

[1] WM Smart. "John Couch Adams and the discovery of Neptune". In: *Nature* 158.4019 (1946), pp. 648–652 (cit. on p. 1).

[2] Albert Einstein. "Erklärung der Perihelbewegung des Merkur aus der allgemeinen Relativitätstheorie". In: *Sitzungsberichte der preußischen Akademie der Wissenschaften* 831 (1915), p. 839 (cit. on p. 1).

[3] Vera C. Rubin and W. Kent Ford Jr. "Rotation of the Andromeda Nebula from a Spectroscopic Survey of Emission Regions". In: *Astrophys. J.* 159 (1970), pp. 379–403 (cit. on p. 1).

[4] Fritz Zwicky. "Die Rotverschiebung von extragalaktischen Nebeln". In: *Helvetica Physica Acta, Vol. 6, p. 110-127* 6 (1933), pp. 110–127 (cit. on p. 1).

[5] Douglas Clowe, Marusa Bradac, Anthony H. Gonzalez, et al. "A direct empirical proof of the existence of dark matter". In: *Astrophys. J. Lett.* 648 (2006), pp. L109–L113 (cit. on p. 1).

[6] Charles Alcock, Carl W Akerlof, RA Allsman, et al. "Possible gravitational microlensing of a star in the Large Magellanic Cloud". In: *nature* 365.6447 (1993), pp. 621–623 (cit. on p. 1).

[7] Jonathan L. Feng. "Dark Matter Candidates from Particle Physics and Methods of Detection". In: *Annual Review of Astronomy and Astrophysics* 48.1 (2010), pp. 495–545 (cit. on p. 3).

[8] Nassim Bozorgnia, Joseph Bramante, James M. Cline, et al. "Dark matter candidates and searches". In: *Canadian Journal of Physics* (Sept. 2024) (cit. on p. 3).

[9] F. Wilczek. "Problem of Strong P and T Invariance in the Presence of Instantons". In: *Phys. Rev. Lett.* 40 (5 Jan. 1978), pp. 279–282 (cit. on p. 3).

[10] Steven Weinberg. "A New Light Boson?" In: *Phys. Rev. Lett.* 40 (4 Jan. 1978), pp. 223–226 (cit. on p. 3).

[11] R. D. Peccei and Helen R. Quinn. "Constraints imposed by CP conservation in the presence of pseudoparticles". In: *Phys. Rev. D* 16 (6 Sept. 1977), pp. 1791–1797 (cit. on p. 3).

[12] MADMAX Collaboration, P Brun, A Caldwell, et al. "A new experimental approach to probe QCD axion dark matter in the mass range above 40μeV". In: *Eur. Phys. J. C* 79 (2019), p. 186 (cit. on p. 3).

[13] N. Du, N. Force, R. Khatiwada, et al. "Search for Invisible Axion Dark Matter with the Axion Dark Matter Experiment". In: *Phys. Rev. Lett.* 120 (15 Apr. 2018), p. 151301 (cit. on p. 3).

[14] V. Anastassopoulos, S. Aune, K. Barth, et al. “New CAST limit on the axion–photon interaction”. In: *Nature Physics* 13.6 (May 2017), pp. 584–590 (cit. on p. 3).

[15] Theopisti Dafni and Javier Galán. “Digging into axion physics with (baby) IAXO”. In: *Universe* 8.1 (2022), p. 37 (cit. on p. 3).

[16] Francesca Chadha-Day, John Ellis, and David J. E. Marsh. “Axion dark matter: What is it and why now?” In: *Science Advances* 8.8 (2022), eabj3618 (cit. on p. 3).

[17] Rikhav Shah. “A TES detector for ALPS II : characterising a cryogenic, low-background, low energy single photon detector”. eng. PhD thesis. Mainz: Johannes Gutenberg-Universität Mainz, 2023 (cit. on pp. 3, 9, 11, 17, 23, 28, 31, 33, 39, 50, 95).

[18] Jan Dreyling-Eschweiler. “A superconducting microcalorimeter for low-flux detection of near-infrared single photons”. PhD thesis. U. Hamburg, Dept. Phys., 2014 (cit. on pp. 3, 9, 17, 28, 31, 33, 39, 50, 95).

[19] E. Aprile et al. “The XENONnT dark matter experiment”. In: *Eur. Phys. J. C* 84.8 (2024), p. 784 (cit. on p. 3).

[20] Qiuhong Wang, Abdusalam Abdukerim, Wei Chen, et al. “Results of dark matter search using the full PandaX-II exposure”. In: *Chinese Physics C* 44.12 (Dec. 2020), p. 125001 (cit. on pp. 3, 4).

[21] Jelle Aalbers, DS Akerib, CW Akerlof, et al. “First dark matter search results from the LUX-ZEPLIN (LZ) experiment”. In: *Physical review letters* 131.4 (2023), p. 041002 (cit. on pp. 3, 4).

[22] F. Ruppin, J. Billard, E. Figueroa-Feliciano, and L. Strigari. “Complementarity of dark matter detectors in light of the neutrino background”. In: *Phys. Rev. D* 90 (8 Oct. 2014), p. 083510 (cit. on p. 4).

[23] J. I. Collar. “Search for a nonrelativistic component in the spectrum of cosmic rays at Earth”. In: *Physical Review D* 98.2 (July 2018) (cit. on p. 4).

[24] M. F. Albakry et al. “Search for low-mass dark matter via bremsstrahlung radiation and the Migdal effect in SuperCDMS”. In: *Phys. Rev. D* 107.11 (2023), p. 112013 (cit. on pp. 4, 86).

[25] Q. Arnaud, D. Asner, J.-P. Bard, et al. “First results from the NEWS-G direct dark matter search experiment at the LSM”. In: *Astroparticle Physics* 97 (2018), pp. 54–62 (cit. on p. 4).

[26] Govinda Adhikari, Estella B. de Souza, Nelson Carlin, et al. “Strong constraints from COSINE-100 on the DAMA dark matter results using the same sodium iodide target”. In: *Science Advances* 7.46 (2021), eabk2699 (cit. on p. 4).

[27] M Felizardo, T A Girard, T Morlat, et al. “Recent results from the SIMPLE dark matter search”. In: *Journal of Physics: Conference Series* 375.1 (2012), p. 012011 (cit. on p. 4).

[28] E. Armengaud et al. “Search for sub-GeV dark matter via the Migdal effect with an EDELWEISS germanium detector with NbSi transition-edge sensors”. In: *Phys. Rev. D* 106.6 (2022), p. 062004 (cit. on pp. 4, 86).

[29] E. Behnke, M. Besnier, P. Bhattacharjee, et al. “Final results of the PICASSO dark matter search experiment”. In: *Astropart. Phys.* 90 (Apr. 2017), pp. 85–92 (cit. on p. 4).

[30] K. Abe, K. Hiraide, K. Ichimura, et al. “A direct dark matter search in XMASS-I”. In: *Physics Letters B* 789 (Feb. 2019), pp. 45–53 (cit. on p. 4).

[31] D.S. Akerib et al. “Results of a Search for Sub-GeV Dark Matter Using 2013 LUX Data”. In: *Phys. Rev. Lett.* 122.13 (2019), p. 131301 (cit. on pp. 4, 86).

[32] D.Yu. Akimov, H.M. Araújo, E.J. Barnes, et al. “WIMP-nucleon cross-section results from the second science run of ZEPLIN-III”. In: *Physics Letters B* 709.1-2 (2012), pp. 14–20 (cit. on p. 4).

[33] E. Aprile, K. Abe, F. Agostini, et al. “First Dark Matter Search with Nuclear Recoils from the XENONnT Experiment”. In: *Physical Review Letters* 131.4 (July 2023) (cit. on p. 4).

[34] A. Aguilar-Arevalo, D. Amidei, D. Baxter, et al. “Results on Low-Mass Weakly Interacting Massive Particles from an 11 kgd Target Exposure of DAMIC at SNOLAB”. In: *Physical Review Letters* 125.24 (Dec. 2020) (cit. on p. 4).

[35] P. Agnes, I. F. M. Albuquerque, T. Alexander, et al. “Search for Dark-Matter–Nucleon Interactions via Migdal Effect with DarkSide-50”. In: *Phys. Rev. Lett.* 130 (10 Mar. 2023), p. 101001 (cit. on p. 4).

[36] A. H. Abdelhameed et al. “First results from the CRESST-III low-mass dark matter program”. In: *Physical Review D* 100.10 (Nov. 2019) (cit. on pp. 4, 86).

[37] J Aalbers, F Agostini, M Alfonsi, et al. “DARWIN: towards the ultimate dark matter detector”. In: *Journal of Cosmology and Astroparticle Physics* 2016.11 (2016), p. 017 (cit. on p. 4).

[38] Tarek Saab, Enectail Figueroa, and SuperCDMS Collaboration. *Dark Matter Limit Plotter*. `https://supercdms.slac.stanford.edu/science-results/dark-matter-limit-plotter/`. Created by Tarek Saab (University of Florida) and Enectail Figueroa (Northwestern University). Accessed: 2025-07-20. 2025 (cit. on p. 4).

[39] D. S. Akerib, P. B. Cushman, C. E. Dahl, et al. “Snowmass2021 Cosmic Frontier Dark Matter Direct Detection to the Neutrino Fog”. In: *arXiv preprint arXiv:2203.08084* (2022) (cit. on p. 4).

[40] Jonathan L. Feng and Jason Kumar. “Dark-Matter Particles without Weak-Scale Masses or Weak Interactions”. In: *Phys. Rev. Lett.* 101 (23 Dec. 2008), p. 231301 (cit. on p. 5).

[41] Adam Falkowski, Joshua T Ruderman, and Tomer Volansky. “Asymmetric dark matter from leptogenesis”. In: *Journal of High Energy Physics* 2011.5 (2011), pp. 1–32 (cit. on p. 5).

[42] Maxim Pospelov, Adam Ritz, and Mikhail Voloshin. “Secluded WIMP dark matter”. In: *Physics Letters B* 662.1 (2008), pp. 53–61 (cit. on p. 5).

[43] Yonit Hochberg, Eric Kuflik, Tomer Volansky, and Jay G. Wacker. "Mechanism for Thermal Relic Dark Matter of Strongly Interacting Massive Particles". In: *Phys. Rev. Lett.* 113 (17 Oct. 2014), p. 171301 (cit. on pp. 5, 91).

[44] Belina von Krosigk, Klaus Eitel, Christian Enss, et al. "DELight: A Direct search Experiment for Light dark matter with superfluid helium". In: *SciPost Phys. Proc.* (2023), p. 016 (cit. on p. 5).

[45] Rouven Essig, Jeremy Mardon, and Tomer Volansky. "Direct Detection of Sub-GeV Dark Matter". In: *Phys. Rev. D* 85 (2012), p. 076007 (cit. on pp. 5, 82).

[46] Simon Knapen, Tongyan Lin, and Kathryn M. Zurek. "Light dark matter: Models and constraints". In: *Phys. Rev. D* 96 (11 Dec. 2017), p. 115021 (cit. on p. 5).

[47] Yonit Hochberg, Ilya Charaev, Sae-Woo Nam, et al. "Detecting Sub-GeV Dark Matter with Superconducting Nanowires". In: *Phys. Rev. Lett.* 123.15 (2019), p. 151802 (cit. on pp. 6, 7).

[48] Noah Kurinsky, Paul Brink, Richard Partridge, Blas Cabrera, and Matt Pyle. "SuperCDMS SNOLAB Low-Mass Detectors: Ultra-Sensitive Phonon Calorimeters for a Sub-GeV Dark Matter Search". In: *arXiv preprint arXiv:1611.04083* (2016) (cit. on p. 6).

[49] J. Rothe, G. Angloher, P. Bauer, et al. "TES-Based Light Detectors for the CRESST Direct Dark Matter Search". In: *Journal of Low Temperature Physics* 193 (Dec. 2018) (cit. on p. 6).

[50] S. Marnieros, E. Armengaud, Q. Arnaud, et al. "High Impedance TES Bolometers for EDELWEISS". In: *Journal of Low Temperature Physics* 211.5–6 (Dec. 2022), pp. 214–219 (cit. on p. 6).

[51] G. Angloher, M. R. Bharadwaj, I. Dafinei, et al. "Deep-underground dark matter search with a COSINUS detector prototype". In: *Phys. Rev. D* 110 (4 Aug. 2024), p. 043010 (cit. on p. 6).

[52] J. Billard, J. Gascon, S. Marnieros, and S. Scorza. "Transition Edge Sensors with Sub-eV Resolution And Cryogenic Targets (TESSERACT) at the underground laboratory of Modane (LSM)". In: *Nuclear Physics B* 1003 (2024). Special Issue of Nobel Symposium 182 on Dark Matter, p. 116465 (cit. on p. 6).

[53] Yonit Hochberg, Yue Zhao, and Kathryn M. Zurek. "Superconducting Detectors for Superlight Dark Matter". In: *Phys. Rev. Lett.* 116.1 (2016), p. 011301 (cit. on pp. 7, 91).

[54] G. N. Gol'tsman, O. Okunev, G. Chulkova, et al. "Picosecond superconducting single-photon optical detector". In: *Appl. Phys. Lett.* 79.6 (2001), p. 705 (cit. on p. 7).

[55] Yonit Hochberg, Benjamin V. Lehmann, Ilya Charaev, et al. "New constraints on dark matter from superconducting nanowires". In: *Phys. Rev. D* 106.11 (2022), p. 112005 (cit. on pp. 7, 20, 53, 81).

[56] Laura Baudis et al. “A New Bite Into Dark Matter with the SNSPD-Based QROCODILE Experiment”. In: *arXiv preprint arXiv:2412.16279* (Dec. 2024) (cit. on pp. 8, 77).

[57] K.D. Irwin and G.C. Hilton. “Transition-Edge Sensors”. In: *Cryogenic Particle Detection*. Ed. by Christian Enss. Berlin, Heidelberg: Springer Berlin Heidelberg, 2005, pp. 63–150 (cit. on pp. 9, 12, 13, 45).

[58] José Alejandro Rubiera Gimeno. “Optimizing a Transition Edge Sensor detector system for low flux infrared photon measurements at the ALPS II experiment”. PhD thesis. Hamburg: Hamburg U., 2024 (cit. on pp. 9, 28, 33, 37–39, 41–43, 45, 49–51, 53, 60, 62, 95, 100).

[59] R Bähre, B Döbrich, J Dreyling-Eschweiler, et al. “Any light particle search II — Technical Design Report”. In: *Journal of Instrumentation* 8.09 (Sept. 2013), T09001 (cit. on p. 9).

[60] Ayman Hallal, Giuseppe Messineo, Mauricio Diaz Ortiz, et al. “The heterodyne sensing system for the ALPS II search for sub-eV weakly interacting particles”. In: *Physics of the Dark Universe* 35 (2022), p. 100914 (cit. on p. 9).

[61] Todd Kozlowski et al. “Design and performance of the ALPS II regeneration cavity”. In: *Opt. Express* 33.5 (2025), pp. 11153–11166 (cit. on p. 9).

[62] M. Diaz Ortiz et al. “Design of the ALPS II optical system”. In: *Phys. Dark Univ.* 35 (2022), p. 100968 (cit. on p. 9).

[63] Aaron D. Spector, Jan H. Põld, Robin Bähre, Axel Lindner, and Benno Willke. “Characterization of optical systems for the ALPS II experiment”. In: *Opt. Express* 24 (2016), p. 9237 (cit. on p. 9).

[64] Noemi Bastidon. “The cryogenic photon detection system for the ALPS II experiment: characterization, optimization and background rejection”. PhD thesis. Universität Hamburg, 2016 (cit. on pp. 9, 45, 60).

[65] José Alejandro Rubiera Gimeno, Friederike Januschek, Katharina-Sophie Isleif, et al. “A TES system for ALPS II - Status and Prospects”. In: *PoS* EPS-HEP2023 (2024), p. 567 (cit. on pp. 9, 11).

[66] Rikhav Shah, Katharina-Sophie Isleif, Friederike Januschek, Axel Lindner, and Matthias Schott. “Characterising a Single-Photon Detector for ALPS II”. In: *J Low Temp Phys* 209 (2022), pp. 355–362 (cit. on pp. 9, 19, 33, 49).

[67] Rikhav Shah, Katharina-Sophie Isleif, Friederike Januschek, Axel Lindner, and Matthias Schott. “TES Detector for ALPS II”. In: *PoS* EPS-HEP2021 (2022), p. 801 (cit. on pp. 9, 10, 50).

[68] José Alejandro Rubiera Gimeno, Katharina-Sophie Isleif, Friederike Januschek, et al. “The TES detector of the ALPS II experiment”. In: *Nuclear Instruments and Methods in Physics Research Section A: Accelerators, Spectrometers, Detectors and Associated Equipment* 1046 (2023), p. 167588 (cit. on pp. 9, 33, 49).

[69] Noemie Bastidon, Dieter Horns, and Axel Lindner. "Characterization of a Transition-Edge Sensor for the ALPS II Experiment". In: *arXiv preprint arXiv:1509.02064* (Sept. 2015) (cit. on p. 9).

[70] Andreas Ringwald. "Production and detection of very light bosons in the HERA tunnel". In: *Physics Letters B* 569.1-2 (2003), pp. 51–56 (cit. on p. 9).

[71] Zachary R. Bush, Simon Barke, Harold Hollis, et al. "Coherent detection of ultraweak electromagnetic fields". In: *Phys. Rev. D* 99 (2 Jan. 2019), p. 022001 (cit. on p. 10).

[72] José Alejandro Rubiera Gimeno, Katharina-Sophie Isleif, Friederike Januschek, et al. "Simulation and measurement of Black Body Radiation background in a Transition Edge Sensor". In: *arXiv preprint arXiv:2505.08555* (2025) (cit. on pp. 11, 45, 49, 50).

[73] D. H. Andrews, Jr. Brucksch W. F., W. T. Ziegler, and E. R. Blanchard. "Attenuated Superconductors I. For Measuring Infra-Red Radiation". In: *Review of Scientific Instruments* 13.7 (July 1942), pp. 281–292 (cit. on p. 12).

[74] Kevin T. Crowley, Jason E. Austermann, Steve K. Choi, et al. "Advanced ACTPol TES Device Parameters and Noise Performance in Fielded Arrays". In: *Journal of Low Temperature Physics* 193.3–4 (July 2018), pp. 328–336 (cit. on p. 12).

[75] Kazuki Niwa, Kaori Hattori, and Daiji Fukuda. "Few-Photon Spectral Confocal Microscopy for Cell Imaging Using Superconducting Transition Edge Sensor". In: *Frontiers in Bioengineering and Biotechnology* Volume 9 - 2021 (2021) (cit. on p. 12).

[76] Mark Anton Lindeman. "Microcalorimetry and the Transition-Edge Sensor". PhD thesis. University of California, Davis, 2000 (cit. on p. 15).

[77] K. D. Irwin. "An application of electrothermal feedback for high resolution cryogenic particle detection". In: *Applied Physics Letters* 66.15 (Apr. 1995), pp. 1998–2000 (cit. on p. 16).

[78] John Clarke and Alex I. Braginski. *The SQUID Handbook*. John Wiley & Sons, Ltd, 2004 (cit. on pp. 17, 18, 28).

[79] J. Pleikies, O. Usenko, K. H. Kuit, et al. "SQUID Developments for the Gravitational Wave Antenna MiniGRAIL". In: *IEEE Transactions on Applied Superconductivity* 17.2 (2007), pp. 764–767 (cit. on p. 17).

[80] John Clarke, Michael Hatridge, and Michael Mößle. "SQUID-detected magnetic resonance imaging in microtesla fields". In: *Annu. Rev. Biomed. Eng.* 9.1 (2007), pp. 389–413 (cit. on p. 17).

[81] Brian David Josephson. "Possible new effects in superconductive tunnelling". In: *Physics letters* 1.7 (1962), pp. 251–253 (cit. on p. 17).

[82] K.D. Irwin and M.E. Huber. "SQUID operational amplifier". In: *IEEE Transactions on Applied Superconductivity* 11.1 (2001), pp. 1265–1270 (cit. on p. 18).

[83] M.E. Huber, P.A. Neil, R.G. Benson, et al. "DC SQUID series array amplifiers with 120 MHz bandwidth (corrected)". In: *IEEE Transactions on Applied Superconductivity* 11.2 (2001), pp. 4048–4053 (cit. on p. 18).

[84] Robert Lasenby and Anirudh Prabhu. "Dark matter–electron scattering in materials: Sum rules and heterostructures". In: *Phys. Rev. D* 105 (9 May 2022), p. 095009 (cit. on pp. 20, 81).

[85] Yonit Hochberg, Yonatan Kahn, Noah Kurinsky, et al. "Determining Dark-Matter–Electron Scattering Rates from the Dielectric Function". In: *Phys. Rev. Lett.* 127.15 (2021), p. 151802 (cit. on p. 20).

[86] Martin Dressel and George Grüner. *Electrodynamics of solids: optical properties of electrons in matter*. Cambridge university press, 2002 (cit. on p. 20).

[87] Tanner Trickle, Zhengkang Zhang, Kathryn M. Zurek, Katherine Inzani, and Sinéad M. Griffin. "Multi-Channel Direct Detection of Light Dark Matter: Theoretical Framework". In: *JHEP* 03 (2020), p. 036 (cit. on pp. 21, 82).

[88] Aaron J. Miller, Adriana E. Lita, Brice Calkins, et al. "Compact cryogenic self-aligning fiber-to-detector coupling with losses below one percent". In: *Opt. Express* 19.10 (May 2011), pp. 9102–9110 (cit. on pp. 25, 27).

[89] A. E. Lita, B. Calkins, L. A. Pellouchoud, A. J. Miller, and S. Nam. "Superconducting transition-edge sensors optimized for high-efficiency photon-number resolving detectors". In: *Advanced Photon Counting Techniques IV*. Ed. by Mark A. Itzler and Joe C. Campbell. Vol. 7681. International Society for Optics and Photonics. SPIE, 2010, p. 76810D (cit. on p. 26).

[90] A.E. Lita, D. Rosenberg, S. Nam, et al. "Tuning of tungsten thin film superconducting transition temperature for fabrication of photon number resolving detectors". In: *IEEE Transactions on Applied Superconductivity* 15.2 (2005), pp. 3528–3531 (cit. on p. 26).

[91] N. Bastidon and D. Horns. "Radioactivity induced dark count rate for single near-infrared photon detection with a tungsten transition edge sensor at 80 mK". In: *arXiv preprint arXiv:2206.14654* (2022) (cit. on p. 33).

[92] P. Adari, A. Aguilar-Arevalo, D. Amidei, et al. "EXCESS workshop: Descriptions of rising low-energy spectra". In: *SciPost Phys. Proc.* 9 (2022), p. 001 (cit. on p. 49).

[93] G. Angloher, S. Banik, G. Benato, et al. "Latest observations on the low energy excess in CRESST-III". In: *SciPost Phys. Proc.* 12 (2023), p. 013 (cit. on p. 49).

[94] A. Aguilar-Arevalo, D. Amidei, I. Arnquist, et al. "Characterization of the background spectrum in DAMIC at SNOLAB". In: *Phys. Rev. D* 105 (6 Mar. 2022), p. 062003 (cit. on p. 49).

[95] R. K. Romani, Y.-Y. Chang, R. Mahapatra, et al. "A transition edge sensor operated in coincidence with a high sensitivity athermal phonon sensor for photon coupled rare event searches". In: *Applied Physics Letters* 125.23 (Dec. 2024), p. 232601 (cit. on p. 49).

[96] R Anthony-Petersen, A Biekert, R Bunker, et al. "A Stress Induced Source of Phonon Bursts and Quasiparticle Poisoning". In: *Nature Communications* 15.1 (2024) (cit. on p. 49).

[97] Roger K. Romani. "Aluminum relaxation as the source of excess low energy events in low threshold calorimeters". In: *Journal of Applied Physics* 136.12 (Sept. 2024), p. 124502 (cit. on p. 49).

[98] Aaron Chou, Kent Irwin, Reina H Maruyama, et al. "Quantum Sensors for High Energy Physics". In: *arXiv preprint arXiv:2311.01930* (2023) (cit. on p. 49).

[99] Isabella Oceano. "Axion and ALP search with the Any Light Particle Search II experiment at DESY". In: *Proceedings of The European Physical Society Conference on High Energy Physics — PoS(EPS-HEP2023)*. Vol. 449. 2024, p. 117 (cit. on p. 49).

[100] Manuel Meyer, Katharina Isleif, Friederike Januschek, et al. "A First Application of Machine and Deep Learning for Background Rejection in the ALPS II TES Detector". In: *Annalen der Physik* (2023), p. 2200545 (cit. on p. 50).

[101] Laura Manenti, Carlo Pepe, Isaac Sarnoff, et al. "Dark counts in optical superconducting transition-edge sensors for rare-event searches". In: *Phys. Rev. Appl.* 22 (2 Aug. 2024), p. 024051 (cit. on pp. 52, 72).

[102] Christina Schwemmbauer, Yonit Hochberg, Katharina-Sophie Isleif, et al. "Simulations for direct dark matter searches using ALPS II's TES detection system". In: *PoS* COSMICWISPers (2024), p. 055 (cit. on p. 53).

[103] Christina Schwemmbauer, Guy Daniel Hadas, Yonit Hochberg, et al. "First direct search for light dark matter interactions in a transition-edge sensor". In: *arXiv preprint arXiv:2506.18982* (2025) (cit. on p. 75).

[104] Benjamin V. Lehmann. *Personal communication*. 2025 (cit. on pp. 75, 81).

[105] Yonit Hochberg. *Personal communication*. 2025 (cit. on pp. 75, 81).

[106] J. D. Lewin and P. F. Smith. "Review of mathematics, numerical factors, and corrections for dark matter experiments based on elastic nuclear recoil". In: *Astropart. Phys.* 6 (1996), pp. 87–112 (cit. on p. 75).

[107] Liron Barak et al. "SENSEI: Direct-Detection Results on sub-GeV Dark Matter from a New Skipper-CCD". In: *Phys. Rev. Lett.* 125.17 (2020), p. 171802 (cit. on p. 76).

[108] D.W. Amaral et al. "Constraints on low-mass, relic dark matter candidates from a surface-operated SuperCDMS single-charge sensitive detector". In: *Phys. Rev. D* 102.9 (2020), p. 091101 (cit. on p. 76).

[109] A. Aguilar-Arevalo et al. "Constraints on Light Dark Matter Particles Interacting with Electrons from DAMIC at SNOLAB". In: *Phys. Rev. Lett.* 123.18 (2019), p. 181802 (cit. on p. 76).

[110] P. Agnes et al. "Constraints on Sub-GeV Dark-Matter–Electron Scattering from the DarkSide-50 Experiment". In: *Phys. Rev. Lett.* 121.11 (2018), p. 111303 (cit. on p. 76).

[111] E. Aprile et al. "Light Dark Matter Search with Ionization Signals in XENON1T". In: *Phys. Rev. Lett.* 123.25 (2019), p. 251801 (cit. on p. 76).

[112] Rouven Essig, Tomer Volansky, and Tien-Tien Yu. "New Constraints and Prospects for sub-GeV Dark Matter Scattering off Electrons in Xenon". In: *Phys. Rev. D* 96.4 (2017), p. 043017 (cit. on p. 76).

[113] Paul Szypryt et al. "Kinetic inductance current sensor for visible to near-infrared wavelength transition-edge sensor readout". In: *Commun. Eng.* 3.1 (2024), p. 160 (cit. on p. 78).

[114] Kaori Hattori, Toshio Konno, Yoshitaka Miura, Sachiko Takasu, and Daiji Fukuda. "An optical transition-edge sensor with high energy resolution". In: *Supercond. Sci. Technol.* 35.9 (2022), p. 095002 (cit. on p. 78).

[115] Paul Szypryt et al. "Toward multiplexed kinetic inductance current sensor arrays". In: *21st International Conference on Low Temperature Detectors-LTD2025, Santa Fe, NM, USA* (June 1-6 2025) (cit. on p. 78).

[116] Timon Emken, Chris Kouvaris, and Ian M. Shoemaker. "Terrestrial Effects on Dark Matter-Electron Scattering Experiments". In: *Phys. Rev. D* 96.1 (2017), p. 015018 (cit. on p. 79).

[117] Timon Emken, Rouven Essig, Chris Kouvaris, and Mukul Sholapurkar. "Direct Detection of Strongly Interacting Sub-GeV Dark Matter via Electron Recoils". In: *JCAP* 09 (2019), p. 070 (cit. on p. 79).

[118] Sinéad M. Griffin, Guy Daniel Hadas, Yonit Hochberg, Katherine Inzani, and Benjamin V. Lehmann. "Dark Matter-Electron Detectors for Dark Matter-Nucleon Interactions". In: *arXiv preprint arXiv:2412.16283* (2024) (cit. on pp. 81, 82).

[119] Guy Daniel Hadas. *Personal communication.* 2025 (cit. on p. 81).

[120] Richard H. Helm. "Inelastic and Elastic Scattering of 187-Mev Electrons from Selected Even-Even Nuclei". In: *Phys. Rev.* 104 (1956), pp. 1466–1475 (cit. on p. 83).

[121] Haipeng An, Maxim Pospelov, Josef Pradler, and Adam Ritz. "Direct Detection Constraints on Dark Photon Dark Matter". In: *Phys. Lett.* B747 (2015), pp. 331–338 (cit. on p. 83).

[122] A. Andrianavalomahefa et al. "Limits from the Funk Experiment on the Mixing Strength of Hidden-Photon Dark Matter in the Visible and Near-Ultraviolet Wavelength Range". In: *Phys. Rev. D* 102.4 (2020), p. 042001 (cit. on p. 83).

[123] R. Agnese et al. "First Dark Matter Constraints from a SuperCDMS Single-Charge Sensitive Detector". In: *Phys. Rev. Lett.* 121.5 (2018). [Erratum: Phys.Rev.Lett. 122, 069901 (2019)], p. 051301 (cit. on p. 83).

[124] Q. Arnaud et al. "First germanium-based constraints on sub-MeV Dark Matter with the EDELWEISS experiment". In: *Phys. Rev. Lett.* 125.14 (2020), p. 141301 (cit. on p. 83).

[125] Haipeng An, Maxim Pospelov, Josef Pradler, and Adam Ritz. "New limits on dark photons from solar emission and keV scale dark matter". In: *Phys. Rev. D* 102 (2020), p. 115022 (cit. on p. 83).

[126] Masahiro Ibe, Wakutaka Nakano, Yutaro Shoji, and Kazumine Suzuki. "Migdal Effect in Dark Matter Direct Detection Experiments". In: *JHEP* 03 (2018), p. 194 (cit. on p. 85).

[127] A Migdal. In: *Sov. Phys. JETP* 9 (1939), p. 1163 (cit. on p. 85).

[128] G Baur, F Rosel, and D Trautmann. "Ionisation induced by neutrons". In: *Journal of Physics B: Atomic and Molecular Physics* 16.14 (July 1983), p. L419 (cit. on p. 85).

[129] H.M. Araújo, S.N. Balashov, J.E. Borg, et al. "The MIGDAL experiment: Measuring a rare atomic process to aid the search for dark matter". In: *Astroparticle Physics* 151 (2023), p. 102853 (cit. on p. 85).

[130] E. Armengaud et al. "Searching for low-mass dark matter particles with a massive Ge bolometer operated above-ground". In: *Phys. Rev. D* 99.8 (2019), p. 082003 (cit. on p. 86).

[131] P. Agnes, I. F. M. Albuquerque, T. Alexander, et al. "Search for low-mass dark matter WIMPs with 12 ton-day exposure of DarkSide-50". In: *Phys. Rev. D* 107 (6 Mar. 2023), p. 063001 (cit. on p. 86).

[132] D. Franco. "Light dark matter search with DarkSide-50". In: *arXiv preprint arXiv:2306.12151* (2023) (cit. on p. 86).

[133] I. Alkhatib et al. "Light Dark Matter Search with a High-Resolution Athermal Phonon Detector Operated Above Ground". In: *Phys. Rev. Lett.* 127 (2021), p. 061801 (cit. on p. 86).

[134] Prakruth Adari, Itay M. Bloch, Ana M. Botti, et al. "First Direct-Detection Results on Sub-GeV Dark Matter Using the SENSEI Detector at SNOLAB". In: *Phys. Rev. Lett.* 134 (1 Jan. 2025), p. 011804 (cit. on p. 86).

[135] Di Huang, Abdusalam Abdukerim, Zihao Bo, et al. "Search for Dark-Matter–Nucleon Interactions with a Dark Mediator in PandaX-4T". In: *Phys. Rev. Lett.* 131 (19 Nov. 2023), p. 191002 (cit. on p. 86).

[136] Lawrence J. Hall, Karsten Jedamzik, John March-Russell, and Stephen M. West. "Freeze-In Production of FIMP Dark Matter". In: *JHEP* 03 (2010), p. 080 (cit. on p. 91).

[137] Fatemeh Elahi, Christopher Kolda, and James Unwin. "UltraViolet Freeze-in". In: *JHEP* 03 (2015), p. 048 (cit. on p. 91).

[138] Kathryn M. Zurek. "Asymmetric Dark Matter: Theories, Signatures, and Constraints". In: *Phys. Rept.* 537 (2014), pp. 91–121 (cit. on p. 91).

[139] Eric Kuflik, Maxim Perelstein, Nicolas Rey-Le Lorier, and Yu-Dai Tsai. "Elastically Decoupling Dark Matter". In: *Phys. Rev. Lett.* 116.22 (2016), p. 221302 (cit. on p. 91).

[140] Eric Kuflik, Maxim Perelstein, Nicolas Rey-Le Lorier, and Yu-Dai Tsai. "Phenomenology of ELDER Dark Matter". In: *JHEP* 08 (2017), p. 078 (cit. on p. 91).

[141] Muping Chen, Volodymyr Takhistov, Kazunori Nakayama, and Kaori Hattori. "Light Dark Matter Detection with Sub-eV Transition-Edge Sensors". In: *arXiv preprint arXiv:2506.10070* (June 2025) (cit. on p. 92).

[142] C. L. Chang, Y. -Y. Chang, L. Chaplinsky, et al. "First Limits on Light Dark Matter Interactions in a Low Threshold Two Channel Athermal Phonon Detector from the TESSERACT Collaboration". In: *arXiv preprint arXiv:2503.03683* (2025) (cit. on p. 92).

Colophon

This thesis was typeset with LaTeX 2_ε. It is based on the *Clean Thesis* style developed by Ricardo Langner, distributed under the LaTeX Project Public License.

In this thesis I have used (generative) AI tools to assist with the optimization of Python code used for analysis and plotting as well as spelling and grammar checks.

Acknowledgement

This thesis would not have been possible without the support of many. First and foremost, I want to thank Erika Garutti, Axel Lindner and Friederike Januschek for their supervision and the opportunity to work on this exciting and broad topic. In this context, I would like to thank Friederike especially, who guided and supported me in countless one-on-one meetings and dedicated so much of her time for my supervision. I am beyond grateful.

I would also like to thank the other members of the TES team, who accompanied me on this journey: Elmeri Rivasto, Rikhav Shah, Manuel Meyer and Katharina-Sofie Isleif for their support whenever I needed it and for creating an environment in which we could accomplish great things as a team. A special thanks in that regard goes out to Jose Alejandro Rubiera Gimeno and Gulden (Joule) Othman, for great times in the lab, lots of help and patience, and especially to Jose for having my back (and many discussions!) while finishing this thesis.

Of course I would like to thank the whole ALPS group for welcoming me (again) and also trusting me with much of the outreach work I enjoyed so much over the last years. A special thanks also goes to David Reuther and Sandy Croatto for their creative solutions to our hardware and lab problems and their moral support.

I am grateful for the insightful discussions and support regarding especially the dark matter exclusion limits and calculations with Benjamin Lehmann and Yonit Hochberg. Furthermore, I would like to thank the team around Adriana Lita and Sae Woo Nam at NIST for the supply of new TES chips. Of course I also want to thank PTB, Jörn Beyer and Marco Schmidt for assembling the TES modules, providing the SQUIDs and many helpful discussions and tutorials regarding the hardware. I also want to thank Dieter Horns for the TES module we could borrow, while ours were broken. Furthermore, I am grateful for the opportunities presented to me through my membership of the PIER graduate school, especially regarding the travel award, enabling me to share and discuss my research abroad.

I would like to thank the many groups at DESY, which made my time truly worthwhile in many different ways: the members of the FH Early Career Scientist Board, the amazing women I met in dynaMENT and especially Eileen Schwanold for the organization of this amazing program, Freya Blekman for being my dynaMENT mentor, the whole PR team—especially Lisa Caspar—and Zarah Saleh from ITT for the organization of the Cross-Innovation Hub.

Last but not least, I want to express my gratitude to my partner Konstantin, my family, and my friends for their patience, encouragement and emotional support.